ON THE ABILITY OF PROTECTIVE HEADGEAR TO ALTER SKULL AND BRAIN KINETICS DURING BLAST AND IMPACT: AN EXPERIMENTAL STUDY USING A SURROGATE MODEL OF THE HUMAN HEAD WITH NOVEL INSTRUMENTATION

by

Austin David Azar

A thesis submitted in partial fulfillment of the requirements for the degree of

Master of Science

DEPARTMENT OF MECHANICAL ENGINEERING

University of Alberta

Abstract

Blast-induced traumatic brain injury (bTBI) has become increasingly prevalent among military personnel over recent years. Head protection is fielded to mitigate the amount of energy imparted to head, as a result of ballistic and impact exposure. Despite the efficacy of contemporary headgear in protecting the wearer from ballistic and impact threats, rates of bTBI have been continuing to rise. Limited biomechanical literature exists to determine whether or not modern military head protection is able to alter the transmission of blast energy into the head and brain. Using a simulant-based surrogate model of the human head, equipped with a novel array of instrumentation, this thesis aims to investigate the effect of protective headgear on the transmission of energy into the head and brain during blast and impact experiments.

The development and validation of an in-fibre Bragg grating (FBG) transducer for measuring kinetics on the inner skull table are first presented. The developed FBG force transducer contains a multi-layered composite superstructure (6 mm nominal diameter) and demonstrates linearity and repeatability under both dynamic impact-response calibrations and blast-loading conditions. Spectral analysis indicates that the presented transducer captures transient kinetics of blast overpressure with an average of 0.12% difference in normalized Fourier amplitudes captured by the FBG and validated reference piezo-electric transducer. Time-domain analysis indicates that the FBG force transducer is repeatable with maximum coefficient of variance for repeated measures at 7.9% whereas the validated reference transducer coefficient of variance is 9.1% (maximum), based on the normalized blast exposure data. The novel force transducer is the first application of FBG technology to measure inner skull kinetics under blast loading and can be used to evaluate the mechanisms of energy transfer into the head during blast exposure.

The newly developed transducers were then integrated into a biofidelic simulant-based surrogate model of the head and used to assess whether or not helmets and eye protection can alter mechanical measures during both blast and impact loading scenarios. Free-field blast simulations at an outdoor test range (DRDC Valcartier) were conducted to create realistic blast exposure on the head surrogate using various protection scenarios. Impact loading on the headform was created in a laboratory setting, using a linear monorail drop tower, for the cases

with a bare headform and for cases wearing a combat helmet. Specifically, inner skull forces and pressure within the brain parenchyma were investigated for the various blast and impact loading conditions and protection scenarios. Results suggest that adding head protection can attenuate the measured kinetics relative to the case when the surrogate model is unprotected, in both blast and impact. Measurements also demonstrate a propensity towards more spectral content at lower frequencies, relative to an unprotected head, for measurements nearest to the site of loading. Overall, adding head protection was found to attenuate pressure in the brain parenchyma by as much as 49% during blast and 53% during impact, and forces on the inner table of the skull by as much as 80% during blast and 84% during impact, relative to an unprotected head.

In summary, this work presents a developed transducer that is a repeatable tool with the capacity to assess inner skull kinetics during blast and impact events and therefore can be applied towards the assessment of relative headgear protection efficacy. A simulant-based surrogate headform, with integrated instrumentation, documents the mitigation of internal kinetics and shift of frequency content with the addition of protective headgear. These results are an important contribution to documenting how the skull and brain react during blast and impact loading when the head is protected relative to when the head is unprotected.

Preface

This work was financially supported by the US Department of Defence ITC Program (Contract #W911NF-16-0083), with in-kind support from Defence Research and Development Canada Collaborative Agreement (#SRE 16-023).

This thesis expresses content of the primary author and does not necessarily reflect opinions of ARL or DRDC.

Acknowledgements

Table of Contents

List of Tables

List of Figures

Chapter 1: Introduction

The issue of blast induced brain injury and the importance of studying energy transmission into the head is described in this chapter, along with the objectives and organization of this thesis.

1.1   Motivation

Traumatic brain injury (TBI) has an immense effect on the overall health of combat veterans and civilian society, with long-term physical and psychological consequences. The overall economic costs of TBIs, including medical expenses and lost productivity for all society, have been estimated to be upward of $76 billion for the United States alone [1,2]. In military demographics, rates of TBI have been rising during recent conflicts [3–7], with nearly 25% of US deployed soldiers to Afghanistan (Operation Enduring Freedom; OEF), and Iraq (Operation Iraqi Freedom; OIF) exhibiting symptoms of TBI [8–10]. For soldiers on deployment, blast exposure accounts for the vast majority of injuries sustained, with reports as high as 80% of total injuries [11–14]. Additionally, it is estimated that over 50% of head injuries that involve blast exposure are also attributable to blunt trauma [15]. This is because blast events will often launch an individual or part of their body and can induce blunt impact through collision with surrounding objects. The increased rates of blast-induced traumatic brain injury (bTBI) is considered to be partially attributed to the increased use of explosive devices in modern warfare, such as land mines, rocket propelled grenades (RPGs), and improvised explosive devices (IEDs) [16]. Effective mitigation strategies could halt or reverse the increasing rates of bTBI, but in order to accomplish this, a proper understanding of the bTBI injury mechanisms must be known [14].

The desire to understand and effectively mitigate bTBI has led towards intense research efforts on several possible injury mechanisms and evaluation methods for protective devices. Combat helmets are fielded to protect the user from impact and ballistic threats and are commonly considered to be effective at mitigating these threats [15,17–22]. Despite the efficacy of contemporary head protection towards mitigating ballistic and impact threats, bTBI rates continue to rise [14], and it appears to be unknown whether or not modern helmets are effective at protecting against blast waves. Currently, there is limited literature that exists to

address this issue and determine whether head protection is capable of altering the transmission of blast energy into the head and brain.

1.2 Thesis Objectives

The objectives of this thesis are twofold. The first objective is to design a force transducer that integrates into the interior skull of a simulant-based surrogate headform such that mechanical interactions between the simulant skull and brain can be detected. The second objective of this thesis is to use the instrumented surrogate headform, equipped with pressure transducers within the brain parenchyma along with novel force transducers on the inner skull table, to ascertain whether or not protective headgear alters the transmission of blast and impact energy into the brain.

1.3 Thesis Organization

This thesis begins with a brief overview of relevant theory and literature on blast waves and traumatic brain injury. Following that, an outline of head models that have been used for blast experiments is presented. An overview of head protection devices and how they are tested is then discussed, proceeded by a summary of optical sensing technologies and their applications towards biomechanics.

Chapter 3 documents the development and validation of an optical fibre force transducer for measuring inner skull forces during blast and impact loading. The transducer presented in this section is the first application of FBG technology towards the measurement of inner skull kinetics during blast loading. This chapter is a re-formatted version of the manuscript that has been accepted to the journal of IEEE Sensors and published on October 8, 2018 (© 2018 IEEE), titled "An optical fibre transducer for measuring kinetics of skull-brain interaction in a surrogate model of the human head subjected to blast overpressure." The first author of this manuscript is also the author of this thesis.

Chapter 4 documents the effect of contemporary protective headgear on the transmission of energy into the head and brain of a simulant-based surrogate model during blast and impact. The content in this chapter has been reformatted from a manuscript that is under preparation

for submission into the ASME Journal of Biomechanical Engineering. The first author of this manuscript is also the author of this thesis.

Finally, the concluding chapter will summarize the contributions of this thesis as well as provide suggestions for future work.

In reference to IEEE copyrighted material which is used with permission in this thesis, the IEEE does not endorse any of University of Alberta's products or services. Internal or personal use of this material is permitted. If interested in reprinting/republishing IEEE copyrighted material for advertising or promotional purposes or for creating new collective works for resale or redistribution, please go to the following link to learn how to obtain a License from RightsLink:

http://www.ieee.org/publications_standards/publications/rights/rights_link.html

Chapter 2: Background

2.1   Blast Physics

An explosion occurs from the nearly instantaneous phase change of a solid or liquid into gas form [23]. Immediately post-detonation, these converted gasses temporarily occupy the same volume as the parent solid or liquid, resulting in extremely high pressures and rapid expansion outwards in all directions away from the source. The ensuing compression of surrounding air molecules, thereby forming what is known as the shock front, propagates away from the point location of the detonation site [24]. The increase in pressure above atmospheric conditions is commonly referred to as the blast overpressure.

Blast dynamics in close proximity to the detonation site is highly complex and may involve two-dimensional wave motion, ballistics, and substantial thermal radiation effects [14]. Further away from the detonation, blast physics are much more simplistic and approximately one-dimensional. This far-field flow regime is often referred to as the "free-field" region and is typically where most blast wave injury research is focused [14].

In free-field conditions, static overpressure can be estimated using the Friedlander equation [14]. An ideal representation of the Friedlander waveform shown in Figure 1.

Initially, the shock front arrives at the observation location and pressure increases up to the peak blast overpressure nearly instantaneously. The pressure then drops exponentially and returns to atmospheric over an interval known as the positive phase. As the gases further expand, the pressure continuous to decrease, creating a relative vacuum known as the negative phase, or blast underpressure [25]. Eventually, pressure returns to atmospheric conditions after the blast wave subsides.
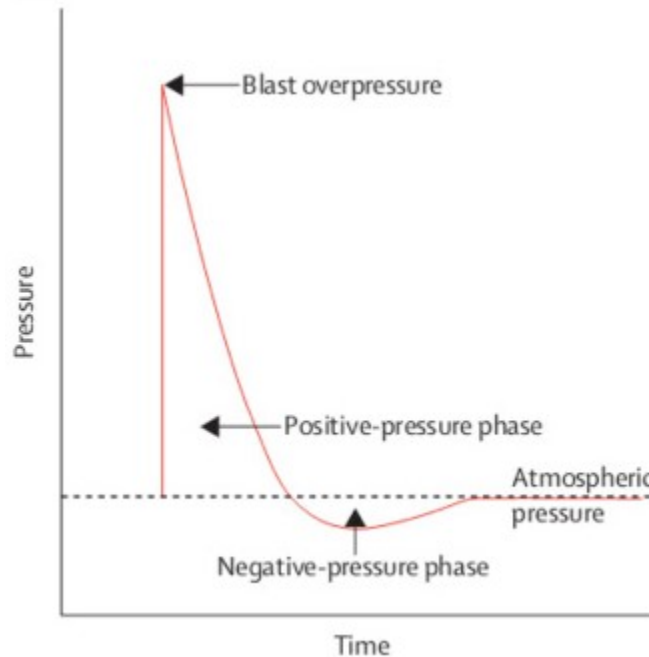
Figure 1: An ideal theoretical blast wave (Friedlander waveform) with indications of the positive and negative phases [26]. The dashed line indicates atmospheric pressure. Image used with permission from Elsevier.

The time to peak pressure during a blast event occurs over a much shorter timescale relative to kinetics measured during ballistic and blunt impact loading. Typically, the time to peak mechanics will occur in 3 to 100 microseconds for a blast wave, approximately 100 to 200 microseconds in a ballistic impact, and 3 to 50 milliseconds for blunt impact [27].

The speed of the gases moving behind the blast front is referred to the 'blast wind' and can reach velocities of several hundred miles per hour, which is greater than the wind speeds recorded during even the most severe hurricanes [26]. Although occurring for shorter durations

than a sustained hurricane wind, a blast wind can still propel objects and individuals into the air and induce a variety of injurious scenarios.

2.2   Classifications of Blast Injury

A blast event can result in many different types of injuries, which are broadly classified into four categories [14,16,26,28,29] (Figure 2). Primary blast injuries are due to the blast wave propagating through the body and damaging living tissue, also referred to as barotrauma [14]. These injuries typically affect organs containing gas or interfacing with air, such as the lungs, ears, eyes, and gastrointestinal tract [16], but the effects of primary blast on the central nervous system (CNS) remain unresolved. Secondary blast injuries occur when the explosion propels shrapnel or other debris at the victim and inducing either blunt or penetrating trauma. Tertiary blast injuries are due to displacement of an individual following a blast exposure, and the subsequent impact of the victim into surrounding structures. These injuries typically occur for individuals in close proximity to the detonation location, and can induce significant blunt trauma [16]. Quaternary blast injuries are due to thermal radiation or chemical exposure from the explosion, often manifesting as burns [14]. Typically, blast events are polytraumatic [16], implying that multiple mechanisms will induce injury simultaneously, and often multiple of the above-mentioned pathways do not occur in isolation on the battlefield.
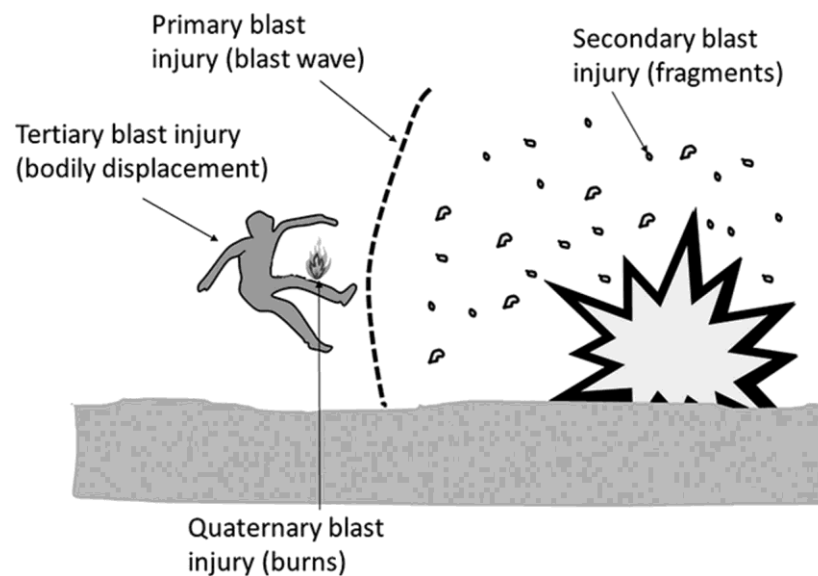
Figure 2: Classifications of injury from blast events [30]. Image used with permission from Wolters Kluwer Health, Inc.

2.3   Traumatic Brain Injury (TBI)

TBI affects the lives of millions of people around the world, with an estimated range of occurrence between 60 to 720 cases per 100,000 individuals [31,32]. Brain injuries are typically classified as either focal or diffuse, with focal injuries comprising damage to a localized area and diffuse injuries involving damage over a large generalized area [33].

Diffuse axonal injury (DAI), contusion, and subdural hemorrhage are the most prevalent forms of TBI [23], and have all been observed following a blast exposure [34]. DAI is a broad term to describe the scattered disruption of white matter tracts within the brain [35,36]. DAI is generally associated with the shearing, elongation, or bending of axons within brain matter that can result in impaired neuronal transport from focal axonal swelling and may result in axonal disconnection [35]. DAI typically manifests in the internal capsule, deep gray matter, upper brainstem, cordicomedullary junction, and the corpus callosum [36]. Cerebral contusion is the bruising of brain tissue, and is associated with microhemorrhages of blood vessels and edema within the brain parenchyma [24]. Contusions often occur in the cortical tissue, typically within the superficial gray matter of the inferior, lateral, and anterior aspects of the temporal and frontal lobes [23]. Subdural hemorrhage, or hematoma, manifests when the brain moves within the skull to an extent that ruptures bridging veins which connect the brain to the encapsulating dura mater [23,37]. This injury most commonly occurs for the frontal and parietal convexities [23].

For blast exposure, it is commonly assumed that elevated levels of internal mechanics such as intracranial pressure (ICP) will lead towards symptoms of TBI [14,38–42], however the exact thresholds or injury risks have not yet been determined for humans.

2.4 Blast TBI

Blasts are the most common cause of injury during modern conflicts, with reports as high as 80% of total sustained injuries [11,12,14,43]. The Walter Reed Army Medical Center (WRAMC) reported that out of all the individuals that sustained injuries during the Iraq and Afghanistan wars, 28% of them had a TBI [44]. Because of the polytraumatic nature of blast events, it is difficult to clinically define which forms of blast injuries are most prevalent when considering TBI [14]. Often during research, the effects of primary blast are investigated in isolation from other forms of injury such as blunt or penetrating trauma, but it is important to note that real blast events are likely to trigger multiple mechanisms. For example, it has been estimated that 50 to 60 percent of head injuries that involve blast exposure were also attributable to low-rate blunt trauma [27]. This section describes various mechanisms of bTBI that have been proposed in current literature with a specific focus on primary, secondary, and tertiary blast effects.

The effects of primary blast on the brain have been challenging to define and remain yet to be fully understood [14,45]. Current theories of primary bTBI mechanisms include transosteal wave propagation, skull orifice transmission, skull flexure dynamics, thoracic surge, and cavitation [14]. A blast wave could transmit directly into the brain through the skull by way of transosteal wave propagation [46–48], also known as the "direct cranial transmission theory," however, it is a theoretically unlikely mechanism due to the acoustic impedances of the cranium and surrounding tissue [14]. Acoustic impedance is defined as the product of density and speed of sound within a material, and a blast wave can only transmit effectively at an interface when two materials have similar acoustic impedances, otherwise the majority of the wave will be reflected. It has been demonstrated that due to the high acoustic impedance discrepancies within the human head, less than 0.001% of the blast wave would transmit through the scalp, skull, and cerebrospinal fluid (CSF) and into the brain [14]. A blast wave could also disrupt brain tissue by propagating through skull orifices such as nasal sinuses [49], auditory canals [50,51], and/or eye orbits [52–55]. Sensory organs located at these orifices are frequently injured during blast exposure [24], however a blast wave may not be able to transmit effectively into the brain through these orifices since blast waves are very sensitive to large reductions in area [14]. Even if transmission through skull orifices does not induce brain

damage directly, it could lead towards indirect brain injuries through focal injuries at the orifice. For example, disruption of cranial nerves in close proximity to the eye orbits could induce secondary brain injury effects such as neurodegeneration in the occipital visual cortex [14]. It has also been hypothesized that modes of skull flexure can be excited under blast loading [56–58], which results in elevated pressure within the cranial vault [14,59]. The blast wave travels faster through the skull relative to other human tissues, resulting in a complex strain profile surrounding the brain [14]. This mechanism could manifest as diffuse brain injury patterns [60], which has been documented in several rodent models [61–64]. This theory is supported by high-frequency oscillations in ICP that has been observed during animal [57], cadaver [65,66], and computational finite element models [58,67]. A blast wave could also propagate indirectly into the brain through vulnerable cavities in the thorax and abdomen region [14]. This theory, referred to as "thoracic surge," speculates that the rapid compression of organs within the thorax and abdomen following blast exposure can create a shock front that propagates towards the brain through soft tissue and vascular mediums [68–70]. This theory is supported by significant increases in pressure within the internal carotid artery following a thoracic blast exposure [71]. It is important to note that thoracic and abdominal injuries on the battlefield have become much less prevalent in recent conflicts due to advancements in body armor [72–74], which would also contribute towards reductions in the prevalence of the thoracic surge mechanism. Cavitation is another primary bTBI theory which postulates that regions of negative pressure within the cranial vault could yield the formation of cavitation bubbles [14]. These bubbles may damage surrounding brain tissue when they collapse [14,75]. Studies using surrogate and PMHS models found negative ICP responses following blast exposure [65,75], however further work is required to prove whether or not negative ICP actually causes cavitation. A study using an ellipsoid brain model with a transparent polycarbonate skull imaged cavitation bubbles under blast loading with ICP signals around 150 kPa underpressure [75], but this has not been fully demonstrated for biological tissue.

Understanding which bTBI mechanisms are most prevalent during a blast event, and how their prevalence may vary based on the blast loading scenario [76], can help direct the development of future protective combat headgear and ultimately mitigate the occurrence of bTBI.

2.5   Blast Surrogate Models

Surrogate models are an engineering method to provide robust and repeatable approximations to complex problems that cannot be easily examined directly. In biomechanics research, a surrogate model attempts to approximate key anatomy, in terms of shape, dimensions, and mechanical properties of human tissue, in an effort to achieve a model with a mechanical response that is similar to a human. Robustness is an important quality for a surrogate model, which requires that the model's integrity will not degrade after use which would effect future measurements. Repeatability is another important quality of a surrogate model such that repeated measurements can be expected to be similar and very high sample sizes and resources are not required when using the model. If measured mechanics within a validated model can be linked to injury, then such models can be useful in estimating the mitigation in injury risk via protective gear.

Blast headforms are surrogate models of the human head, designed to study the effect of blast exposure to the head and to evaluate the efficacy of protective headgear under blast loading. In order to have a biofidelic response to blast, it is necessary to effectively and accurately model the aspects and regions of the human head that influence blast wave transmission [16]. Material selection and geometry are important factors in developing a surrogate model with a biofedelic response to blast [16]. Several headforms have been employed for the assessment of blast loading and are briefly outlined in this chapter.

The Hybrid III is an anthropomorphic test device (ATD) developed in 1973 for use in the automotive industry, and has been used in blast experiments [16]. The headform comprises an aluminum skull and an external vinyl rubber for skin. The Hybrid III is very durable, however, it lacks appropriate biofidelity towards blast due to the lack of important internal features/materials and the wavespeed within aluminum is far greater than a human skull.

The Manikin for Assessing Blast Incapacitation and Lethality (MABIL) was designed by at Defence Research and Development Canada (DRDC) Valcartier to evaluate personal protective devices under blast loading [16]. MABIL comprises a solid urethane head, with facial features based on the Canadian Standards Association's (CSA) headform anthropometry. MABIL was instrumented with a pressure transducer in the ear canal and

another in the eye, along with a photodiode in the eye to measure light intensity during a blast event [16].

The Dynamic Event Response Analysis Man (DERAMan) headform was developed by Britain's Defence Evaluation and Research Agency [16], and was designed to suffer car crashes, sports collisions, and automotive seat ejections [77]. The DERAMan is made with a polyurethane outer skin, a skull (hard plastic – undisclosed composition) and a soft gelatinous brain (undisclosed composition). The headform is instrumented with 40 piezoelectric pressure transducers within the brain, 45 piezoelectric pressure transducers on the inner surface of the skull, two accelerometers, and one three-dimensional force gauge. The DERAMan has reportedly been used for blast experiments but results have not been published [16,77].

Johns Hopkins University (JHU) developed a human surrogate head model (HSHM) based on a finite element model of the human head [78]. The skull of this head model is composed of a glass/epoxy composite and the brain is made from Sylgard gel. The JHU HSHM has been instrumented with two pressure transducers and four displacement transducers, all within the surrogate brain material, and has been subjected to blast overpressure within a shock tube [78].

The Warrior Injury Assement Manikin (WIAMan) blast manikin was developed for studying underbody blasts to improve military vehicle design [79], however it lacks any approximation of the brain and inner skull anatomy.

The Realistic Explosive Dummy Head (REDHead) was developed at the University of Nebraska using various surrogate materials for the skin, skull, and brain [77]. The final version consisted of a polydimethylsiloxane (PDMS) skin and a polyurethane skull assembly, with an opening for the brain and CSF [80]. Water was used to model the CSF, and a silicone gel was used for the surrogate brain. The headform was instrumented with polyvinylidene fluoride (PVDF) piezoelectric pressure transducers within the brain and on the outer surface of the skull, strain gauges (Vishay MR1-350-130) on the outer surface of the skull, a micro electro-mechanical systems (MEMS) accelerometer (unreported location), and a fibre optic pressure transducer within the surrogate brain.

The Blast Injury Protection Evaluation Device (BIPED) is a simulant-based surrogate model of the human head, fully developed by researchers at DRDC Valcartier [81]. The BIPED comprises surrogate skin, skull, falx and tentorium membranes, a brain, and CSF. The surrogate skin is composed of a tough urethane rubber with facial features based on the CSA headform anthropometry [82]. The skull, nominally 6.35 mm thick, is made from polyurethane with internal features based on an available CAD model [83]. Falx and tentorium membranes are composed of neoprene sheets (70 Shore A hardness). The surrogate brain is made from a silicone gel (Sylgard 527, Dow Corning) and CSF is modelled as saline solution. The BIPED has been instrumented with pressure transducers within the brain and on the outer surface of the headform and used during free-field blast experiments [81]. The BIPED has also been directly compared to post mortem human subjects (PMHS) within a shock tube and results suggests similar responses in terms of ICP both in magnitude and frequency [66].

2.6   Head Protective Devices

Helmets are commonly attributed as being the primary protection device for the head. In the military, combat helmets have been shown to be effective at protecting the wearer from impact and ballistic threats [15,17,84–89]. Originally, combat helmets comprised a formed steel bowl with a web-based suspension system [90] and were widely employed during World War I. Today, modern combat helmets involve the use of light-weight and high strength fibrous materials, such as Kevlar 129 or Twaron [90], with a phenolic resin, along with an elastomeric foam suspension system.

Helmets for both sport and military purposes are all designed to protect the wearer from relevant environmental threats, while constrained to being sufficiently lightweight and ergonomic in order to not inhibit performance or morale. During ballistic and blunt impact, helmets are designed to mitigate the energy imparted to the head and reductions in energy transmission to the underlying head is generally associated with reduced risk of head injury. The outer shell of the helmet protects the head from focal damage through deformation of the shell material and redistribution of the loading over a larger area. The inner liner of the helmet further attenuates the re-distributed energy transmitted from the shell and provides an

ergonomic interface for the user. For sport helmet certifications, which focus on protecting the wearer from blunt impact, helmets are traditionally evaluated by their ability to attenuate linear head acceleration below a threshold value [91–93]. Modern combat helmets are tested by their ability to mitigate ballistic penetration and behind-helmet blunt trauma (BHBT), as well by their ability to withstand other environmental stressors such as exposure to temperature extremes [14]. The mitigation of mechanics under blast loading is lesser documented compared to ballistic and impact loading.

In combat scenarios, no existing protective headgear is able to completely protect the wearer against all the potential threats that can exist on the battlefield [58]. Combat helmet certifications do not currently have a paradigm for directly mitigating bTBI, yet it is commonly assumed that protecting the wearer against other threats, such as ballistics, will also provide protection from blast. With the current state of biomechanics research, the extent of validity for that assumption remains unknown. However, despite the efficacy of modern combat helmets in mitigating injury from ballistic threats and impacts, bTBI rates continue to rise [65], and it appears to be an open-ended question whether or not modern combat helmets are effective at protecting military personnel from blast waves.

2.7   FBG Technology and Applications Towards Biomechanics

Fibre Bragg gratings (FBGs) have become increasing popular in recent years for sensing applications within the field of biomechanics [94], in addition to a wide range of other applications [95]. FBGs offer attractive advantages such as biocompatibility, small size, light weight, chemical inertness, immunity to electromagnetic interference, and capacity for multiplexing [94,96].

Fibre-optic sensors operate by modulating properties of light, such as intensity, phase, polarization, and frequency, in response to specific environmental stimuli. Optical fibres consist of a core, cladding, and will often also have a buffer coating and protective jacketing. The core is a very thin strand of glass where signals in the form of light are transmitted through. The cladding surrounds the core and is composed of a higher refractive index material than the core. This mismatch of refractive indices causes light to reflect back internally within the core

and allows for transmission of light with minimal losses. This phenomenon is known as total internal reflection. An outer coating and other protective layers are often employed to guard the optical fibre from any harsh external conditions.

FBGs are the most widely employed type of optic fibre sensing technology, and are particularly common among the research community [97]. Other forms of optical sensing technology include interferometry, scattering, faraday rotation, luminescence, blackbody, fibre optic gyroscope (FOG), among others [97]. FBG technology was discovered accidentally in 1978 at the Canadian Research Center in Ottawa [98]. Just over a decade later, improved fabrication methods for the gratings were developed [99], allowing for more intensive research to follow. Many forms of gratings exist (uniform, long-period, chirped, tilted, sampled [97]), however FBGs all operate based on the common principle of reflecting specific wavelengths of forward propagating light from the source to a backwards propagating mode through the core and sometimes through the cladding. The reflected spectrum of the backwards propagating light can be interpreted using a form of wavelength interrogation or demodulation technology. The peak of the reflected spectrum is known as the Bragg wavelength, λ_B.

For uniform FBGs, the grating period Λ, or the distance between similar edges of one grating to another, is constant and the reflected light is transmitted back through the core of the fibre. The reflected Bragg wavelength changes as a function of the grating period Λ and the effective refractive index of the core, n_{eff}, as follows [97]:

$$\lambda_B = 2n_{eff}\Lambda \qquad\qquad\qquad (i)$$

FBGs are useful for sensing applications because when the gratings are subjected to strain or temperature, the grating period will change, resulting in a shift in the Bragg wavelength based on the above equation. Multiple sets of Bragg gratings can be fabricated within a single optical fibre, each with a distinct Bragg wavelength, allowing for distributed measurements along the length of a fibre. Transducers based on FBG technology have been developed and employed to measure a wide variety of physical parameters such as strain [100,101], temperature [102,103], pressure [104], force [105,106], and refractive index [107].

Chapter 3: An optical fibre transducer for measuring kinetics of skull-brain interaction in a surrogate model of the human head subjected to blast overpressure

The following manuscript has been accepted to the journal of IEEE Sensors and published on October 8, 2018 (© 2018 IEEE). The first author of this manuscript is also the author of this thesis.

3.1 Introduction

Before measurement of skull kinetics during blast can be achieved, a novel transducer needs to be developed and integrated into the BIPED. This chapter describes the development, calibration, and validation of the optical fibre force transducer for blast and impact measurements, along with the integration of the transducer into the BIPED. This transducer is the first application of FBG technology towards the measurement of inner skull kinetics under blast loading, and can be used for evaluating the mechanisms of energy transfer into the head.

3.2 Background

Mild traumatic brain injury (mTBI) has become increasingly prevalent among personnel in the armed forces over recent years [3,108–110]. This has been partially attributed to the increased use of explosive devices in modern warfare [16], including devices such as land mines, rocket propelled grenades (RPGs), and improvised explosive devices (IEDs). While the mechanisms of injury are not universally agreed upon, exposure to these devices can lead to injury through: (1) an overpressure wave that couples energy into the torso and head; (2) high velocity projectiles and fragments that can cause severe penetrating injury; and (3) displacement of the head and torso by overpressure, leading to acceleration/deceleration injuries and possibly blunt impact, which can cause both focal and diffuse tissue damage. The underlying mechanisms of these three exposures, in particular exposure to blast overpressure, that lead to brain injury are as yet not completely understood despite the wealth of clinical and pre-clinical research that is available [23,111,112]. The fact that underlying injury mechanisms are not completely characterized is potentially worrisome because statistics indicate rates of mTBI are elevated in warfighters and could be increasing [108]. A retrospective study from 1997 to 2007 looking at mild traumatic brain injury (mTBI) in US warfighters indicated 98,012

mTBI injuries over the decade with an average increase of 8.5% per year [108]. Prevention strategies could halt or reverse the increasing trend, but to prevent an injury the mechanisms must be understood.

The desire to understand and ultimately prevent blast-induced brain injury has led to intense research efforts focusing on both injury mechanisms and protection devices. It is generally accepted that the mechanism of injury comprises both mechanical and biological factors. Specific to mechanical factors, it has been hypothesized that overpressures can couple energy into the brain and through various mechanisms result in tissue damage [16]. This coupling could lead to elevated pressure in cerebrospinal fluid spaces and stress in brain tissue, both of which could be relevant in brain injury. This hypothesis has led to biomechanical studies using animals and post-mortem human subjects, both of which have confirmed that exposure to blast can significantly elevate pressure and stress in the anatomy of the brain [113,114]. At the same time, research using small animal models has examined the role of blast overpressure in the onset and long-term cascade of biological processes that characterize brain injury. This research also suggests the mechanics of the overpressure are relevant in the onset and progression of the complex biological processes of brain injury [11]-[12]. As a result of this research, the mechanics of overpressure exposure and the stress that it can create in the brain has been a focus for researchers attempting to develop repeatable models with which protective headgear can be tested.

The majority of mechanical models used in assessing protection devices attempt to recreate the mechanics of the human response to an injury event and, through instrumentation, measure mechanics that quantify injury risk mitigation. A contemporary example of this paradigm is mechanical models of the human head used in the assessment of sport helmets. These head models recreate the physical size and mass of human heads and measure head accelerations, which is thought to relate to risk of severe focal head injury (the injury that sport helmets are credited with preventing [18,117–119]). Head models for blast include the Dynamic Event Response Analysis Man (DERAMan) [16], Johns Hopkins Human Surrogate Head Model (HSHM) [16], the Realistic Explosive Dummy Head (REDHead) [77,80], and the Blast Injury Protection Evaluation Device (BIPED) [66,76]. Developed for military blast injury investigations, the Warrior Injury Assessment Manikin (WIAMAN) lacks any approximation

of the brain and inner skull anatomy. Pioneered by Defence Research and Development Canada (DRDC), MABIL was designed to measure only blast pressure at the mouth and ear canal. The British contributed the DERAMan headform, but to-date there has been no data released for this model. The Applied Physics Laboratory (APL) of Johns Hopkins University developed an experimental head-brain model and a computer model designed to match experiment measurements [78].

The BIPED, again designed by researchers at DRDC, comprises skin, skull, falx and tentorium membranes, a simulant model of the brain, and a fluid layer between the skull and brain. This model is designed to measure pressures on the head exterior and within the brain parenchyma [66]. The BIPED also measures global head acceleration to allow quantification of inertial loading of the head and brain. In this paper, we present research on the development of an optical transducer system to measure interaction kinetics between the skull and brain within the BIPED. These transducers quantify the transient forces that occur between the skull and brain, which can lead to compression/tension in brain tissue. Skull interaction and resulting compression of brain tissue is a known mechanism for brain injury [38,120–122] and therefore it is desired that the BIPED have instrumentation capable of quantifying mitigation of this mechanism.

This manuscript presents a transient force transducer for detecting contact force between the BIPED simulant skull and brain. The transducer is built around an optical approach using in-fibre Bragg grating (FBG) technology. Our research group previously reported on transient force transducers designed specifically for characterizing forces applied on the head exterior by protective sport helmets subjected to low speed blunt impact [105]. The work presented in the current manuscript is an advancement of these previous efforts and builds upon our previous work by developing a transducer that: is physically smaller than previous variants, is amenable to being arrayed within the interior (not exterior) of head models within simulated cerebrospinal fluid layers, and perhaps most importantly, is verified to be capable of resolving force transients that occur over much shorter timescales (typical of blast) than blunt impact force transducers that we have previously reported on utilizing FBG technology.

FBGs comprise a short segment of an optical fibre, typically 1mm to 10mm, in the core of which a periodic modulation in refractive index is created. In single mode optical fibre,

coherent light travels through the core and when it encounters an FBG, a single-peaked spectrum of light is reflected and propagates back towards the light source. This spectrum has a center wavelength called the Bragg wavelength, λ_B. The Bragg wavelength can be predictably modulated when the fibre length corresponding to the FBG is exposed to, among other parameters, mechanical strain and temperature. If the FBG is contained in a transducer that can convert a given measurand (e.g. pressure, force, humidity) to strain, then λ_B can be used to indicate the magnitude of the given measurand. Knowledge of this transduction approach and the fact that FBGs possess highly desirable characteristics including biocompatibility, potentially high frequency response, immunity to harsh environments and electromagnetic interference, along with the capacity to be multiplexed allowing spatially distributed measurements, has led the authors and other researchers to apply FBGs in basic and trauma biomechanics [94]. In the present work, we exploit extremely small size and compatibility with liquid that is offered by optical fibre to develop a force transducer that is small enough to be implanted into the inner table, in contact with fluid, of a physical model of the human head.

The specific objective of this work is to design a transducer that integrates into the interior skull of the BIPED such that mechanical interaction between a simulant skull and brain can be detected as contact forces. Strain-optic and linear elastic numerical modeling is used to predict transducer sensitivity and to examine the mechanical resonances of the transducer, respectively. Calibration experiments that expose the transducer to impact force and blast overpressure demonstrate that the transducer is capable of detecting mechanics over the range of frequencies characteristic of dynamic blast overpressures. Finally, exemplar measurements of skull-brain contact force from a single exposure of the BIPED to an incident blast wave are presented to verify the FBG transducer functions in its proposed application (in-situ).

3.3   Methods

3.3.1   BIPED Geometry and Instrumentation

Developed by the Weapons Effects and Protection section of DRDC-Valcartier, the BIPED is a reusable anthropomorphic model of the human head with several biofidelic features. Mechanical and physical properties for the BIPED are presented in previous literature

[81]. Here, we present an overview of the physical and mechanical properties and instrumentation that are relevant to the presented work. Surrogate materials were selected based on their mechanical and physical properties, in order to exhibit a biomechanical response to blast loading that is similar to literature for brain, skull, and soft tissues. External headform geometry (Figure 3a-c) was engineered with anthropomorphic eye orbits, nasal cavities, a jaw, and an upper skull geometry that matches the ISO Size J Headform (e.g. Model SB070, Cadex Inc., QC Canada). The BIPED can be mounted onto a Hybrid III neck assembly, which acts as a mechanical model of the adult human neck that is commonly applied in injury biomechanics research [123–125]. Internal features were constructed using an available human skull model (Anatomium 3D, 21st Century Solutions Ltd., CA United States). Water is used to simulate cerebrospinal fluid layers between the skull and brain, which play an important role in the mechanics of the brain in impact and blast events. Falx and tentorium membranes are also important in the mechanical response of the brain and are modeled using polymer layers (Neoprene, 70 Shore A hardness) [126]. The brain surrogate (Figure 3d) is composed of homogenous Sylgard 527 (Dow Corning Corporation, MI United States) and consists of two hemispheres and a cerebellum. The surrogate skull is composed of TC-854 A/B polyurethane (BJB Enterprises Inc., CA United States), with nominal skull thickness of 6.35mm. The scalp soft tissue layer is composed of a urethane rubber (Vytaflex 20, Smooth-On Inc., CA United States). Biofidelity of the BIPED has been tested in experiments where both the BIPED and isolated heads from post-mortem human subjects were subjected to dynamic overpressure [66]. In these trials, pressure was measured in the brain parenchyma using modified Kulite piezo-resistive pressure sensors (XCL-062, Kulite Semiconductor Products Inc., NJ United States). External overpressure measurements (Kulite LL-125 flat line series) and global headform accelerations (PCB 350C02 linear accelerometers, NY USA) have also been monitored during blast trials on the BIPED [81]. The force transducers developed in this work will reside at the inner surface of the skull to measure the contact force between the brain and skull within the BIPED (Figure 4).
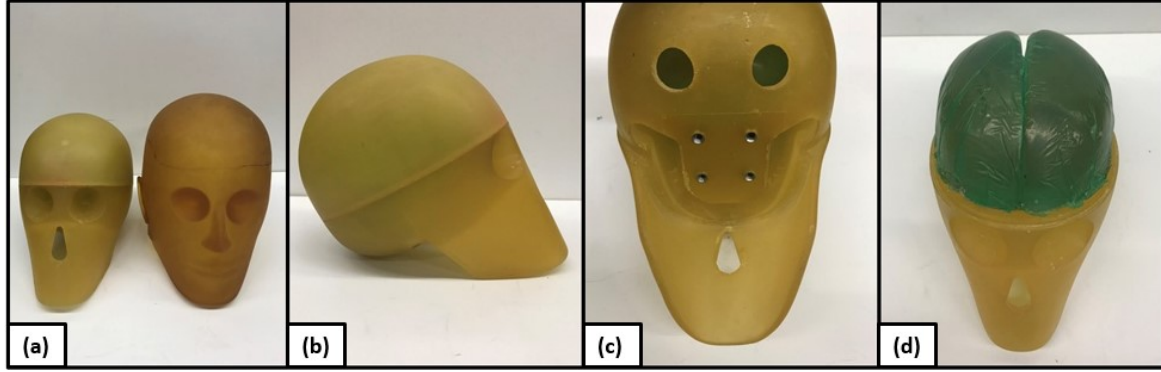
Figure 3: **From left to right - (a) Frontal view of the BIPED skull and scalp soft tissue layer. (b) Side view of the BIPED skull. (c) Bottom view of the BIPED skull showing the 4-point attachment location for the Hybrid III neck. (d) Top view of the BIPED skull with the skull cap removed and the surrogate brain material exposed. Permissions for reproduction of this figure were granted by IEEE.**

3.3.2   Force Transducer Design and Optical Instrumentation

The optical force transducer is fabricated using an in-fibre Bragg grating (FBG) embedded within a multi-layered superstructure (Figure 4) composed of aluminum (6061-T6 alloy) and an acrylic-based photopolymer (VeroGray RGD850, Stratasys Ltd., MN United States). The upper and lower polymer layers are 1.15 mm and 0.85 mm thick, respectively, while the aluminum layer is 1 mm thick. The fully assembled transducer superstructure has an overall height of 3 mm and diameter of 6.3 mm. An industrial silane adhesive (Loctite MS 930, Henkel AG & Co., Germany) is used to bond the aluminum and polymer layers together at their points of contact. The present transducer design houses a 1550nm centered Bragg grating (Technica Optical Components LLC., GA United States), with a full-width at half maximum (FWHM) of 1.5nm, a grating length of 1mm, and a 60% nominal reflectivity.

Force applied to the transducer, as shown in Figure 4, is transmitted to the aluminum layer, creating strain in the center beam. Positioning the optical fibre along the beam component of the aluminum layer (Figure 4), with the active sensing region (i.e. the Bragg grating) in the center of the beam, allows for force transmission to induce linear bending of the aluminum beam and thus linear strain along the FBG. The peak shift of the Bragg wavelength, $\Delta\lambda_B$, for a uniform FBG under longitudinal mechanical strain, ε, can be calculated as [127–130]:

$$\Delta\lambda_B = \lambda_B \left\{ 1 - \left(\frac{n^2}{2}\right) [p_{12} - v(p_{11} + p_{12})] \right\} \varepsilon \qquad (1)$$

Where p_{11} and p_{12} are components of the strain optic tensor, v is the Poisson's ratio for silica glass, and n is the index of refraction. Assuming common values for germanium-doped silica, which is typically used for FBG manufacturing, gives values of $p_{11} = 0.113$, $p_{12} = 0.252$, $v = 0.16$, and $n = 1.45$ [129]. This expression does not account for thermo-optic effects on the Bragg grating, which is appropriate for the isothermal conditions in which the presented transducer is characterized. Using this model, we can predict the Bragg wavelength shift for a given range of FBG strain, and thus estimate the transducer sensitivity, in units of picometer (pm) of Bragg wavelength change per newton force applied to the transducer (pm/N), over that range.

The optical fibre is directly bonded at both outer edges of the aluminum bridge using the Loctite MS 930 epoxy. The overall transduction mechanism of this transducer is therefore converting an applied force upon the flat surface of the superstructure into a shift in the Bragg wavelength. The Bragg wavelength shift for this study is monitored at 62.5 kHz using a Bragg grating interrogator (SmartScan, Smart Fibres Ltd, UK), which is a dual purpose instrument that supplies light to the Bragg grating transducers and also detects shift in their reflected Bragg wavelength.

This transducer is designed to be mounted flush with the inner surface of the BIPED skull (Figure 4), which requires skull material removal for the transducer to be integrated. In order to not compromise the structural integrity of the skull material adjacent to the transducer locations, and also not affect the frequency response of the headform, the overall height of the transducer is limited to 3mm, which is less than half of the surrogate skull nominal thickness of 6.35mm. The transducer width is 6.3mm such that the transducer can fit within a ¼'' (6.35mm) wide blind-hole. The presented transducer design is 50% smaller than our previously reported transducer [105].
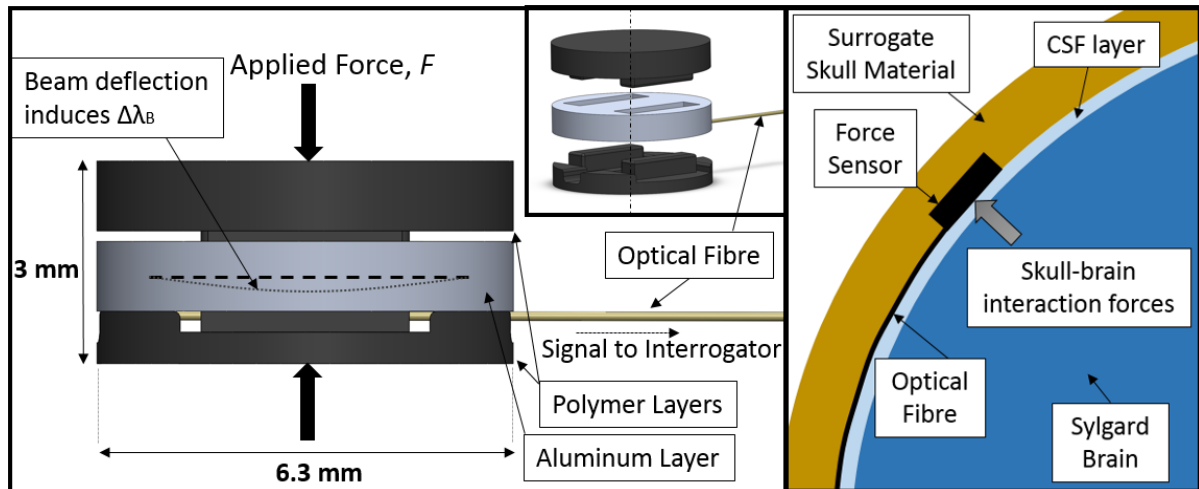
Figure 4: (a) Transducer assembly and key dimensions, indicating the position of the FBG and force transmission. **(b)** Schematic of the FBG force transducer located within the BIPED. Permissions for reproduction of this figure were granted by IEEE.

3.3.3 Finite Element Modelling

The mechanical resonance of the transducer was estimated using structural Finite Element (FE) analysis (ANSYS AIM 19.0, ANSYS Inc., PA United States). The purpose of this analysis is to verify that the frequencies observed during blast loading are sufficiently low in comparison to the first resonance of the transducer, such that blast loading will not induce resonance in the FBG force transducer. The FE model is designed to match the physical dimensions of the transducer, using 6061 Aluminum Alloy (Young's Modulus = 69 GPa) for the aluminum layer and a custom plastic (Young's Modulus = 2 GPa, based on a Stratasys polyjet material catalogue) for the VeroGray rigid opaque polymer components. Bonded contact set connections model the contact interfaces between the three layers of the transducer, as shown in Figure 5. The optical fibre bends away from the superstructure in application, but for simplicity in the simulation, it is treated as a perfectly horizontal remote mass, with material properties of silicon dioxide (Young's Modulus = 67 GPa). The bottom layer, which in application will be resting against the BIPED skull, is modelled as fixed along all degrees of freedom. All other surfaces within the model are modelled to move freely. Using a mesh composed of linear tetrahedral solid elements (4 nodes per element), the number of nodes was doubled iteratively until the lowest mode of resonance changed by less than 0.5% of the previous magnitude. This resulted in a final mesh with a maximum element face size of 0.25 mm and 52,466 nodes.

The same FE model and mesh is used to estimate the force sensitivity of the transducer (Figure 6). Compressive loads are simulated from 0 N to 100 N in 10 N increments, applied uniformly upon the upper surface of the model, and the strain at the nominal FBG location is determined. Equation (1) is used to predict the shift in Bragg wavelength based upon the computed FBG strain, which, in conjunction with the applied loading, can be used to assess the model-predicted force sensitivity of the transducer.
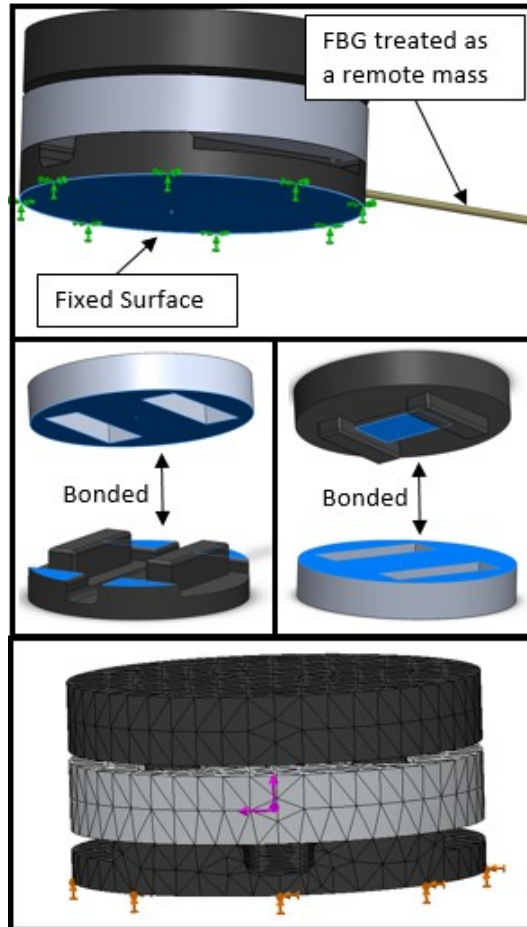
Figure 5: Finite element model boundary conditions and mesh (a coarse mesh is used here for better visualization). Visual indicators are displayed on top of the solid model to indicate the applied structural conditions. Permissions for reproduction of this figure were granted by IEEE.
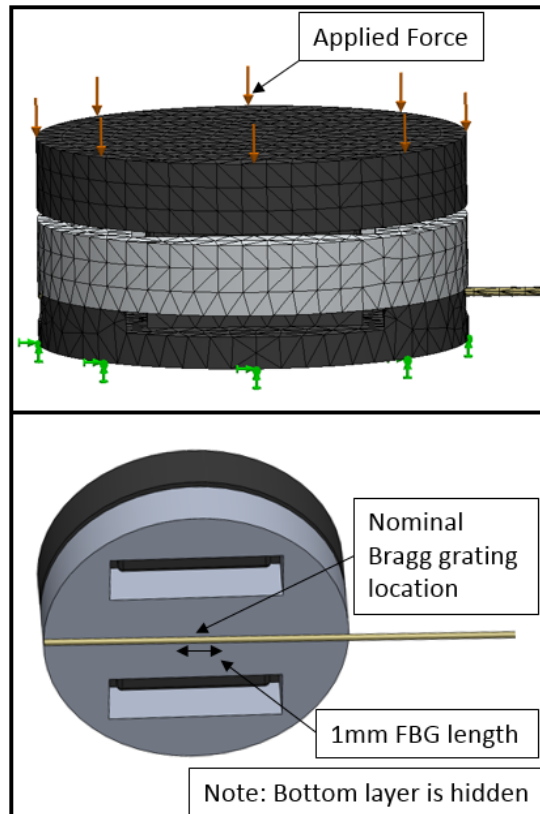
Figure 6: Finite element model used to determine strain at the nominal FBG location. Visual indicators are displayed on top of the solid model to indicate the applied structural conditions. Permissions for reproduction of this figure were granted by IEEE.

3.3.4 Calibration Experiments

We first calibrate the force transducer for impact forces, using an impact-response calibration that applies forces over a range which we speculate the skull could apply to the brain due to relative skull-brain motion during blast. Then, we subject the transducer to a simulated blast overpressure, to confirm that the force transducer captures all frequencies of interest in blast loading.

3.3.5 Impact-Response Calibration

Calibration is required to develop a relationship between the shift in peak reflected wavelength and the force applied to the transducer. In this study, the FBG force transducers are dynamically calibrated using an impact-response calibration method [36], [37], which involves dropping an impactor of known mass onto the force transducer. The experiment is shown in Figure 7. The spherical impactor (5kg total falling mass) has a single-axis linear

piezoresistive accelerometer (Xiamen Niell, Model CAYZ147V-2-2KA, China) attached so that vertical acceleration of the mass can be accurately recorded. Acceleration of the impactor is used to calculate the dynamic loading applied to the transducer, using Newton's second law of motion. The FBG transducer is fixed upon a Modular Elastomer Programmer (MEP) pad, positioned directly underneath the impactor, and as close as possible to the vertical axis of the accelerometer. The accelerometer is wired to a custom-built amplifier, containing an analog anti-aliasing filter and a programmable gain amplifier. The analog output signal from the amplifier is then directed to a data acquisition system (National Instruments, PXI-6251, TX USA), with a custom LabView program that was developed to initiate data collection from the accelerometer at a sampling rate of 100 kHz.

The applied forces on the transducer nominally range from 0 N to 100 N. Transducer data is filtered using a 4th order low-pass Butterworth filter with a cut-off frequency of 1000 Hz. The signals collected from the accelerometer and Bragg transducer are aligned using signal correlation and post-processed (MATLAB R2016b, MathWorks, MA United States) to compute the dynamic transducer sensitivity.
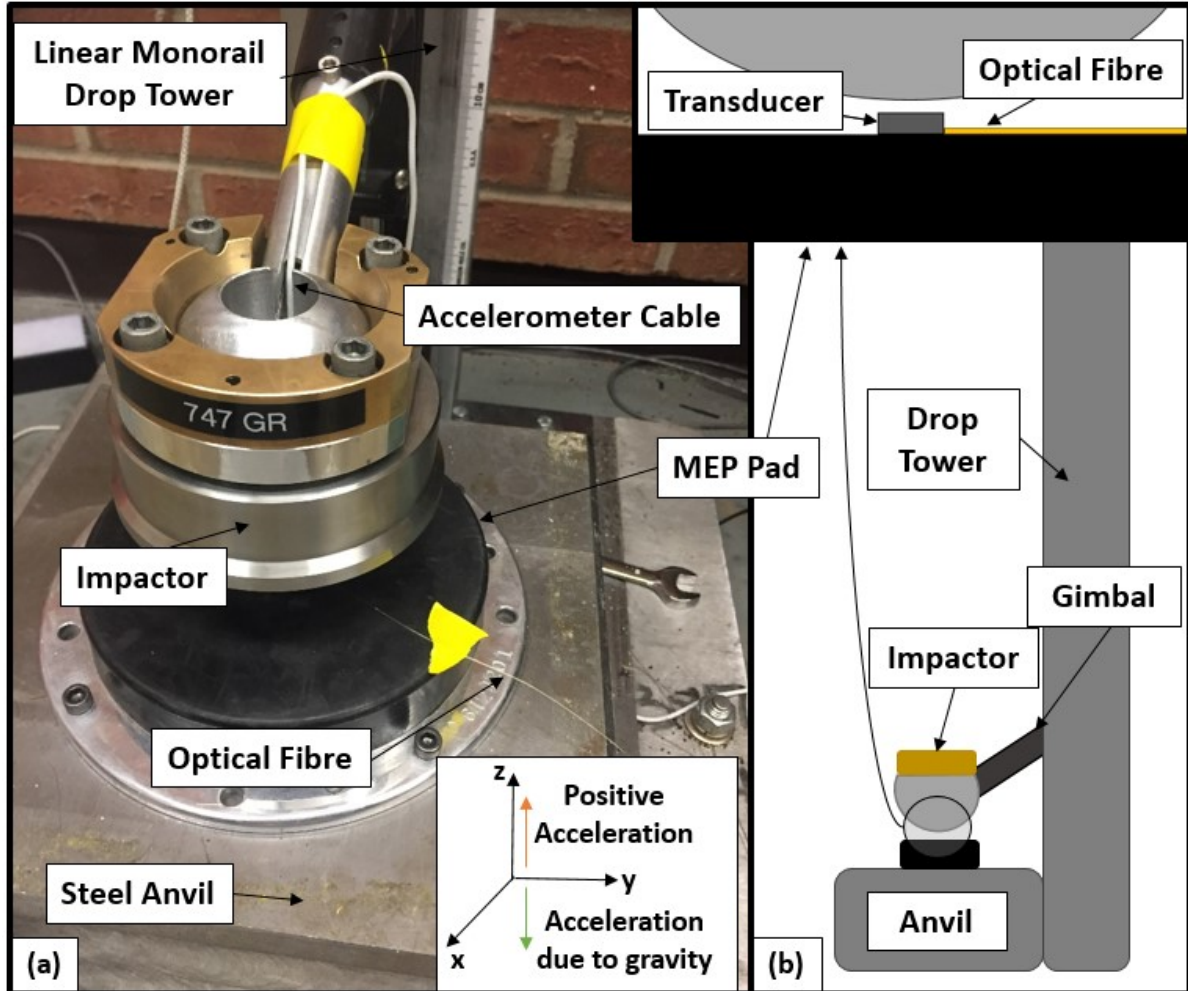
Figure 7: (a) Experimental set-up for an impact response dynamic calibration. (b) Schematic of the drop tower and close-up of the transducer position. Permissions for reproduction of this figure were granted by IEEE.

3.3.6 Blast Exposure Simulation

A custom-built advanced blast simulator (ABS; approximately 30.5 cm in diameter and 5.79 m in length; see Figure 8), located at DRDC Suffield Research Center (Medicine Hat, AB Canada), is used to produce simulated blast overpressure. The ABS utilizes a divergent driver section designed to reproduce the correct waveforms for static and dynamic pressures within a blast shockwave [38]. The ABS operates by pressurizing the driver section with helium gas, separated from ambient-pressure conditions by a polymer diaphragm. The diaphragm eventually ruptures as the driver pressure increases, thereby releasing the high-pressure gas down the length of the ABS, simulating the front of a blast wave. Computer-controlled pressurization of the helium gas and manual insertion of pre-determined thicknesses of

reinforced cellulose acetate sheets (collectively forming the polymer diaphragm) allow for control over the intensity of the shock front in order to achieve the required target overpressure.

For this work, a steel end plate is fixed to the end of the ABS, and contains five open holes in it (see Figure 8). The larger center hole is left open to the external environment, while the four outer holes were all filled to be flush with the inner surface of the ABS. Two of these four holes are used to position the presented design for FBG transducers within the steel end plate, mounted flush with the inner surface. Custom-built polymer components were designed to house the transducers within these holes, and to wire the optical fibre out of the ABS. A third hole in the steel plate is used for a reference pressure sensor (Model 133A28, PCB Piezotronics Inc., NY United States) spaced at an equal distance from the center and also mounted flush with the inner surface. This PCB pressure transducer is used for comparison with FBG force transducer results in terms of time-domain traces and frequency domain profiles. FBG transducer data is collected by the SmartScan wavelength interrogator at 62.5 kHz, while PCB pressure transducer data is collected at 500 kHz. Both force and pressure signals were filtered using a 4th order low pass butterworth filter with a 10 kHz cutoff frequency [39].
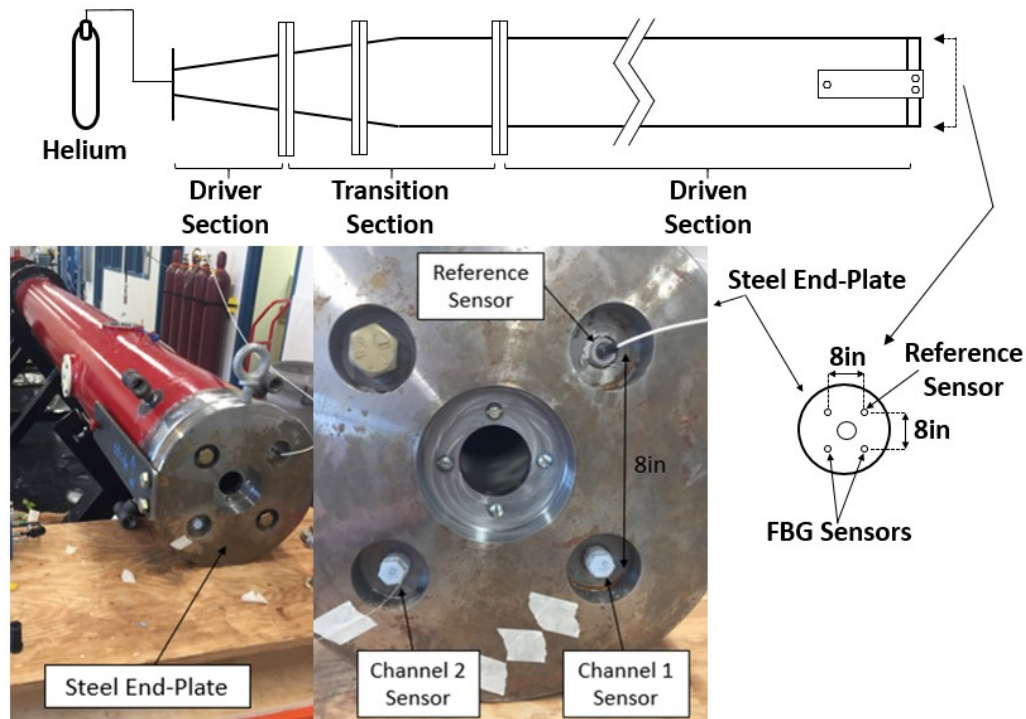
Figure 8: Schematic and photographs of the ABS, indicating the positions of the FBG transducers and the reference transducer. Permissions for reproduction of this figure were granted by IEEE.

3.3.7 Free-Field Blast Experiment

An FBG force transducer was integrated into the frontal region of the BIPED headform, located as shown in Figure 9 (also described in Figure 4), approximately 15mm above the transverse plane located just above the eye sockets). A Kulite XCL-072 was molded into the Sylgard 527 surrogate brain material at the approximate location shown in Figure 9 and used to monitor intracranial pressure (ICP) in the frontal region. The ICP transducer is located in roughly the same plane as the FBG transducer and approximately two-thirds of the distance away from the center of the BIPED towards the front of the skull (based on an x-ray image of the instrumented surrogate brain).

We performed a free-field blast trial using a 5kg C4 charge detonated at a height of 1.5m from the ground. The un-protected (un-helmeted) BIPED is positioned (measuring from the nose on the urethane soft tissue layer) at the same height as the charge, with a 5m standoff distance. A Hybrid III neck (Humanetics ATD, Farmington Hills MI), fixed rigidly at the lower-neck to a steel pole, connects at the upper-neck to the base of the BIPED, and positions the surrogate headform such that it rests vertically and facing towards the charge.
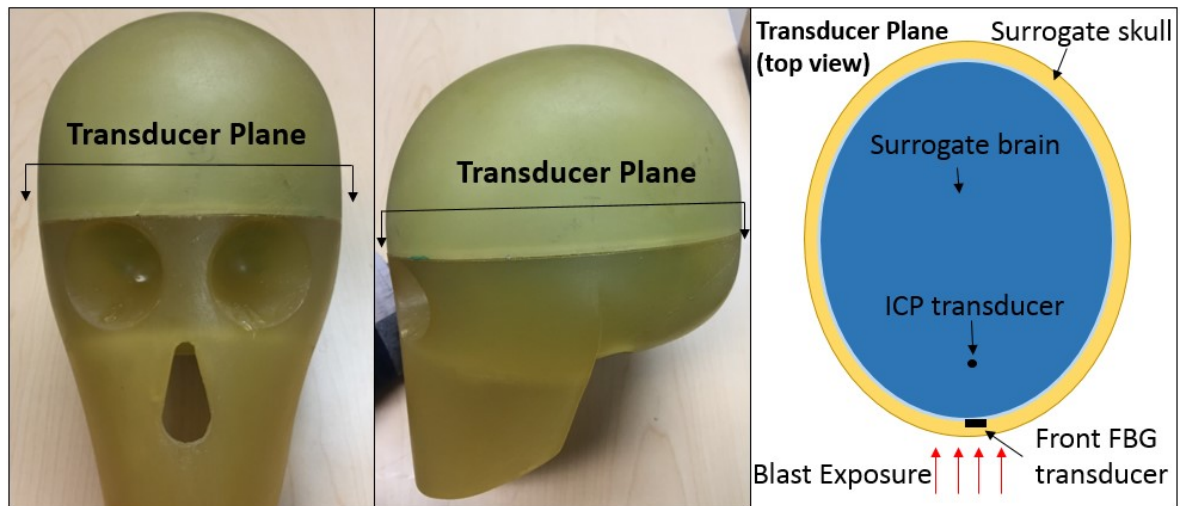
Figure 9: Image of the BIPED with a cross-sectional planar view of the instrumentation integrated within the headform. Permissions for reproduction of this figure were granted by IEEE.

3.3.8 Statistics

From the impact calibration experiments, force transducer sensitivity is determined using the least squares method. Force is the independent variable and Bragg wavelength shift is the predicted or the dependent variable, with sensitivity as the predicted slope in the data (reported in units of pm/N). The coefficient of determination, R^2, is reported for each calculated sensitivity and is interpreted as how well the linear model predicts the dependent variable (R^2 ranges from 0 to 1, with 1 being an ideal model). Mean and standard deviation for transducer sensitivity are calculated based on the results from three drop trials (n = 3), and repeated for three transducers.

From ABS experiments, the mean, standard deviation, and coefficient of variation (COV) of peak measurements are calculated for both FBG force transducer results and PCB pressure sensor results, along with the driver overpressure. For comparing spectral results, the average normalized FFT magnitude, root mean square (RMS) difference, maximum deviation, and the ratio of RMS to average FFT magnitude are reported. The mean and standard deviations of these are also presented.

3.4 Results

3.4.1 Numerical Prediction of Mechanical Resonance

The ANSYS FE modal analysis predicts a first mechanical resonance for the force transducer at approximately 24.8 kHz, and the mode of deformation associated with this resonance is shown as the insert in Figure 10, with exemplar data from FBG transducer #1. This figure also shows the strain optic model predictions for Bragg wavelength shifts as a function of applied loading. The model predicts a force sensitivity of 16.6 pm/N with R^2 greater than 0.99.
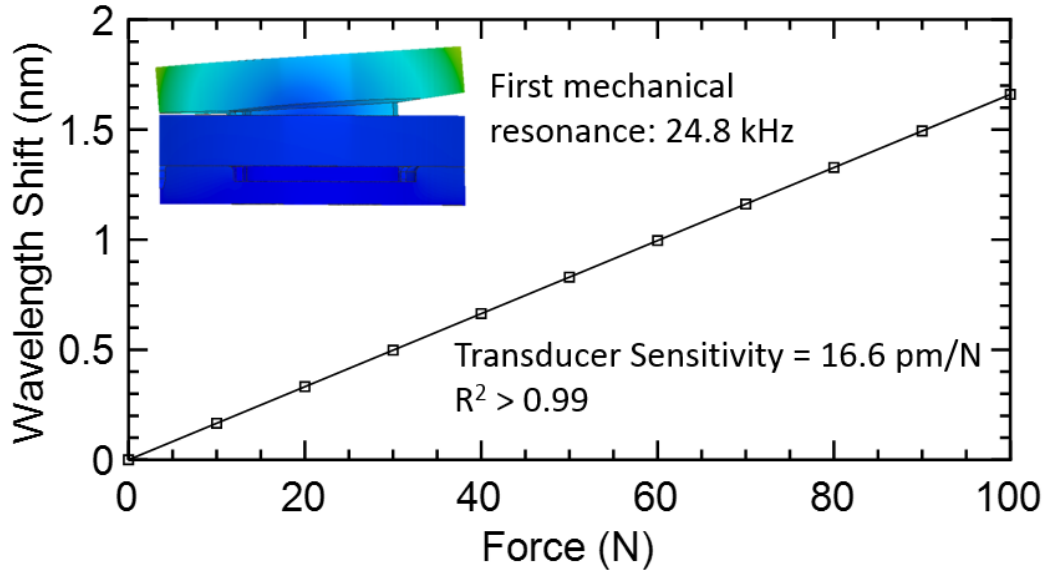
Figure 10: Modal analysis result for the first mechanical resonance of the transducer and strain optic predictions for transducer sensitivity. Permissions for reproduction of this figure were granted by IEEE.

3.4.2 Dynamic Calibration Results

From the impact-response calibration method, typical force versus time and typical wavelength versus time plots are shown in Figure 11. Subsequent peaks at lower amplitudes are due to rebounding and subsequent impacts of the impactor, resulting in the damped oscillatory behavior observed.

Plotting the rising edges of the initial impact peak for both wavelength shift and force against each other, up until a peak wavelength shift of approximately 1 nm, is shown in Figure 10 for three transducers. The average sensitivity from the three transducers in Figure 12 is 19.7 pm/N, which is within 16% of the model predicted sensitivity of 16.6 pm/N. Sensitivity, standard deviation, and R^2 for individual calibrations of the three transducers (n = 3 for each) are tabulated in Table 1. Full scale uncertainty (F.S.U.) represents the standard deviation in force, based upon the standard error (i.e. one standard deviation) of the calibration, relative to a force output of 10 N (i.e. the full scale output based on the results shown later in section D). Stated another way, F.S.U. conveys a +/- range on force about the magnitudes shown in Figure 14 that the true force value is expected to lie within.

Spectral results from the discrete Fourier transform of the transducer outputs and accelerometer readings (normalized with respect to the maximum amplitude in the trial) are shown for a sample trial in Figure 13. Similar spectral results were found for different trials with the same transducer, as well as for other transducers. To analyze the repeatability from dynamic calibrations in the frequency domain, the RMS difference between normalized force and wavelength Fourier amplitudes are tabulated in Table 2. The average of normalized force Fourier amplitudes are also reported, along with the maximum deviation between force (F) and wavelength (WL) normalized magnitudes in the frequency domain. The Fourier analysis associated with impact calibration (Figure 13) showed amplitudes in applied force signals that were less than 1000 Hz (<4% of the frequency at first resonance), suggesting that based on the dynamics of the transducer, the impact loading experiment could be viewed as quasi-static. Therefore, we did not complete static calibration experiments where loads were incrementally applied to the FBG transducer.
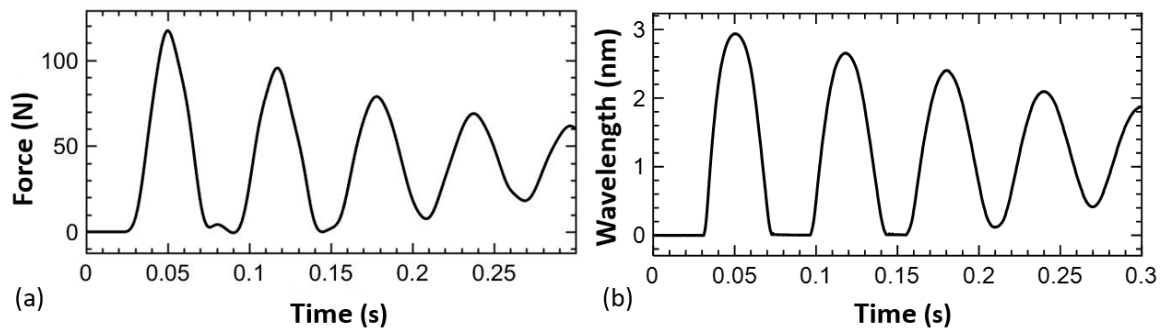
Figure 11: (a) Typical impact force applied to the FBG transducer plotted against time, and (b) the corresponding impact-induced wavelength shift vs. time. Permissions for reproduction of this figure were granted by IEEE.
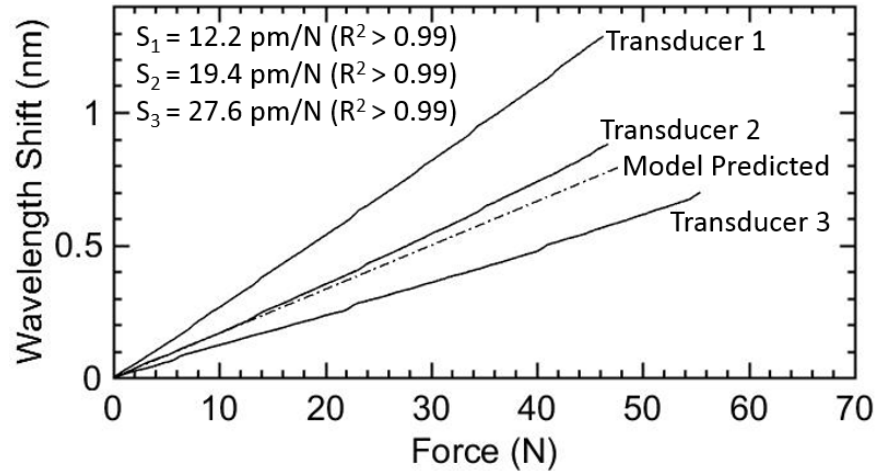
Figure 12: Sample calibration characteristics from three FBG transducers, showing their sensitivities and coefficients of determination from a linear regression analysis. The strain optic model prediction of 16.6 pm/N sensitivity is shown in the plot as well. Individual data points are not visible at this scale because all data captured at 62.5 kHz is presented and the distance between points at this rate is not discernable with the unaided eye. Permissions for reproduction of this figure were granted by IEEE.
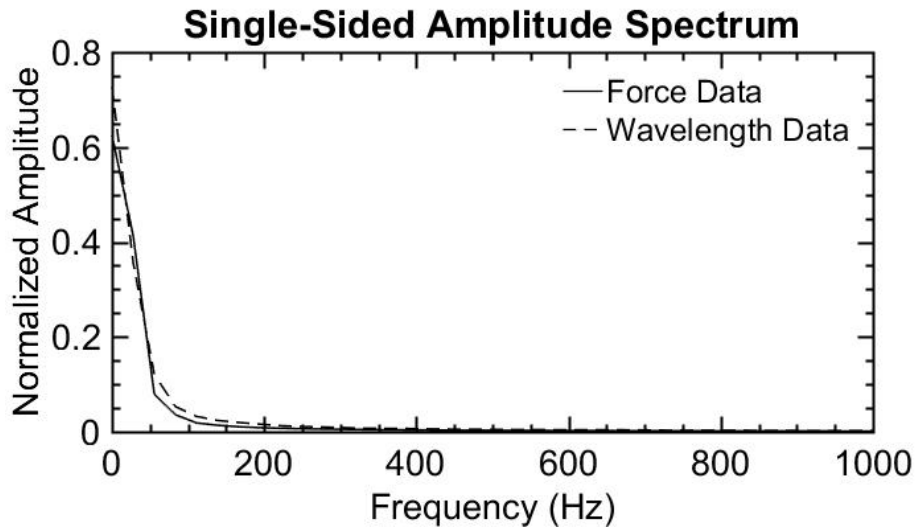
Figure 13: Frequency spectrum of accelerometer (force data) and FBG transducer (wavelength data) from an impact response calibration experiment. Permissions for reproduction of this figure were granted by IEEE.

Table 1: Sensitivity, predicted Standard Deviation in sensitivity, and COV (standard deviation divided by sensitivity) for three sets of FBG transducer dynamic calibration experiments (n = 3 for each). Permissions for reproduction of this table were granted by IEEE.

Tx #	Drop #	Sx [pm/N]	S.E. [pm/N]	COV [pm/N]	F.S.U. [N]	R^2 [ ]
1	1	12.206	0.024	0.20%	0.020	>0.99
1	2	12.153	0.023	0.19%	0.019	>0.99
1	3	12.109	0.021	0.17%	0.017	>0.99
	Mean:	12.156	0.023	0.19%	0.019	>0.99
2	1	18.807	0.036	0.19%	0.019	>0.99
2	2	19.014	0.038	0.20%	0.020	>0.99
2	3	20.483	0.026	0.13%	0.013	>0.99
	Mean:	19.434	0.033	0.17%	0.017	>0.99
3	1	27.019	0.040	0.15%	0.015	>0.99
3	2	28.012	0.025	0.09%	0.009	>0.99
3	3	27.852	0.026	0.09%	0.009	>0.99
	Mean:	27.627	0.030	0.11%	0.011	>0.99

Tx = transducer, Sx = sensitivity, S.E. (Sx) = standard error of sensitivity, COV = coefficient of variation of sensitivity, F.S.U. = full scale uncertainty.

Table 2: Comparison of normalized accelerometer and FBG transducer fourier amplitudes from the dynamic calibrations of three transducers (n = 3 for each). Permissions for reproduction of this table were granted by IEEE.

Tx #	Drop #	FFT Average [a] [ ]	RMS Difference [b] [ ]	Max Deviation [c] [ ]	RMS/Average [ ]
1	1	3.80E-03	1.11E-06	2.31E-02	0.03%
1	2	3.80E-03	1.90E-06	2.56E-02	0.05%
1	3	3.82E-03	3.78E-06	4.48E-02	0.10%
2	1	3.78E-03	3.29E-06	3.80E-02	0.09%
2	2	3.80E-03	2.04E-06	2.59E-02	0.05%
2	3	3.89E-03	5.21E-06	3.77E-02	0.13%
3	1	3.85E-03	1.62E-06	2.74E-02	0.04%
3	2	3.87E-03	1.38E-06	2.08E-02	0.04%
3	3	3.84E-03	3.75E-06	2.83E-02	0.10%
	Mean:	3.83E-03	2.68E-06	3.02E-02	0.07%
	STD:	3.75E-05	1.39E-06	8.08E-03	0.04%

[a] FFT average is calculated as the average normalized magnitude in the frequency domain for the reference transducer.
[b] RMS difference is determined based on the differences between the FBG transducer and the reference transducer magnitudes in the frequency domain.
[c] Max deviation is calculated as the maximum difference between the FBG transducer and the reference transducer magnitudes in the frequency domain.
STD = sample standard deviation.

3.4.3 Blast Simulation Results

Figure 14 shows pressure transducer output and FBG force transducer output from a sample ABS trial, normalized with respect to the maximum value observed from each sensor. Spectral results from these normalized outputs are shown in Figure 15. The peak results, mean, standard deviation, and coefficient of variation from 11 ABS experiments are tabulated in Table 3. From the spectral results in Figure 15, the average of reference transducer normalized output, RMS difference, max deviation, and the RMS/average ratio, are tabulated in Table 4.
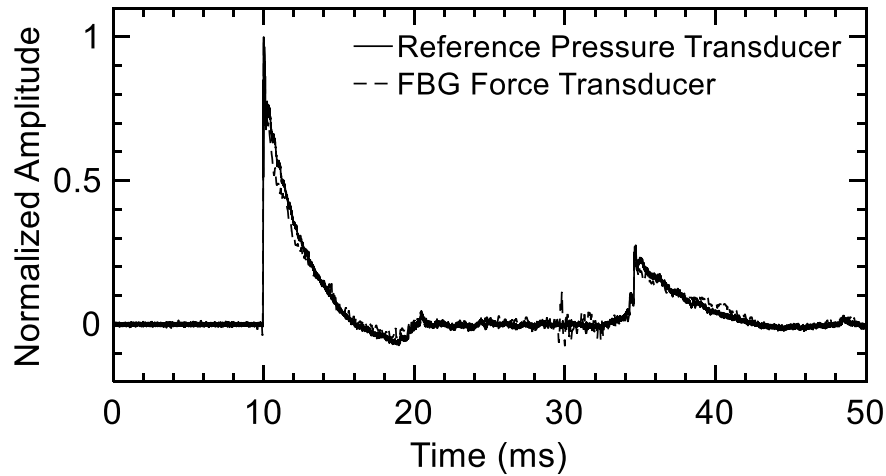
Figure 14: Normalized amplitude vs. time from a sample ABS experiment for both the reference pressure transducer and an FBG force transducer. Permissions for reproduction of this figure were granted by IEEE.
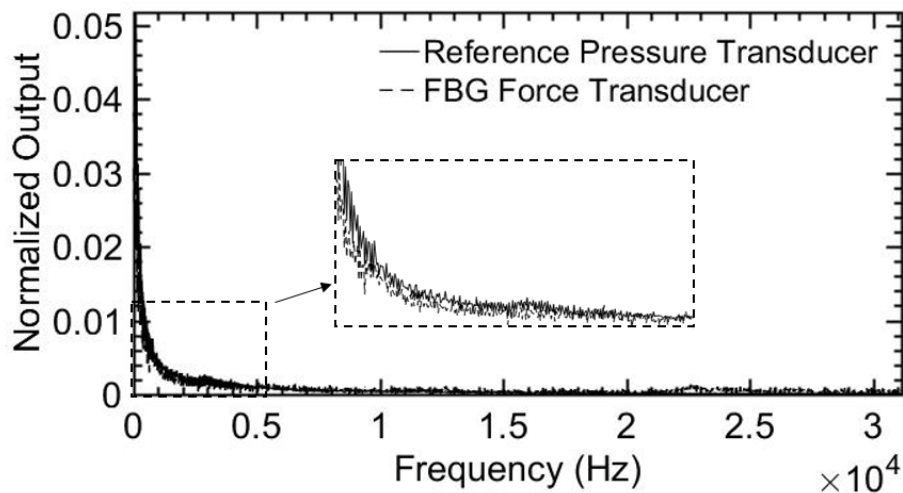
Figure 15: Spectral results from an ABS experiment, comparing the normalized output from the reference pressure transducer and an FBG force transducer. Permissions for reproduction of this figure were granted by IEEE.

3.4.4 Free-Field Blast Experiment Results

Frontal FBG force and ICP measurements and spectral results from the free-field blast experiment are shown in Figure 16.
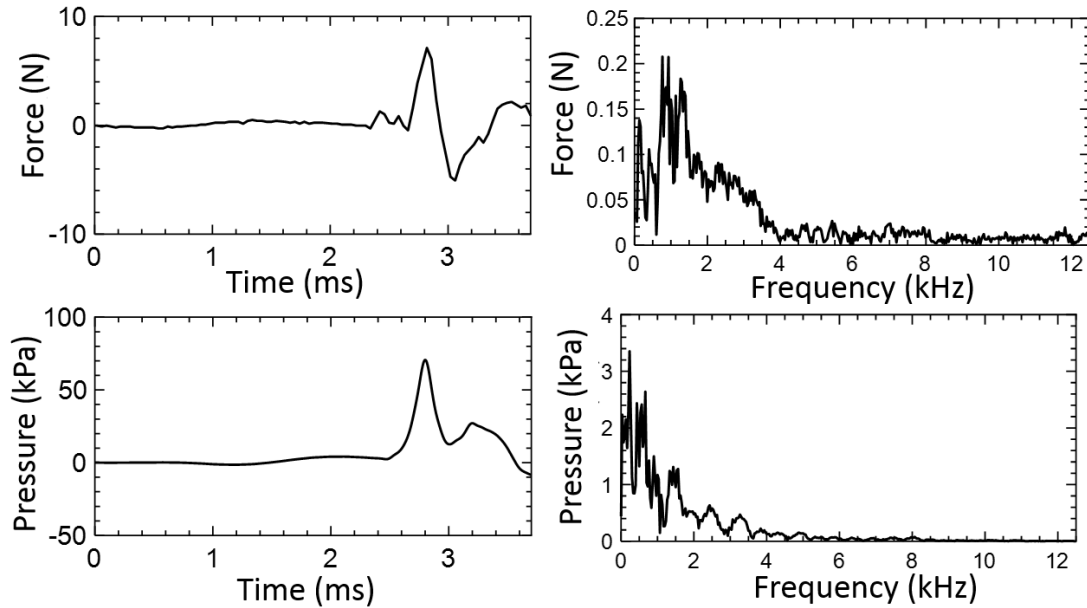
Figure 16: FBG force and ICP measurements, along with FFT transforms, from a free-field blast experiment using 5kg C4 at a 5m standoff. The presented data is for an un-helmeted (un-protected) BIPED. Permissions for reproduction of this figure were granted by IEEE.

Table 3: Driver overpressures and corresponding sensor peak measurements during ABS experiments. Permissions for reproduction of this table were granted by IEEE.

Target Pressure Level	Driver Overpressure [kPa]	FBG Transducer #1 Normalized Peak Output [a] [pm/pm]	FBG Transducer #2 Normalized Peak Output [a] [pm/pm]	Reference Pressure Transducer Normalized Peak Output [a] [kPa/kPa]
Low (n = 3)	283.23	0.395	0.367	0.447
	270.57	0.416	0.331	0.429
	208.13	0.362	0.314	0.360
Mean:	253.98	0.391	0.337	0.412
STD:	32.83	0.022	0.022	0.037
COV:	12.9%	5.7%	6.7%	9.1%
Medium (n = 3)	531.55	0.661	0.493	0.682
	526.67	0.570	0.581	0.666
	527.84	0.652	0.511	0.642
Mean:	528.69	0.627	0.528	0.663
STD:	2.08	0.041	0.038	0.016
COV:	0.4%	6.5%	7.2%	2.5%
High (n = 5)	1045.14	1.000	0.812	1.000
	1056.06	0.934	0.885	0.896
	1059.14	0.840	1.000	0.897
	1059.83	0.846	0.958	1.000
	1051.15	0.814	0.995	0.994
Mean:	1054.26	0.887	0.930	0.957
STD:	5.49	0.070	0.072	0.050
COV:	0.5%	7.9%	7.7%	5.2%

[a] Peak measurements were normalized based on the greatest observed value from that transducer in all 11 trials.
STD = sample standard deviation, COV = coefficient of variation.

Table 4: Spectral comparison of normalized reference pressure transducer and normalized FBG force transducer amplitudes. Permissions for reproduction of this table were granted by IEEE.

Target Pressure Level	Trial #	FFT Average [a] [ ]	RMS Difference [b] [ ]	Max Deviation [c] [ ]	RMS/Average [ ]
Low (n = 3)	1	1.34E-04	7.97E-08	1.47E-02	0.06%
	2	1.36E-04	9.64E-08	1.50E-02	0.07%
	3	1.42E-04	9.71E-08	1.34E-02	0.07%
Medium (n = 3)	4	1.15E-04	8.15E-08	1.65E-02	0.07%
	5	1.17E-04	8.57E-08	1.72E-02	0.07%
	6	1.19E-04	1.08E-07	1.98E-02	0.09%
High (n = 5)	7	1.11E-04	1.35E-07	2.00E-02	0.12%
	8	1.19E-04	1.19E-07	2.21E-02	0.10%
	9	1.10E-04	2.56E-07	2.66E-02	0.23%
	10	1.06E-04	2.18E-07	3.10E-02	0.21%
	11	1.05E-04	2.14E-07	3.04E-02	0.20%
	Mean :	1.19E-04	1.36E-07	2.06E-02	0.12%
	STD:	1.25E-05	6.33E-08	6.24E-03	0.06%

[a] FFT average is calculated as the average normalized magnitude in the frequency domain for the reference transducer.
[b] RMS difference is determined based on the differences between the FBG transducer and the reference transducer magnitudes in the frequency domain.
[c] Max deviation is calculated as the maximum difference between the FBG transducer and the reference transducer magnitudes in the frequency domain. Although the values for max deviation seem relatively large, they represent the maximum deviation at a single frequency, whereas the overall weighted difference is better represented by the RMS/average ratio.
STD = sample standard deviation.

3.5 Discussion

This work focuses on the development of Bragg grating techniques to measure skull to brain interaction forces in a surrogate head model designed to study head protection in blast. The presented transducer provides repeatable peak measurements and also captures all important transients associated with blast overpressure as indicated by our repeated experiments yielding data in both the time and frequency domain. To our understanding, this is the only FBG-based force transducer designed for the study of blast-induced kinetics in the brain.

Overall, the numerical and experimental results convey that the transducer has appropriate sensitivity and resonances for blast research. This is demonstrated by successfully capturing necessary characteristics in both time and frequency domains, under blast and impact loading conditions, while not inducing transducer resonance.

Finite element simulations predicted a first mechanical resonance of 24.8 kHz for the FBG force transducer, which is well above the impact-induced frequencies observed during dynamic calibrations, as well as for blast-induced loading observed during ABS experiments. Furthermore, we speculate that when the transducer is integrated into the BIPED interior, that the frequencies of excitation on the transducer will be lesser than those associated with our ABS experiments because the BIPED exterior skin and skull will provide considerable mechanical damping. Therefore, we are confident that the resonances of the presented transducer are appropriate for our ongoing research with the BIPED. Further, these results suggest that when the transducer is applied in the BIPED, that blast energy will not induce resonant vibration in the transducer structure and therefore measurement artefacts associated with mechanical vibrations are not predicted when the transducer is in-situ.

Under impact loading conditions during the dynamic calibration experiments, the FBG force transducer exhibits linearity ($R^2 > 0.99$ in all trials) and repeatability (mean coefficient of variation is less than 1% in all trials). Mean sensitivity from the three transducers is 19.7 pm/N, which is within 16% of the model predicted sensitivity of 16.6 pm/N. Variation in transducer sensitivity is due to the assembly process; specifically when the FBG is fixed along the aluminum bridge. Any deviation of the Bragg gratings from the nominal center position yields a drastic effect on sensitivity. Determining an appropriate sensitivity of the FBG transducer for the proposed application requires knowledge of what forces might be observed at the skull-brain interface during blast loading, however, literature does not suggest what these forces might be. Based on previously reported intracranial pressures during free-field blast experiments on the BIPED [27] and using the exposed surface area of the FBG transducer, we estimate that peak forces during similar blast trials would be on the order of 5-10 N. By designing the transducer to have a nominal sensitivity between 10-20 pm/N, combined with the fact that using higher acquisition rates on the SmartScan wavelength interrogator reduces the wavelength interrogation range to 1000 pm, allows the FBG transducer to capture forces up to 50-100 N. This is tenfold greater than the estimated upper limit, nevertheless we wanted to ensure a larger force range for this transducer since skull-brain interaction forces under blast loading have never been reported on before. Our pilot measures of skull-brain force (Figure 16), suggest that our estimates on the required force measurement range are appropriate.

For the nine calibration experiments performed on three force transducers, Fourier analysis suggests that the Bragg transducer is capturing all frequencies of interest in impact loading, which, for this dynamic calibration procedure, appear to lie below approximately 200 Hz. RMS differences between normalized force and wavelength magnitudes in the frequency domain were small relative to the average normalized value (ratios of RMS/Average were all less than 0.13%), indicating that the FBG transducers consistently capture similar spectral profiles when compared to the applied force signals.

Blast simulations in the ABS indicate that the FBG force transducer and reference pressure transducer both capture similar loading in the time-domain (Figure 14) and frequency domain (Figure 15). Because of the lesser sampling rate for the FBG transducer (62.5 kHz) when compared to the reference pressure transducer (500 kHz), it is possible that the time-series data for the FBG transducer could omit to capture the true peak captured by the reference transducer. To investigate this, we downsampled reference transducer data to 62.5 kHz and found that the peak amplitudes were reduced by approximately 7-10% relative to data collected at 500 kHz. We remind the reader that in this manuscript, we present normalized data for sensor calibration experiments in the shock tube and therefore the stated 7-10% reductions should not affect the trends noted in data tables, due to our normalization approach. Peak measurements are repeatable between trials (5.7-7.9% COV for FBG Transducer #1, 6.7-7.7% COV for FBG Transducer #2) and are comparable to the variation observed by the reference pressure transducer (2.5-9.1% COV). Figure 14 indicates that the force transducer can also capture the short-duration negative gauge pressure immediately following the positive phase, which is a characteristic of blast overpressure waves [40], viewed as the negative force section following the positive shock.

From the 11 ABS experiments, Fourier analysis suggests that the majority of the blast spectral content lies below approximately 5000 Hz, with similar Fourier amplitude shapes between FBG force and reference pressure. RMS differences between normalized FBG force and reference pressure in the frequency domain were small relative to the average normalized value (all ratios of RMS/Average were less than 0.23%), indicating consistency between the FBG transducer and reference pressure transducer. An important factor to note from these spectral results is that the FBG force transducers do not appear to resonate when subjected to

blast loading, which is indicated by an approximately zero amplitude observed at frequencies above 5 kHz. As mentioned previously, exciting this resonance would lead to mechanical vibration and force measurement artefacts in the output signal. This also suggests that our data acquisition rate (62.5 kHz) is sufficient to acquire transient signals in the presented application. However, we acknowledge that other demodulation approaches based on edge filters and photodetectors [41] could be employed to achieve greater acquisition rates.

Other sensing technologies, such as resistive or capacitive based force transducers, could be used for this application but arguably they could be considered to have drawbacks. First, transducers based on resistance and capacitance can require several conductors for excitation and signal retrieval, per sensor. The number of excitation and signal conductors increases in direct proportion to the number of transducers used. Second, because they are electronic these transducer technologies are not typically capable of operating when submerged in fluid, and if they are submerged in fluid, they typically require the transducer element to be sealed (i.e. shielded from the fluid). Optical fibre-based transducers, like that presented in this manuscript, require only one optical conductor for each measurement location and are intrinsically immune to the effects of fluid (including the fluid layer in the BIPED). Therefore, because they require relatively lesser conductors and are not sealed from fluid, optical transducers can typically be constructed to be relatively smaller and arguably less complicated than electronic alternatives. Small size and design simplicity offset a primary drawback of using optical transducers: the requirement for relatively more expensive instruments that supply and detect light. Specific to application in the BIPED, because the integration of the force transducer into the BIPED skull requires material removal from the skull, such that the embedded instrumentation appears flush with the inner surface, it is desirable for the instrumentation (both the transducer itself and the transmission medium – either wire or optical fibre) to be as small as possible such that the amount of material removed from the skull is minimized. By minimizing the material removed, we also minimize the corresponding change to overall skull stiffness, a parameter which we desire to remain unaltered such that the BIPED continues to offer a mechanical response similar to previous validation experiments [18]. Therefore, we argue that the use of optical fibre based transducers (i.e. Bragg gratings in this case) is justified when one considers the above factors and the requirements of in situ measurements in the BIPED.

Temperature compensation is not implemented for this work due to the short timescales over which blast wave loading occurs. Despite high temperature exposure during a free-field detonation experiment, the blast wave interacts with the transducer too rapidly to induce a significant temperature shift in the FBG transducer.

Data in Figure 16 from a free-field blast experiment shows that the FBG force transducer is capable of capturing similar time domain traces to the ICP transducer, in both time and frequency domains. Of note, the FBG force measures exhibit negative magnitude (Figure 16) when ICP measures reach a local maximum. In ongoing work, we will scrutinize our data in an attempt to understand these mechanics. In the present paper, we present the exemplar data (Figure 16) to convey that the FBG transducer is capable of detecting kinetics in-situ during a blast event. Higher frequency components observed more predominantly in the force transducer signals could be due to localized skull flexure. The ICP time-series trend and peak magnitude are similar to previously reported BIPED free-field blast experiment results [27]. Peak force magnitude of 7 N from this blast experiment is within the force range that we anticipated.

In forthcoming work, the presented transducer will be used to measure skull to brain interaction forces in multiple locations during free-field blast experiments that expose the BIPED to realistic overpressures. These blast experiments will be repeated for scenarios both with and without protective headgear. While the exact threshold forces for skull-brain interaction and injury are not universally agreed upon, the presented transducers can be used to measure force mitigation, if any, offered by contemporary military protective headgear. These force measurements, in parallel with pressure measurements in the brain parenchyma, will allow us to determine the open question on whether or not protective headgear mitigates blast energy transfer into helmeted soldiers. It is also possible that the FBG transducer presented could be applied in other surrogate models used in impact and blast research. Such application would necessitate minor transducer re-design to ensure the transducer can capture kinetics over ranges appropriate for the application.

In summary, this study presents the development of a FBG force transducer to measure skull-brain interaction forces within a mechanical surrogate headform used to assess protective headgear during blast loading. The presented transducer exhibits repeatability in both impact

force and blast overpressure loading and exhibits excellent agreement with calibration reference transducers in both the time and frequency domain. The transducer can be arrayed within the surrogate headform and used to assess the forces that are created as a result of blast overpressures interacting with both unprotected and protected (i.e. helmeted) heads.

3.6   Conclusions

This paper detailed the development of an FBG force transducer for measuring blast kinetics and the capacity for these transducers to be integrated into the surrogate skull of the BIPED. The main contribution from this paper is providing a validated and repeatable transducer for blast and impact scenarios that can measure inner skull forces within a surrogate headform. The novel force transducer is the first application of FBG technology towards measuring inner skull kinetics under blast loading. While brain pressure and inner skull forces are not directly linked towards TBI, these metrics provide insight towards how the brain and skull react under blast loading and may present an appropriate paradigm towards assessing the relative efficacy of protective headgear at mitigating internal kinetics. The next objective of this thesis, which is the topic for the following chapter, is to investigate the transmissions of blast and impact energy into the BIPED for various protection scenarios.

Chapter 4: Protective headgear attenuates forces on the inner table and pressure in the brain parenchyma during blast and impact: an experimental study using a simulant-based surrogate model of the human head.

The following manuscript is under preparation for submission into the ASME Journal of Biomechanical Engineering (to be submitted in January 2019). This paper does not identically match the version to be submitted to ASME Journal of Biomechanical Engineering. The first author of this manuscript is also the author of this thesis.

4.1 Introduction

In order to document the effect that head protection has on skull and brain kinetics, the BIPED was instrumented with an array of transducers and subject to blast and impact experiments. This chapter describes the effect of contemporary protective headgear on mechanical measures within the cranial vault of a simulant-based surrogate headform during both blast and impact events. Specifically, pressures within the brain parenchyma and forces on the inner table of the skull are investigated.

4.2 Background

Rates of traumatic brain injury (TBI) among warfighters have been rising during recent conflicts and have had a profound impact on the health of combat veterans [3,131–135]. For soldiers deployed to Afghanistan (Operation Enduring Freedom; OEF) and Iraq (Operation Iraqi Freedom; OIF), it has been estimated that nearly 25% of all deployed warfighters suffered from symptoms of TBI [136–138]. Blast exposure accounts for the majority of total injuries among contemporary military personnel, with reports as high as 80% [14,139–141]. It is estimated that 50-60 % of head injuries involving blast exposure on the battlefield also involved blunt trauma [85]. During the OEF and OIF conflicts, the use of explosive devices increased, with improvised explosive devices (IEDs) becoming the weapon of choice against coalition forces [142], resulting in increased blast exposure for the modern warfighter [143,144]. The US Navy-Marine Corps combat trauma registry reported that IEDs were found to be the most common mechanism responsible for TBI cases (52%) during OIF [145].

Effective mitigation strategies are strongly desired by Canadian and US militaries, but in order to reduce the occurrence of blast-induced traumatic brain injury (bTBI), a proper understanding of the bTBI injury mechanisms is required [14].

An explosive blast can cause many different types of injury, which are broadly classified into four categories [14,146]. Primary blast injury is due to the direct effects from the blast wave propagating through the body and damaging living tissue. Secondary blast injury involves the propulsion of debris or fragments that can cause blunt or penetrating injury. Tertiary blast injury occurs when the explosion induces global acceleration of the body, propelling it into collision with surrounding structures in the environment. Quaternary blast injuries are due to post-detonation environmental stressors, such as chemical exposure or burns from thermal radiation. There is limited information available on the effect of primary blast on the human head [14,141], and it is not yet clear how significant primary blasts are relative to blunt impact as sources of injury [85]. Due to the sensitivity of brain tissue to loading rate [147], the mechanisms of injury for primary blast TBI (bTBI) may not be similar to conventional blunt TBI [141,148,149]. In this work, we focus on studying primary blast exposure using free-field detonation experiments and compare results with low-speed impact trials that can simulate a tertiary blast injury scenario involving direct head impact [150].

The mechanisms of primary bTBI remain poorly understood, however several theories exist [14,151]. One theory suggests that blast waves can damage brain tissue by travelling through skull orifices such as nasal sinuses [49], auditory canals [50,51], and/or eye orbits [52–55]. It has also been suggested that a blast wave could directly transmit into the brain through the skull via transosteal wave propagation, referred to as the direct cranial transmission theory [46–48], however acoustic impedances suggest that this is an unlikely mechanism [14]. Another theory suggests that skull deformation can be induced from a blast wave [56–58], either through localized deformation or by exciting a mode of skull resonance. These skull deformations can then cause significant intracranial pressure (ICP) fluctuations [14,59]. Another theory referred to as thoracic surge is proposed to cause bTBI indirectly through the rapid compression of the thorax and abdomen from the blast wave, which then transmits a pressure wave towards the brain through soft tissue and vascular mediums [68–70]. Cavitation has also been proposed as a primary blast injury mechanism, in which localized regions of

negative ICP may result in the formation of cavitation bubbles that cause damage to surrounding brain tissue when they collapse [65,75]. These theories on primary bTBI remain under dispute, but likely do not occur in isolation from one another during a realistic blast scenario, and may vary based on the loading magnitude and exposure duration [14,151]. Understanding which mechanisms are most prevalent during a blast scenario and how they can effectively be mitigated could help direct the development of future protective combat headgear.

The mechanisms of impact induced head injury are relatively better documented than are the mechanisms of blast injury [121]. Impact forces on the head create abrupt head motions comprising both linear and rotational mechanics. These impact forces are first applied to the scalp and then skull, which can in turn create relative motion between the skull and the brain within the cranial vault. These relative motions are believed to be a possible cause of disruption to bridging veins (usually implicated in subdural hematoma) [152,153] and also of contact between the brain and skull leading to disruption of brain tissue (proposed as a mechanism for coup and contre-coup injuries) [154]. Impact to the head and brain also elicit accelerations that are both linear and rotational which are thought to result in inertial loading of tissue leading to both local (focal) and widespread (diffuse) tissue damage [155]. Impact induced injuries are generally classified as either focal or diffuse. Examples of focal injuries include contusion, laceration and localized skull fracture, the latter of which is typically considered to be caused by localized forces on the skull and has in a large amount of literature been correlated with linear head acceleration following impact [156–158]. Examples of diffuse injuries include widespread subdural hematoma due to bridging vein rupture and diffuse axon disruption, the severity and risk of each have both been correlated with rotational impact mechanics including acceleration and velocity [155,159–161]. Often, after a head impact, both linear and rotational kinematics result and therefore it is possible to have both head and brain injuries that are focal and diffuse, affecting both the skull and brain.

Helmets are the primary protection device fielded to protect the head of the wearer from impact, as well as ballistic threats for military personnel, and they are commonly acknowledged as being effective in protecting the wearer from these threats [15,17,84–89]. In combat scenarios, no existing protective headgear is able to fully protect against all the

potential threats that can exist on the battlefield [85]. Current combat helmets are tested by their ability to prevent ballistic penetration, mitigate blunt trauma, and behind-helmet blunt trauma (BHBT) from projectiles and by their ability to withstand environmental stressors such as exposure to temperature extremes [85]. Ballistic protection of the head is achieved by the helmet exterior shell that is struck by projectiles, and through a process involving permanent deformation and failure of shell materials, the exterior shell redistributes the loading over a larger area and reduces the amount of energy available for transmission to the helmeted head. These reductions in energy transfer are typically inferred from head models that use clay to measure depth of deformation of the helmet interior [162], and more recent proposals use head models capable of measuring forces exerted on the head exterior during helmet deformation. Reduction in energy transmission to the underlying head is generally associated with reduced risk and severity of head injury. Similarly, for impact protection, helmets are tested for their ability to attenuate impact energy transmission to an underlying head [85], typically quantified by measuring linear head acceleration during the impact event. A helmet that leads to lesser head acceleration than that measured with another helmet is typically thought to offer superior impact attenuation, and head protection [163]. It is evident from the above that the paradigm for assessing head protection is quantifying reductions in energy transfer. Despite the efficacy of contemporary combat helmets in mitigating injury from ballistic threats and impacts, bTBI rates continue to rise [164], and it appears to be an open question whether modern combat helmets are effective at protecting military personnel from blast waves. Indeed, there is scant biomechanical literature that assesses whether or not contemporary military head protection is capable of altering the transmission of blast energy into the head and brain.

The objective of this study is to ascertain whether or not protective headgear alters the transmission of blast and impact energy into the brain, using a biofidelic surrogate of the head based on simulant materials. Free field blast simulations at an outdoor test range were conducted to create realistic blast loading on the head surrogate for cases where the head was unprotected, wearing a contemporary military helmet, and wearing both a helmet and eye protection. Impact loading on the head surrogate was also created in a laboratory setting for the cases where the head surrogate was unprotected and protected using a helmet. Within the surrogate head, forces on the inner table of the skull were measured, along with pressures

within the brain parenchyma. Transmission of energy into the brain was quantified through peak measures in force and pressure as well as quantification of frequency components in the force and pressure data. Descriptive statistics of repeated experiments were quantified for the purposes of comparing measured mechanics between cases of unprotected and protected headform scenarios.

4.3 Methods

4.3.1 Surrogate Headform and Instrumentation

For this work, we instrument a surrogate blast headform known as the Blast Injury Protection Evaluation Device (BIPED), fully developed by Defense Research and Development Canada (DRDC). An in-depth report on the BIPED, including the history of development, along with current headform geometry and physical properties, is presented in previous literature [81]. The BIPED has been subjected to simulated blast overpressure in blast tube experiments and has been shown to measure ICP of comparable peak magnitude, time duration, and frequency content to cadaver heads that were subjected to overpressure in the same blast tube [66]. In this paper, we outline key headform properties and provide details on the instrumentation used for this study.

The BIPED, shown Figure 17, has several internal and external biofidelic features such as anthropomorphic eye orbits, nasal cavities, a brain, cerebrospinal fluid, skin, a jaw, ears, a cerebellum cavity, along with falx and tentorium membranes. Surrogate skull material is nominally 6.35 mm thick and composed of TC-854 A/B polyurethane (BJB Enterprises Inc., CA United States). Surrogate brain tissue (exposed in Figure 17a) is composed of the silicone Sylgard 527 (Dow Corning Corporation, MI United States), and water is used to simulate cerebrospinal fluid. The external soft tissue layer (Figure 17a) is composed of a tough urethane rubber (Vytaflex 20, Smooth-On Inc., CA United States). Internal falx and tentorium membranes are modelled using 70A hardness Neoprene layers. External feature locations and size are based upon head models used in, for example, Canadian Standards Association CAN/CSA Z262.6-02, helmet test standards [82]. The upper skull geometry matches the top half of the ISO Size J Headform (Cadex Inc., QC, Canada), and internal skull features are based

upon an open-source CAD model of the human skull [83]. The BIPED has a 4-point attachment location at the base of skull where it can be mounted onto a Hybrid III neck.
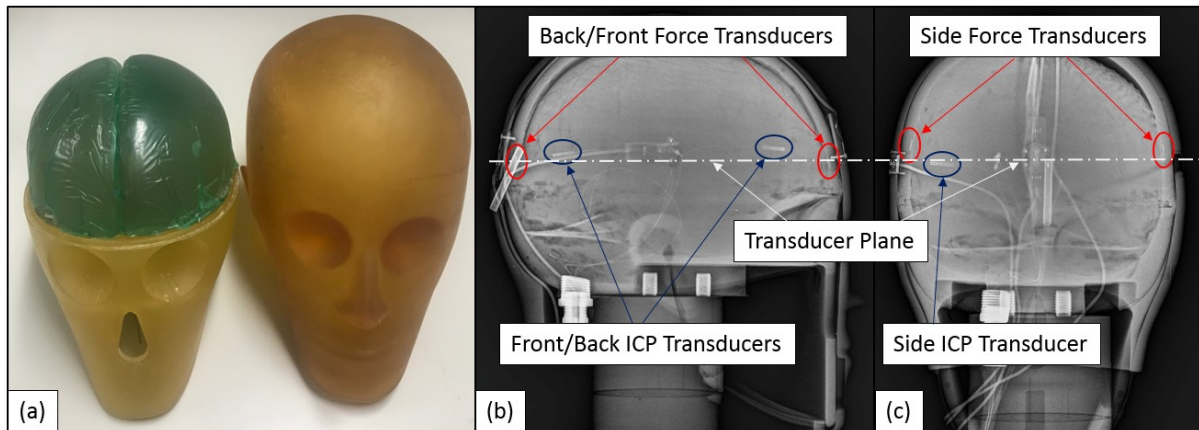
Figure 17: (a) BIPED with the upper skull cap removed and surrogate brain exposed on the left, with the surrogate scalp to the right. (b) Right to left side view X-ray image of the instrumented BIPED showing front and back ICP and force transducer locations. (c) Front to back view X-ray image of the instrumented BIPED showing side ICP and force transducer locations.

For the experiments performed in this study, a BIPED is instrumented with several pressure transducers, similar to work done previously [66,81], but it is additionally equipped with novel force transducers within the surrogate skull material. X-ray images showing some of these transducer locations can be seen in Figure 17. In our previous work, in-fibre Bragg grating (FBG)-based optical force transducers were developed for measuring forces with frequency content characteristic of blast [165], and for this study, multiple FBG-based force transducers are calibrated and integrated into the surrogate skull material and mounted flush with the inner surface (inner table) of the skull. These transducers are composed of an FBG embedded within an aluminum and acrylic based multi-layered cylindrical superstructure, with an overall size of 3 mm in height and 6.3 mm in diameter. The approximate transducer plane for which these transducers are integrated is shown in Figure 18a. This transducer plane is parallel to the transverse plane and offset by approximately 20 mm above the eye sockets on the surrogate skull. Individual transducer locations are shown in Figure 18b, with four locations for front, right, left (impact only), and rear transducers. Two surrogate skull caps are instrumented with an array of force transducers (one for blast experiments and one for impact experiments). After performing the blast experiments, the BIPED skull cap was replaced with

another instrumented skull cap for impact experiments with an additional force transducer on the left side. The transducers are fixed into the headform using high strength epoxy (Loctite MS 930, Henkel AG & Co., Germany).
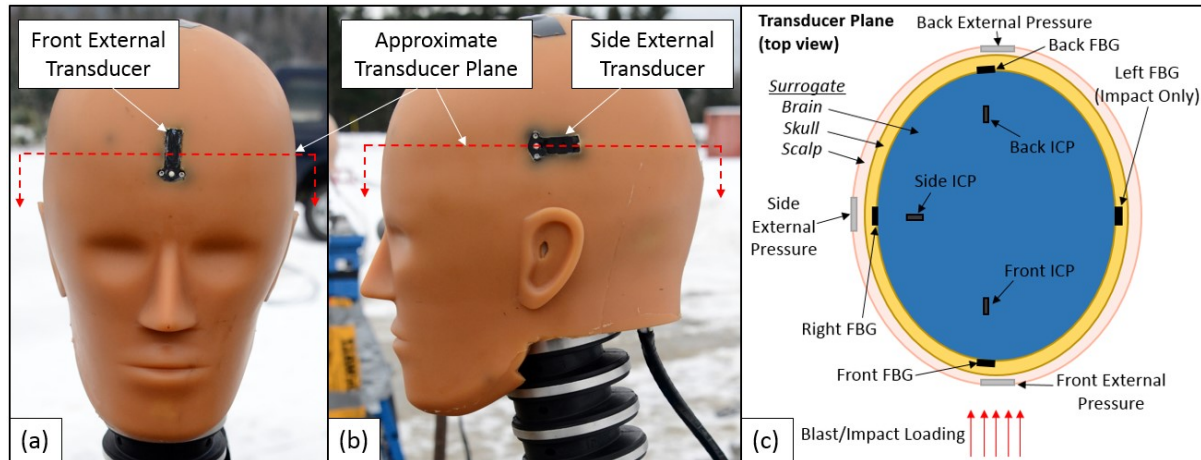
Figure 18: (a) BIPED front view showing the transducer plane and front external transducer. (b) BIPED side view showing the transducer plane and side external transducer. (c) Top view of the transducer plane showing the instrumentation locations.

In addition to the force transducers, the BIPED used for this study is instrumented with several pressure transducers for measuring internal pressures within the surrogate brain parenchyma, as well as the external pressure profile. Three Kulite piezo-resistive pressure transducers (modified XCL-072, Kulite Semiconductor Products, NJ United States) are used to monitor ICP. These transducers have a linear output for pressures up to 14 bars, a resonant frequency over 550 kHz, and are relatively insensitive to acceleration (less than 0.0001% full scale output per g). These ICP transducers are molded into the surrogate brain material (locations shown in Figure 18) in approximately the same plane as the force transducers. External pressure measurements are collected by pressure transducers (modified LL-125 flat line series, Kulite Semiconductor Products, NJ United States) located on the front, side, and back locations of the headform (shown in Figure 18). These external pressure transducers were retrofit into the surrogate skin material and mounted to be flush with the outer surface of the BIPED. The BIPED is filled with water to model CSF and then sealed using thread sealing cord (Loctite 55-10, Henkel AG & Co., Germany) and self-fusing silicone (Loctite SI 5075,

Henkel AG & Co., Germany) for blast experiments. For impact experiments, the BIPED was sealed using an industrial silane adhesive (Loctite MS 930, Henkel AG & Co., Germany).

4.3.2 Blast Exposure

The instrumented BIPED described in the previous section is exposed to blast overpressure at a free-field testing facility located in Valcartier, Quebec, Canada. For these experiments, a 5 kg cylindrical C4 charge is detonated at a height of 1.5 m above the ground. The BIPED is positioned 5 m away horizontally, with the nose of the headform positioned at approximately the same height as the charge. Unprotected and protected side views of the BIPED can be seen in Figure 19. For helmeted cases in this study, we use a Tactical Ballistic Helmet (TBH-II HST Size Large, Gentex Corporation, PA United States). This helmet meets the modified and abbreviated NIJ Standard 0106.01 [166] for ballistic helmets using the NIJ Standard 0108.01 threat level IIIA [167] (9mm 124gr FMJ RN at 1400 fps). It also meets the modified and abbreviated US Army ACH Helmet CO/PD-05-04: 2007 specification.
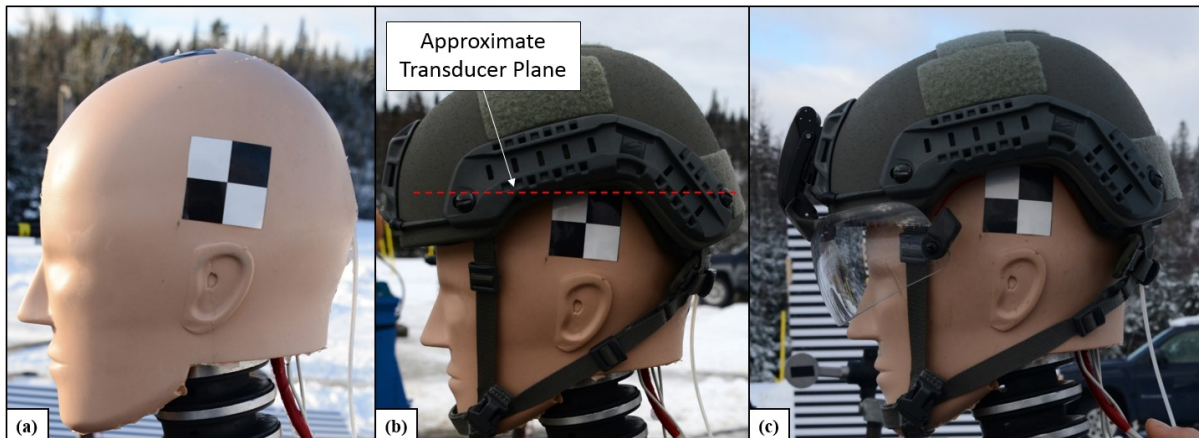
Figure 19: (a) Unprotected BIPED. (b) Protected BIPED with TBH, showing the approximate plane in which the transducers are located relative to the helmet rim. (c) Protected BIPED with TBH and visor.

For blast experiments, the BIPED is fixed upon a Hybrid III neck (Humanetics Innovative Solutions, MI, USA), in which the base of the neck is fixed upon a rigid vertical steel pole that is held secure to a concrete pad at the ground. The steel pole also helps to protect wires and optical fibres running external to the headform. ICP and external pressure signals were collected at 1 MHz and force signals on the inner table of the simulant skull were gathered

at 40 kHz, using a commercial interrogator (SmartScan, Smart Fibres Ltd., UK). A schematic of the test platform can be seen in Figure 20, in which the BIPED is facing the charge, and a visual of the fireball and BIPED immediately post-detonation is shown in Figure 21.
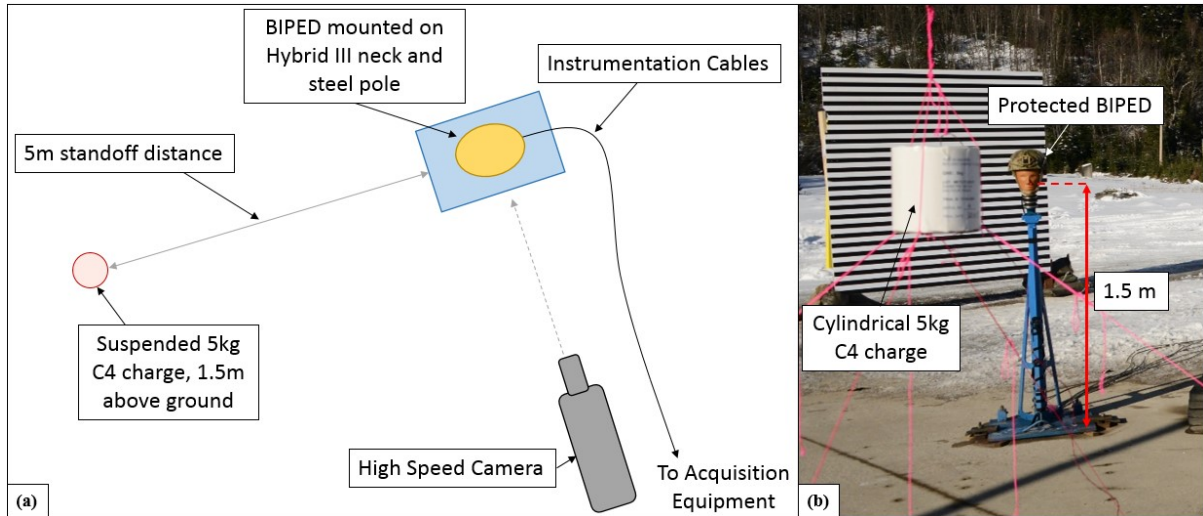
Figure 20: (a) Top-view schematic of the free-field blast experiment setup. (b) Free-field blast experiment setup showing the suspending charge and mounted BIPED with a TBH helmet.

Figure 21: Blast test site showing the resulting fireball from a 5kg C4 detonation and BIPED location during experiments.

Four blast experiments are repeated using an unprotected (bare) BIPED, and seven experiments are conducted using various headform protection scenarios, for a total of 11 blast experiments and 4 protection scenarios. The different test scenarios for the 11 blast experiments are outlined in Table 5. For the protected scenarios: three trials were performed using a TBH, two trials were performed using the TBH and a visor (Baltskin Cobra, Revision Military Ltd., VT USA), and two trials were performed using the TBH, visor, and a lower stiffness neck scenario. The lower stiffness neck scenario was achieved by replacing the standard Hybrid III rubber nodding blocks with a retrofit foam insert. Because the Hybrid III neck is known to have much greater stiffness than a human neck [168,169], this lower stiffness neck scenario was created in an attempt to exhibit increased global headform motion in response to a blast wave.

Table 5: Test conditions of the free-field blast experiments

Scenario #	Number of Repeats	Protection	Neck Stiffness
1	n = 4	None (Unprotected)	Normal (Regular Hybrid III neck)
2	n = 3	Gentex TBH	Normal (Regular Hybrid III neck)
3	n = 2	Gentex TBH + Visor	Normal (Regular Hybrid III neck)
4	n = 2	Gentex TBH + Visor	Low (Hybrid III neck with foam nodding blocks)
Total Blast Experiments:	n = 11		

4.3.3   Impact Loading

An instrumented BIPED (identical to the one used for blast experiments except lacking external pressure transducers, and has an additional force transducer on the left side) is subjected to impact experiments using a custom-built linear guided monorail drop tower [170,171]. All impacts are to the high forehead of the BIPED. High speed cameras (Phantom v611, Vision Research, Wayne, NJ) are used to track global headform movement at 1000 frames per second. A soft impact surface consisting of sportsfield turf (SouthWest Greens GB-011, 100% Polyethylene, 1.75 in pile height) with a crumb rubber infill was fixed upon a steel anvil at the base of the vertical drop tower. This soft impact surface was used instead of the bare steel anvil in order to protect the bare BIPED headform from potentially rupturing and leaking internal fluids at higher drop velocities. The BIPED is mounted onto a Hybrid III neck, which in turn is fixed to an adjustable gimbal that moves freely along the vertical axis of the drop tower. A still-image of a protected and unprotected BIPED drop tower setup can be seen in Figure 22.
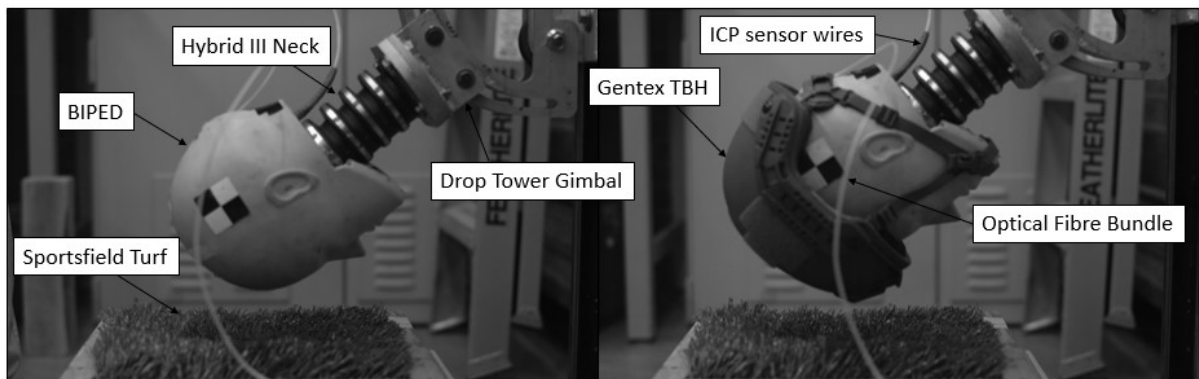
Figure 22: Unhelmeted (left) and helmeted (right) BIPED headform fixed to a Hybrid III neck and drop tower gimbal during an impact experiment.

The height in which the headform is dropped from is controlled to achieved three tiers of impact velocity, termed "low" (1.47-1.54 m/s), "medium" (2.31 – 2.37 m/s), and "high" (3.25 – 3.33 m/s). For each velocity tier, five drop experiments were repeated for an unprotected BIPED and a protected BIPED (using the same TBH model that was used for blast experiments), totaling 30 impact experiments. A test matrix for the BIPED impact experiments can be seen in Table 6. For these impact experiments, ICP data is collected at 25 kHz and force data is gathered at 20 kHz.

Table 6: Test matrix for laboratory impact experiments

Impact Velocity	Head Protection	Number of Repeats	Impact Surface
Low (1.47-1.54 m/s)	None	n = 5	Sportsfield Turf
	TBH	n = 5	Sportsfield Turf
Medium (2.31 - 2.37 m/s)	None	n = 5	Sportsfield Turf
	TBH	n = 5	Sportsfield Turf
High (3.25 - 3.33 m/s)	None	n = 5	Sportsfield Turf
	TBH	n = 5	Sportsfield Turf
	Total Impact Experiments:	n = 30	

4.3.4   Signal Conditioning and Time Synchronization

Data for this study is post-processed using MATLAB R2016b (MathWorks Inc., MA United States). For the instrumentation used during blast experiments, including external pressure, ICP, and force signals, the raw data is filtered using a 4th order Butterworth low pass filter with a cutoff frequency of 10 kHz, based on CFC 6000 [66,172]. Data from impact experiments is filtered using a 4th order Butterworth low pass filter with a cutoff frequency of 1650 Hz (CFC 1000). This filtering approach uses filter specifications described by the Society of Automotive Engineers (SAE) Standard J211 for processing head kinematics and head/neck forces in impact experiments [173]. We acknowledge that the SAE standard does not discuss filtering approaches for forces on the inner table or parenchyma pressures. Nevertheless, our impact measurements indicate frequency content well below CFC1000 cutoff frequency, therefore we feel this filtering approach is appropriate because it will not remove mechanical energy at key frequencies in our signals.

For blast experiments, pressure signals are all time synchronized and triggered by the signal sent to the detonator. Force signals are collected on a separate data acquisition system

triggered manually just before detonation. During impact experiments, ICP and force signals are also collected on separate data acquisition systems. For comparison of data from different blast trials, signals are aligned based on the incident peak of the front external pressure transducer. For comparison within trials, force signals are aligned by shifting the initial peak of the front force transducer to be approximately halfway between the front external incident peak and the front ICP initial peak. For example, in many blast trials the front external pressure incident peak occurs around 2.6 ms and the front incident ICP peak occurs at approximately 2.8 ms, therefore the force signals are shifted such that the front initial force peak occurs at 2.7 ms in this instance. We acknowledge that this may not be the exact time where the force signal peaks would occur, however for the visualization purposes in this work, the error from using this synchronization method should be no greater than 100 μsec and the true difference would not be distinguishable for the figures shown in this paper. In addition, our subsequent analysis focuses on magnitudes of measured mechanics as opposed to their relative order of sequence in the time domain, and so we believe our data analysis approaches are justified. Consequently, any conclusions drawn are limited to magnitudes of measured mechanics.

For spectral analysis, we use a fast Fourier transform (FFT, implemented using MATLAB R2016b) to investigate whether the various protection scenarios have an effect on frequency content [174] in measured data. We also examined the accumulation of amplitudes with increasing frequency using normalized cumulative FFT data, which contain the cumulative sum of FFT amplitudes normalized by the total value of all amplitudes accumulated up to the Nyquist frequency for the given blast or impact experiment. For blast experiments, the Nyquist frequencies are 250 kHz (pressure data) and 20 kHz (force data). For impact experiments, they are 12.5 kHz (pressure) and 10 kHz (force). These normalized data convey the proportion of amplitudes accumulated up to a given frequency in a measured parameter (e.g. pressure or force).

4.3.5   Statistics

For blast experiments, we report the mean results of peak measurements for each scenario. For impact experiments, we report mean, sample standard deviation (STD), and coefficient of variation (COV) of peak measurements for each scenario.

4.4   Results

4.4.1   Blast Exposure

Representative blast data for each transducer location from an unprotected and protected headform scenario can be seen in Figure 23. Peak results and means for each protection scenario are tabulated in Table 7 for the incident blast and ground reflected waves, as measured by the external pressure transducers. Pressure versus time and FFT data from the ICP transducer measurements are shown in Figure 24 for the four protection scenarios, with maximum and minimum values summarized in Table 8. Similarly, Force versus time and FFT data from the force transducer measurements are shown in Figure 25 for the four protection scenarios, with maximum and minimum values tabulated in Table 9. Finally, normalized cumulative FFT data, which contain the cumulative sum of FFT magnitudes normalized by the total value accumulated up to the Nyquist frequency, are shown in Figure 26.
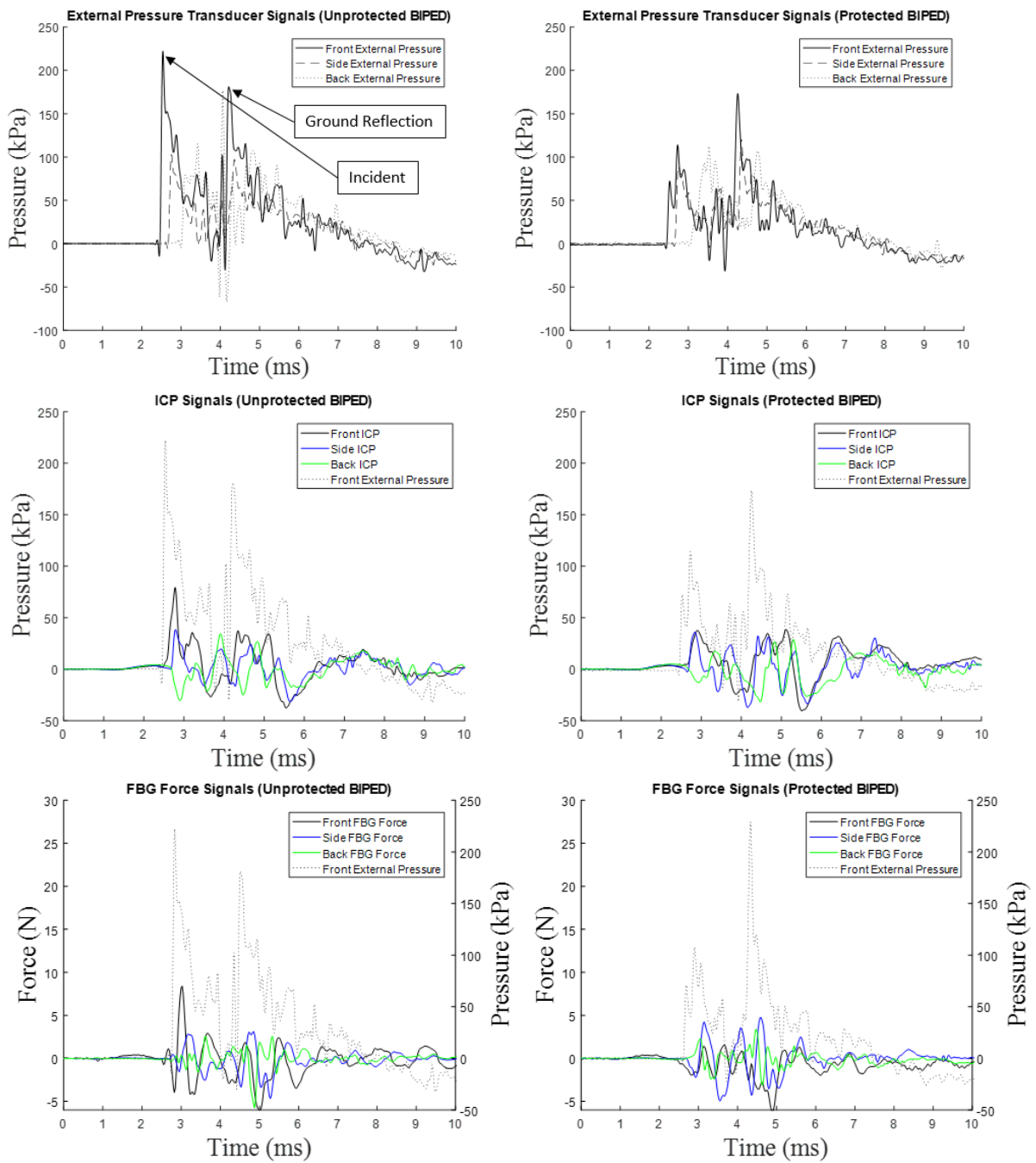
Figure 23: Representative blast data for all transducer locations in an unprotected scenario (Scenario #1, trial T4, shown at left) and a protected scenario (Scenario #3, trial T1, shown at right). The top row contains external pressure measurements for each transducer location. The middle row contains ICP measurements from each transducer location, along with the front external pressure measurement for reference. The bottom row contains force measurements from each transducer location, along with the front external pressure measurement for reference.

Table 7: Peak pressures measured with external transducers on BIPED, for incident blast and ground reflected waves. Means are tabulated for each of the different protection scenarios.

		Peak External Pressure Magnitudes					
		Incident Shock			Ground Reflected Shock		
		Front	Side	Back	Front	Side	Back
Scenario #	Trial #	(kPa)	(kPa)	(kPa)	(kPa)	(kPa)	(kPa)
1	T1	225.1	97.4	86.7	171.1	91.0	110.6
1	T2	220.8	101.9	89.3	152.2	102.4	94.9
1	T3	230.0	103.0	92.4	180.5	81.8	98.3
1	T4	222.2	102.8	176.6	181.2	97.2	90.3
	Mean:	**224.5**	**101.3**	**111.3**	**171.3**	**93.1**	**98.5**
2	T1	187.1	96.6	104.4	249.3	139.5	85.7
2	T2	170.7	91.0	111.9	232.6	125.8	98.0
2	T3	224.7	78.2	94.2	212.3	87.8	77.7
	Mean:	**194.2**	**88.6**	**103.5**	**231.4**	**117.7**	**87.1**
3	T1	114.1	89.3	112.4	173.3	120.2	107.2
3	T2	107.6	90.3	115.6	229.1	120.2	114.1
	Mean:	**110.9**	**89.8**	**114.0**	**201.2**	**120.2**	**110.7**
4	T1	116.6	90.4	129.3	172.5	109.9	113.3
4	T2	75.3	135.5	135.5	225.0	74.5	74.5
	Mean:	**96.0**	**113.0**	**132.4**	**198.8**	**92.2**	**93.9**
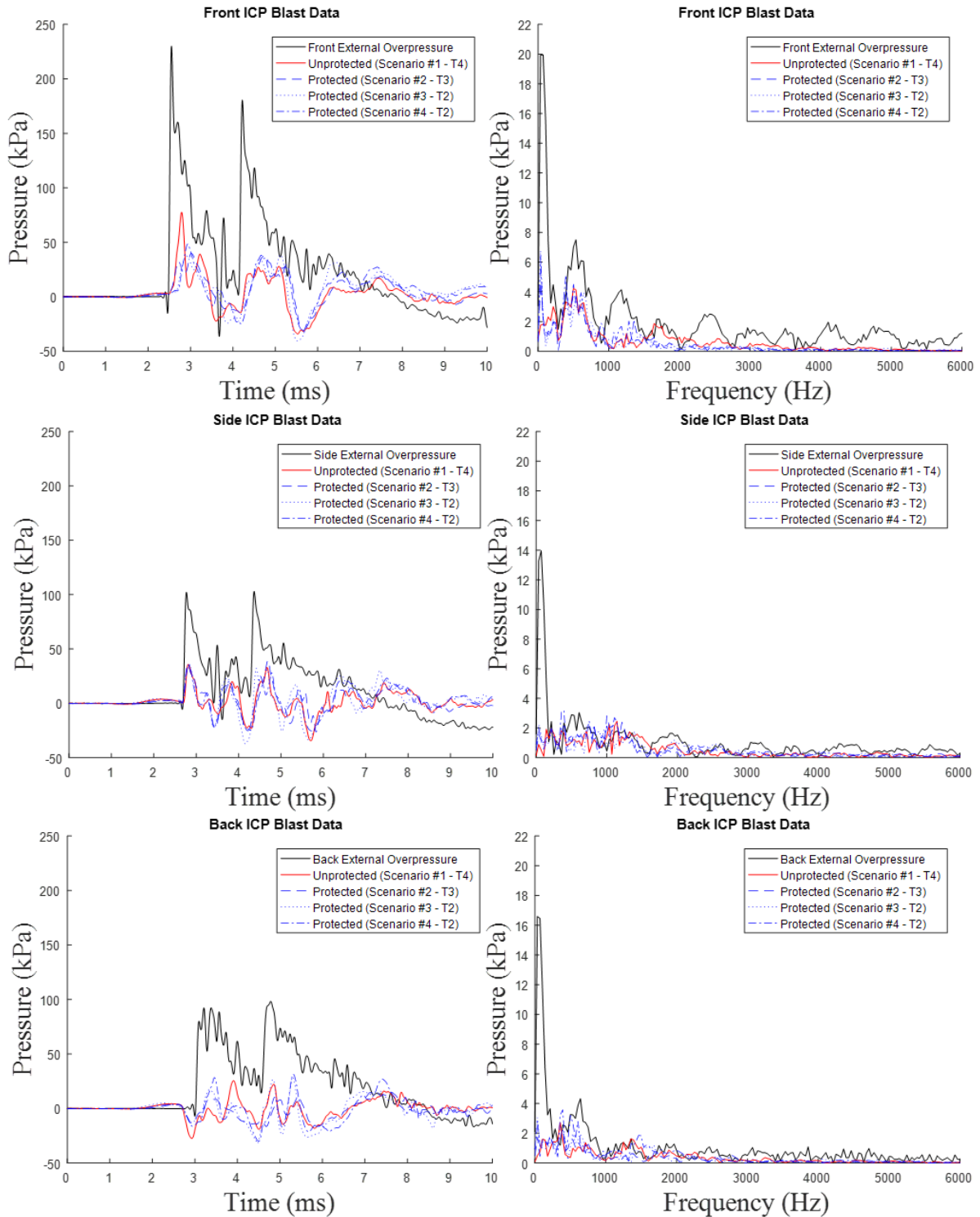
Figure 24: ICP time series and FFT data from blast experiments for various protection scenarios. External overpressure data for each location is also shown for trial #4 from scenario #1. The top row shows front ICP data, the middle row shows side ICP data, and the bottom row shows back ICP data.
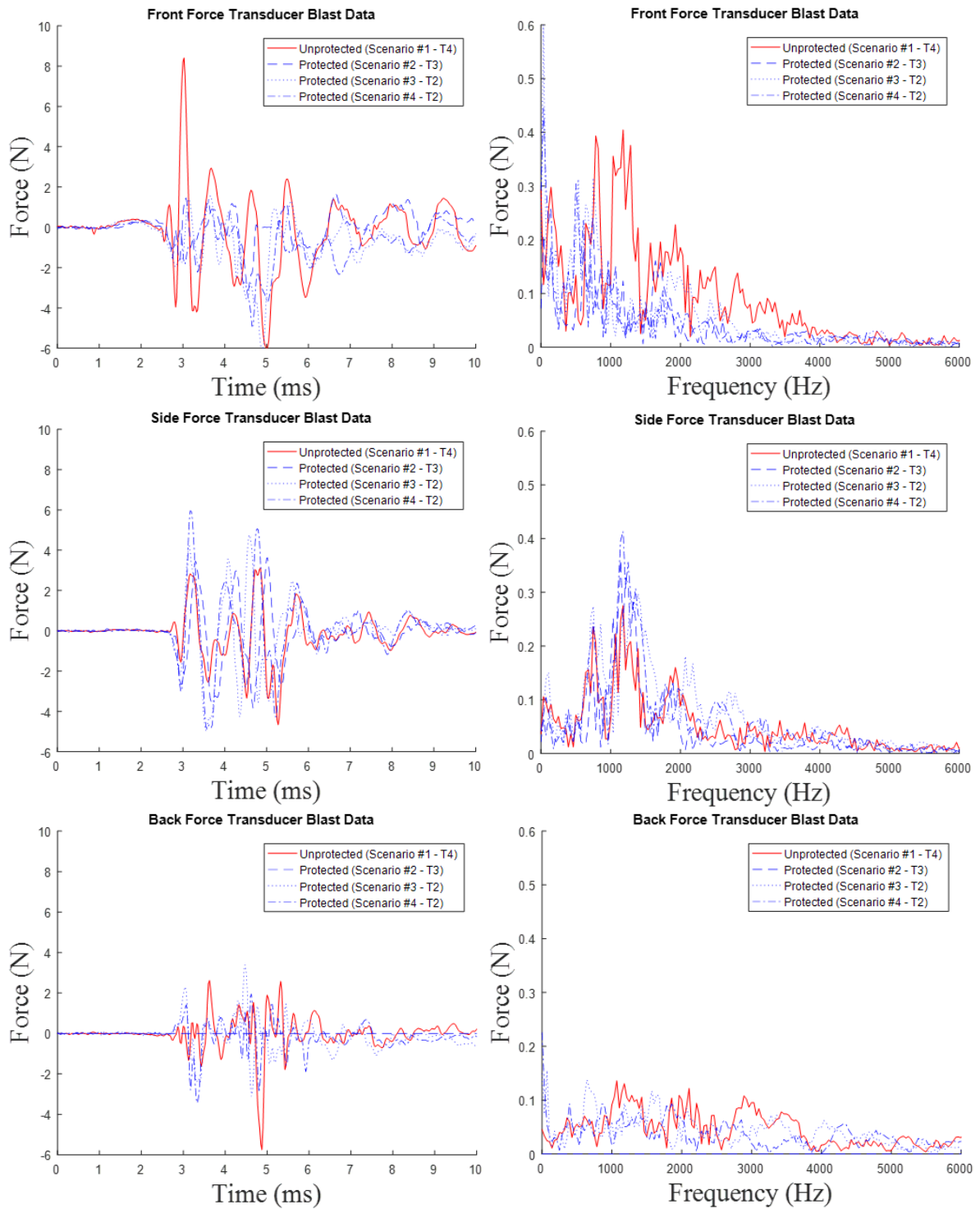
Figure 25: Force time series and FFT data from blast experiments for several protection scenarios. The top row shows front force data, the middle row shows side force data, and the bottom row shows back force data.

Table 8: Maximum and minimum magnitudes in the ICP data for each trial, with means for each scenario.

		Peak ICP Magnitudes					
		Maximum			Minimum		
		Front	Side	Back	Front	Side	Back
Scenario #	Trial #	(kPa)	(kPa)	(kPa)	(kPa)	(kPa)	(kPa)
1	T1	53.5	38.1	10.9	-28.5	-29.2	-25.9
1	T2	79.6	31.7	24.9	-33.4	-26.7	-23.5
1	T3	77.6	35.8	25.6	-34.1	-34.5	-27.4
1	T4	79.2	38.3	34.3	-37.8	-31.4	-30.5
	Mean:	**72.5**	**36.0**	**23.9**	**-33.5**	**-30.4**	**-26.8**
2	T1	52.4	40.7	21.1	-30.3	-31.9	-33.5
2	T2	43.3	37.2	13.8	-24.5	-25.2	-26.5
2	T3	39.8	39.2	15.5	-31.0	-26.3	-16.5
	Mean:	**45.2**	**39.0**	**16.8**	**-28.6**	**-27.8**	**-25.5**
3	T1	38.4	35.8	28.8	-40.5	-37.3	-31.9
3	T2	35.6	33.9	20.7	-30.3	-28.7	-25.4
	Mean:	**37.0**	**34.8**	**24.8**	**-35.4**	**-33.0**	**-28.6**
4	T1	48.4	35.0	31.5	-32.2	-25.9	-29.9
4	T2	51.5	50.0	34.2	-40.1	-41.1	-30.0
	Mean:	**50.0**	**42.5**	**32.8**	**-36.1**	**-33.5**	**-30.0**

Table 9: Maximum and minimum magnitudes in the force signals for each trial, with means for each scenario. Greyed cells containing no values are assigned to results lacking a continuous signal, in which excessive bending occurred in the optical fibre for these trials. When excessive bending occurs, an optical fibre cannot transmit a signal adequately for interrogation, and thus a discontinuity appears in the data until the bending is alleviated.

		Peak FBG Force Magnitudes					
		Maximum			Minimum		
		Front	Side	Back	Front	Side	Back
Scenario #	Trial #	(N)	(N)	(N)	(N)	(N)	(N)
1	T1	8.20		2.83	-4.74		-3.64
1	T2	8.23	3.94		-3.83	-4.62	
1	T3	9.23	3.62		-3.80	-4.65	
1	T4	8.41	3.11	2.62	-5.99	-4.66	-5.75
	Mean:	**8.52**	**3.56**	**2.72**	**-4.59**	**-4.64**	**-4.70**
2	T1	1.37			-2.34		
2	T2	3.60	7.28		-2.80	-5.11	
2	T3	1.77	3.62		-3.13	-3.84	
	Mean:	**2.24**	**5.45**		**-2.76**	**-4.47**	
3	T1	1.79	5.98	3.02	-4.75	-5.54	-4.96
3	T2	1.55	4.75	3.39	-6.17	-4.96	-3.11
	Mean:	**1.67**	**5.36**	**3.20**	**-5.46**	**-5.25**	**-4.03**
4	T1	1.33	5.96	1.95	-4.91	-4.88	-3.44
4	T2	2.49	4.14	1.74	-5.50	-3.59	-2.44
	Mean:	**1.91**	**5.05**	**1.85**	**-5.21**	**-4.23**	**-2.94**
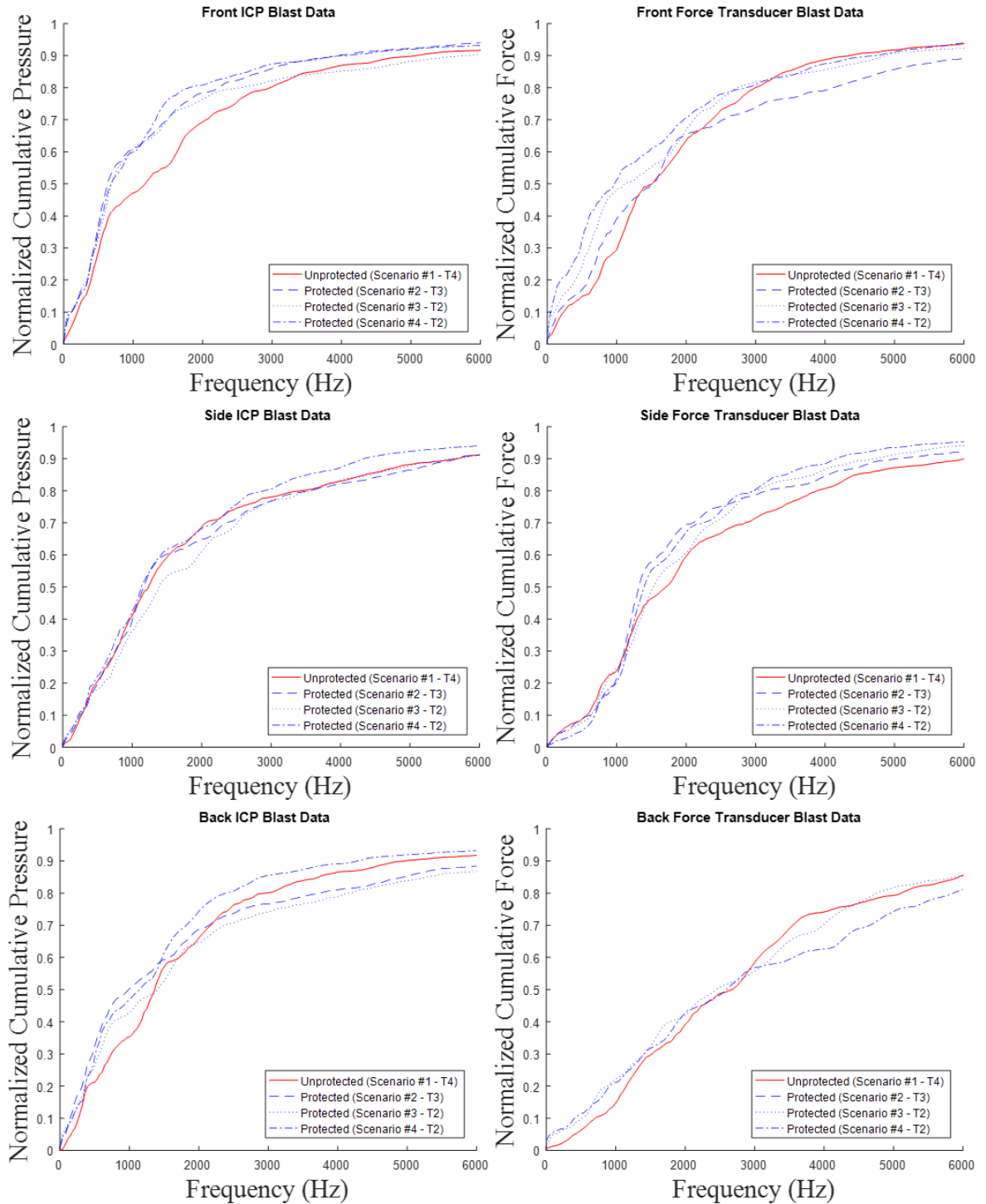
Figure 26: Normalized cumulative FFT data for force and ICP measurements from blast experiments. These figures are plotted up to 6000 Hz, the frequency at which the majority of signals spectral content falls below. Data is normalized based on the accumulated frequency at the Nyquist frequency (250 kHz for ICP and 20 kHz for force data). Therefore, the normalized cumulative results do not reach a value of 1 until higher frequencies than what is shown.

Figure 23 shows representative external pressure field traces, which show near-instantaneous rises in pressure for the incident and ground reflective waves once they reach the headform, with an exponential decay in pressure after their arrival. For these experiments, the ground reflected wave arrives approximately 2 ms after the incident wave. Adding a helmet to the surrogate headform (Scenario #2) reduced front incident shock magnitudes, shown in Table 7, from a mean of 224.5 kPa (Scenario #1) to a mean of 194.2 kPa (attenuation of 13%), however it increased the ground reflected shock magnitudes from a mean of 171.3 kPa to a mean of 231.4 kPa (amplification of 35%). It is important to note that this difference in trends noted in Table 7 for incident and ground reflected peak magnitudes is due to directionality of the arriving blast waves. The incident wave propagates directly towards the BIPED from the charge (at approximately the same height), resulting in purely frontal loading. Because the helmet brim in protected scenarios covers the external pressure transducers (Figure 19b), the result is attenuation of the incident wave for helmeted trials relative to unhelmeted trials as the blast wave propagates through the helmet prior to reaching the external transducer. Conversely, the ground reflected wave propagates towards the BIPED at an upward angle, resulting complex interactions between the helmet brim and scalp of the BIPED, yielding amplification of the ground reflected wave external pressures for helmeted trials relative to unhelmeted trials. Adding eye protection to the surrogate headform (Scenario #3), in addition to a helmet, further attenuated the incident shock from a mean of 194.2 kPa to 110.9 kPa (attenuation of 43%, relative to Scenario #2), measured by the front external transducer. No systematic changes in overpressure measurements for the various protection scenarios were observed for the side and back external pressure transducers.

Measures from instrumentation at the front of the head suggests the addition of head protection affected ICP magnitudes and frequency content. From Table 8, peak frontal ICP measurements were reduced from a mean of 72.5 kPa in the unprotected trials (Scenario #1) to means of 45.2 kPa, 37.0 kPa, and 50.0 kPa in Scenarios #2, 3, and 4, respectively. Adding a TBH helmet alone (Scenario #2, relative to Scenario #1) reduced mean frontal peak ICP measurements by 38%, while mean frontal external incident peak overpressure was reduced by only 13%. From Table 8, peak ICP signals for the side and back transducers did not convey obvious systematic alterations due to addition of protective headgear (despite a large reduction

in the incident wave overpressure and front ICP). The FFT data in Figure 24 demonstrate a shift in the ICP signal towards lower frequencies for the front and back ICP transducers, with reduction in amplitudes between frequencies from 1500 Hz to 2000 Hz. The side ICP data, however, did not convey the same shift in frequency. Side ICP data indicates greater spectral content in the 1000 Hz to 1500 Hz range (protected relative to unprotected). The normalized cumulative distribution plots in Figure 26 better illustrate the shift in frequency content, showing that more of the front ICP transducer signal is accumulated at lower frequencies, particularly below 2000 Hz, when head protection is used (Scenarios #2-4) relative to an unprotected headform (Scenario #1). This shift in spectral content towards lower frequencies is visualized in the normalized cumulative pressure plots as a leftward shift in the normalized cumulative pressure. For the exemplar plot in Figure 26, approximately 60% of the front ICP transducer spectral content is accumulated by 1000 Hz for Scenarios #2-4, in comparison to approximately 47% for Scenario #1. The side ICP data did not indicate change in normalized cumulative pressure for the various protection scenarios.

Relative to an unprotected head, using head protection under blast loading affects the force transducer measurements and their frequency content and the effects noted are largest for instrumentation located at the front of the head. From Table 9, front peak forces at the front are reduced from a mean of 8.52 N in unprotected blast trials (Scenario #1) to means of 2.24 N, 1.67 N, and 1.91 N, for protected Scenarios # 2, 3, and 4, respectively (attenuation of 74% to 80%). In contrast, the side force increased from a mean of 3.56 N in unprotected trials (Scenario #1) to means of 5.45 N, 5.36 N, and 5.05 N, for protected Scenarios #2, 3, and 4, respectively (amplification of 42% to 53%). The FFT data in Figure 25 also demonstrate a shift in spectral content towards lower frequencies for the front and back force transducers, with a particularly substantial attenuation in frequencies in the 1000-1500 Hz range for the front force transducer. Conversely, the side force transducers observe a shift towards more spectral content at higher frequencies, particularly in the 1000-1500 Hz range. Similar to the analysis of ICP signals, the normalized cumulative distribution plots in Figure 26 better illustrate this phenomenon, showing that a greater amount of the force transducer signal is accumulated at lower frequencies when head protection is used (Scenarios #2-4), relative to an unprotected headform (Scenario #1). This shift in spectral content towards lower frequencies is shown as

a leftward shift of the normalized cumulative force. For the plot in Figure 26, between 40% and 50% of the front force transducer spectral content is accumulated below 1000 Hz for Scenarios #2-4, in comparison to 30% for Scenario #1. The normalized cumulative forces for the side transducers appear to accrue more in the 1000-1500 Hz range for the protected scenarios relative to the unprotected trials.

In Figure 23, the reader can note increases in ICP (up to 4 kPa) and force (up to 0.5 N) that occur approximately 1 ms prior to the arrival of the incident blast. These increases have been noted in previous trials and are due to transmission of blast energy from the charge, downward to the ground, through the concrete at the test-site, and then into the head by way of the support post and Hybrid III neck. Because these ICP signals do not correspond to either the incident or ground reflected blasts, they are not considered in our analysis and discussion.

4.4.2 Impact Loading

Representative impact data for each transducer location for both the unprotected and protected headform is shown in Figure 27 and Figure 28 for ICP and force measurements, respectively. Peak magnitudes with means of ICP and force are tabulated in Table 10, Table 11, and Table 12 for low, medium, and high-speed impacts, respectively. Plots comparing results (time series, FFT, and normalized cumulative measurements) for unprotected and protected BIPED scenarios, at each transducer location, are shown in Figure 29 and Figure 30 for ICP and force data, respectively.
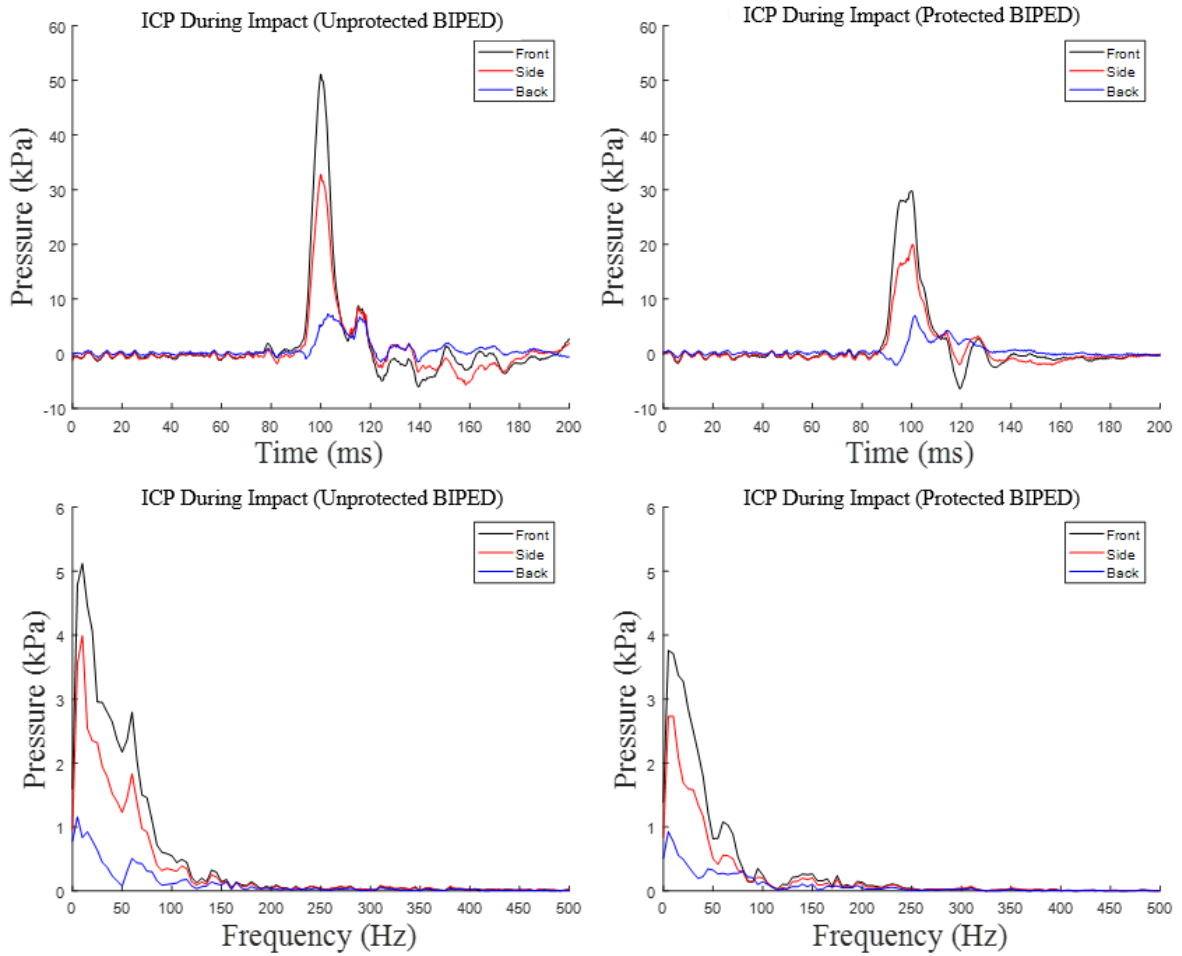
Figure 27: Representative ICP impact measurements from a medium speed impact for an unprotected scenario (left) and protected scenario (right), showing results from each transducer location within the surrogate brain.
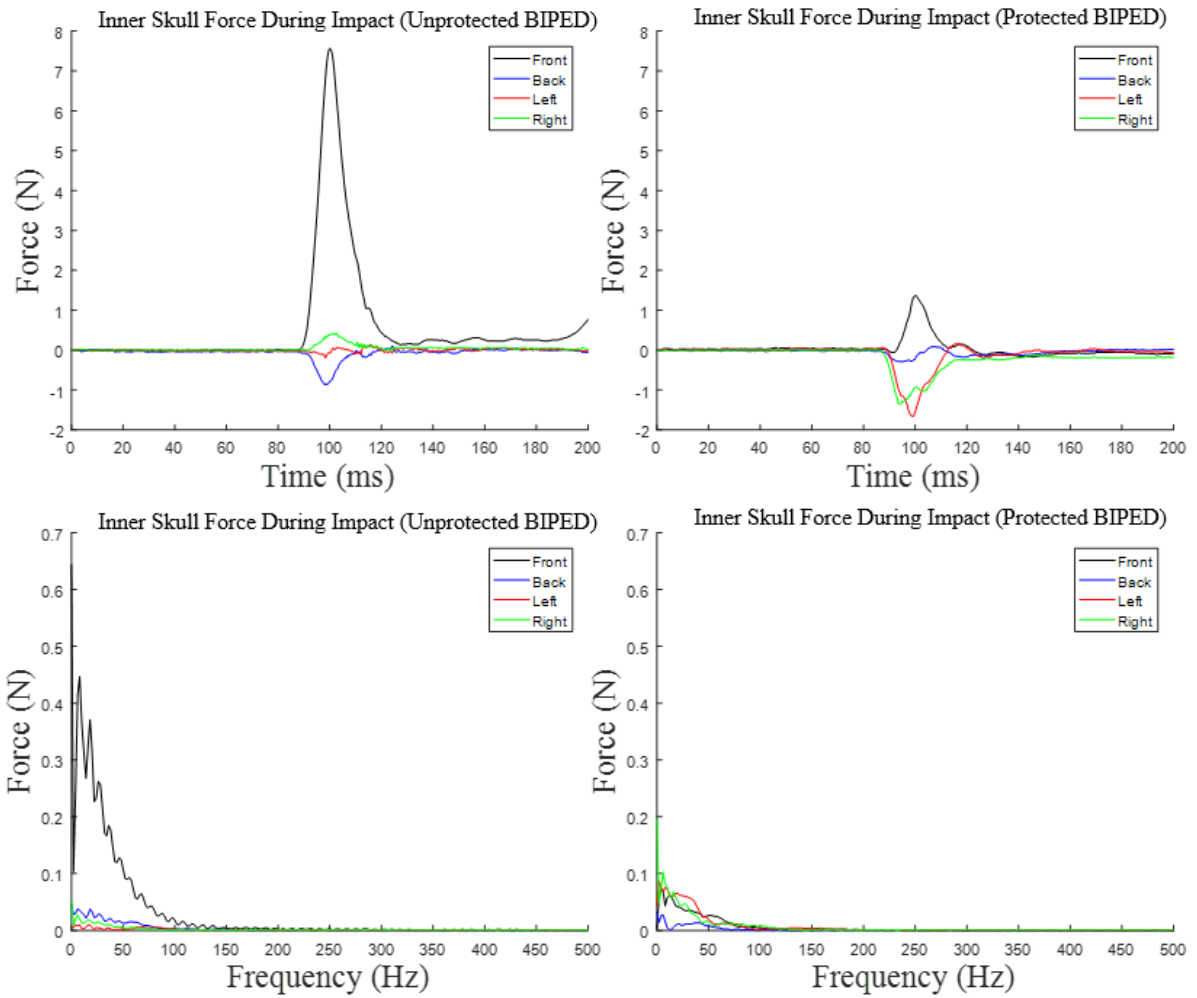
Figure 28: Representative force data from a medium speed impact, for an unprotected scenario (left) and protected scenario (right), showing data from each transducer location.

Table 10: Low speed impact data: peak ICP and force measurements from unprotected (Scenario #1) and protected (Scenario #2) trials. Trials lacking force data due to bending losses in the optical fibres are highlighted in grey. Means, standard deviations, and coefficients of variation are reported in bold text for both Scenario #1 and Scenario #2.

| | | Impact | Peak Force | | | | Peak ICP | | |
| | | Velocity | Front | Back | Left | Right | Front | Back | Side |
Scenario #	Trial #	[m/s]	[N]	[N]	[N]	[N]	[kPa]	[kPa]	[kPa]
1 (Unprotected)	T1	1.63	6.75				31.50	20.07	5.15
1 (Unprotected)	T2	1.72	6.88				32.24	20.77	5.25
1 (Unprotected)	T3	1.69	6.83	-0.68	-0.16	-0.07	32.88	21.27	5.12
1 (Unprotected)	T4	1.66	6.77	-0.69	-0.25	-0.14	33.27	21.39	5.06
1 (Unprotected)	T5	1.68	6.91	-0.64	0.00	-0.33	32.45	20.83	5.07
	Mean:	**1.67**	**6.83**	**-0.67**	**-0.14**	**-0.18**	**32.47**	**20.87**	**5.13**
1 (Unprotected)	**STD:**	**0.03**	**0.07**	**0.03**	**0.12**	**0.13**	**0.67**	**0.52**	**0.08**
	COV:	**2.0%**	**1.0%**	**3.9%**	**91.2%**	**74.6%**	**2.1%**	**2.5%**	**1.5%**
2 (Protected)	T1	1.45					15.66	9.83	3.66
2 (Protected)	T2	1.42		-0.30	-0.75	-0.84	15.59	10.19	3.62
2 (Protected)	T3	1.42		-0.31	-0.84	-0.97	15.23	10.68	3.49
2 (Protected)	T4	1.41		-0.31	-0.84	-0.97	15.54	10.92	3.51
2 (Protected)	T5	1.43	1.18	-0.31	-0.66	-0.83	15.57	10.86	3.40
	Mean:	**1.43**		**-0.31**	**-0.77**	**-0.90**	**15.52**	**10.50**	**3.54**
2 (Protected)	**STD:**	**0.01**		**0.00**	**0.08**	**0.08**	**0.17**	**0.47**	**0.10**
	COV:	**1.0%**		**1.6%**	**11.0%**	**8.7%**	**1.1%**	**4.5%**	**3.0%**

Table 11: Medium speed impact data: peak ICP and force from unprotected (Scenario #1) and protected (Scenario #2) trials. Means, standard deviations, and coefficients of variation are reported in bold text for both Scenario #1 and Scenario #2.

| | | Impact | Peak Force | | | | Peak ICP | | |
| | | Velocity | Front | Back | Left | Right | Front | Back | Side |
Scenario #	Trial #	[m/s]	[N]	[N]	[N]	[N]	[kPa]	[kPa]	[kPa]
1 (Unprotected)	T1	2.36	7.40	-0.90	0.30	0.58	50.28	32.46	7.40
1 (Unprotected)	T2	2.32	7.00	-0.86	0.18	0.51	49.55	31.83	7.45
1 (Unprotected)	T3	2.35	7.12	-0.94	0.18	0.48	50.01	32.25	7.34
1 (Unprotected)	T4	2.35	6.92	-1.01	0.17	0.50	50.31	32.66	7.41
1 (Unprotected)	T5	2.35	7.00	-1.14	0.17	0.48	51.24	32.95	7.33
	Mean:	**2.34**	**7.09**	**-0.97**	**0.20**	**0.51**	**50.28**	**32.43**	**7.39**
1 (Unprotected)	**STD:**	**0.02**	**0.19**	**0.11**	**0.05**	**0.04**	**0.62**	**0.42**	**0.05**
	COV:	**0.7%**	**2.7%**	**11.5%**	**27.2%**	**8.7%**	**1.2%**	**1.3%**	**0.7%**
2 (Protected)	T1	2.31	1.12	-0.33	-2.03	-1.11	24.94	15.52	5.63
2 (Protected)	T2	2.37	1.00	-0.43	-1.90	-1.24	27.50	16.85	6.35
2 (Protected)	T3	2.38	1.06	-0.37	-1.89	-1.16	28.02	17.62	6.48
2 (Protected)	T4	2.37	1.28	-0.34	-1.77	-1.30	28.34	18.29	6.44
2 (Protected)	T5	2.37	1.36	-0.29	-1.66	-1.35	29.60	19.22	6.52
	Mean:	**2.36**	**1.16**	**-0.35**	**-1.85**	**-1.23**	**27.68**	**17.50**	**6.28**
2 (Protected)	**STD:**	**0.03**	**0.15**	**0.05**	**0.14**	**0.10**	**1.72**	**1.41**	**0.37**
	COV:	**1.2%**	**12.9%**	**14.6%**	**7.5%**	**8.0%**	**6.2%**	**8.1%**	**5.9%**

Table 12: High speed impact data: peak ICP and force from unprotected (Scenario #1) and protected (Scenario #2) trials. Means, standard deviations, and coefficients of variation are reported in bold text for both Scenario #1 and Scenario #2.

Scenario #	Trial #	Impact Velocity [m/s]	Front [N]	Back [N]	Left [N]	Right [N]	Front [kPa]	Back [kPa]	Side [kPa]
			Peak Force				**Peak ICP**		
1 (Unprotected)	T1	3.31	8.11	-1.63	0.34	0.97	82.22	54.60	12.75
1 (Unprotected)	T2	3.30	8.06	-1.22	0.19	0.74	81.21	53.39	11.46
1 (Unprotected)	T3	3.29	8.06	-1.10	0.24	0.74	82.50	53.84	11.66
1 (Unprotected)	T4	3.34	7.76	-1.28	0.26	0.86	82.06	53.66	11.73
1 (Unprotected)	T5	3.30	9.18	-1.38	0.17	0.83	81.78	53.30	11.25
	Mean:	**3.31**	**8.23**	**-1.32**	**0.24**	**0.83**	**81.95**	**53.76**	**11.77**
1 (Unprotected)	**STD:**	**0.02**	**0.55**	**0.20**	**0.07**	**0.10**	**0.49**	**0.52**	**0.58**
	COV:	**0.5%**	**6.7%**	**14.9%**	**27.8%**	**11.7%**	**0.6%**	**1.0%**	**4.9%**
2 (Protected)	T1	3.14	2.62	-0.96		-1.67	43.45	26.34	8.84
2 (Protected)	T2	3.29	2.83	-1.19	-2.62	-1.68	45.00	26.50	10.11
2 (Protected)	T3	3.33	2.42	-2.15	-2.77	-1.78	45.95	27.31	10.64
2 (Protected)	T4	3.36	2.44	-0.15	-2.70	-1.85	47.83	28.82	10.15
2 (Protected)	T5	3.43	2.52	-1.85	-2.66	-1.86	49.07	29.45	10.47
	Mean:	**3.31**	**2.57**	**-1.26**	**-2.69**	**-1.77**	**46.26**	**27.68**	**10.04**
2 (Protected)	**STD:**	**0.11**	**0.17**	**0.79**	**0.06**	**0.09**	**2.23**	**1.39**	**0.71**
	COV:	**3.3%**	**6.5%**	**62.4%**	**2.4%**	**5.1%**	**4.8%**	**5.0%**	**7.0%**

High Speed (3.3 - 3.4 m/s) Impact Measurements
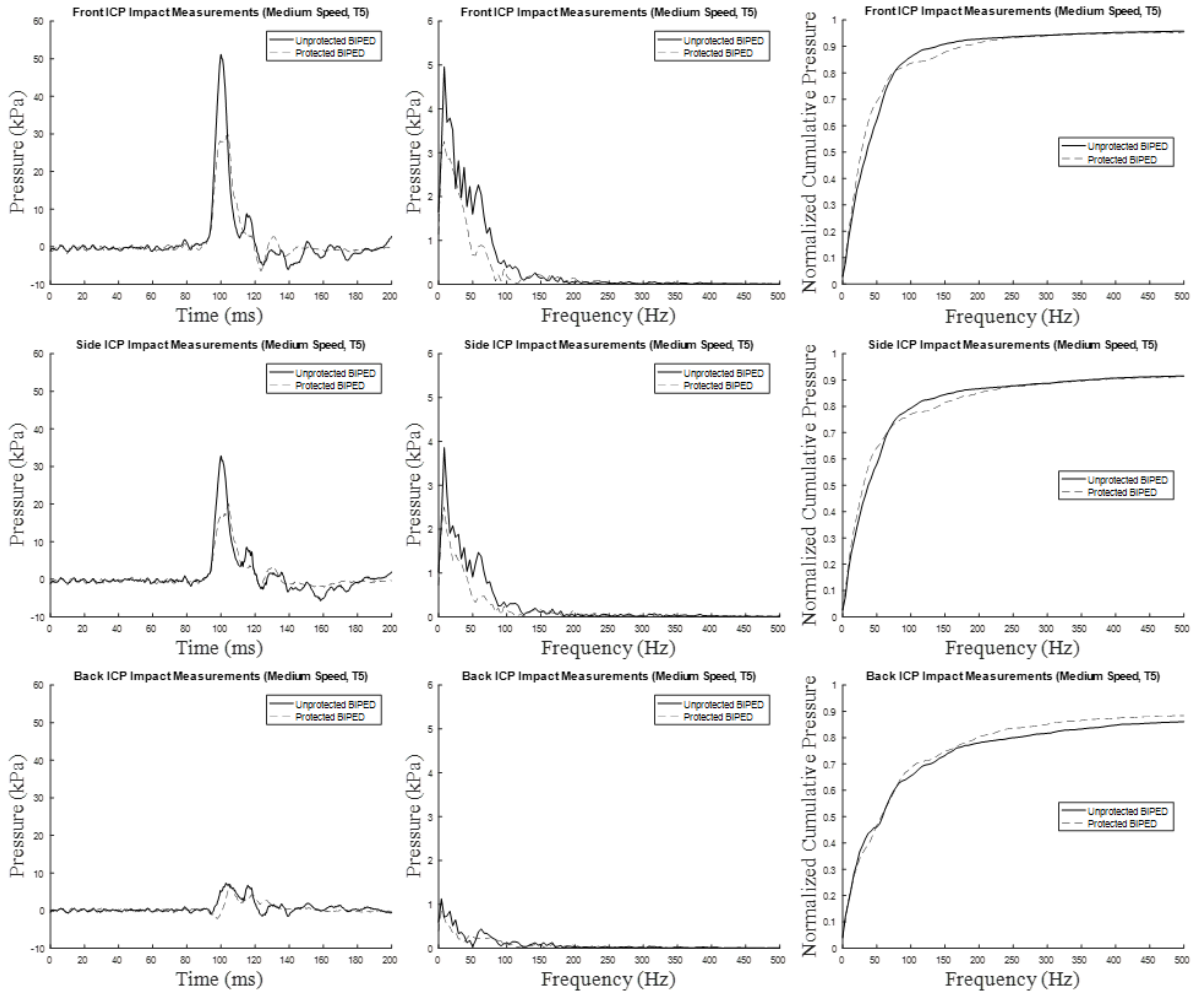
Figure 29: Unprotected vs. protected BIPED impact ICP data showing ICP versus time in the first column, spectral content from an FFT transform in the second column, and normalized cumulative pressure in the third column. The first row shows front transducer measurements, the second row shows side transducer measurements, and the third row shows back transducer measurements.
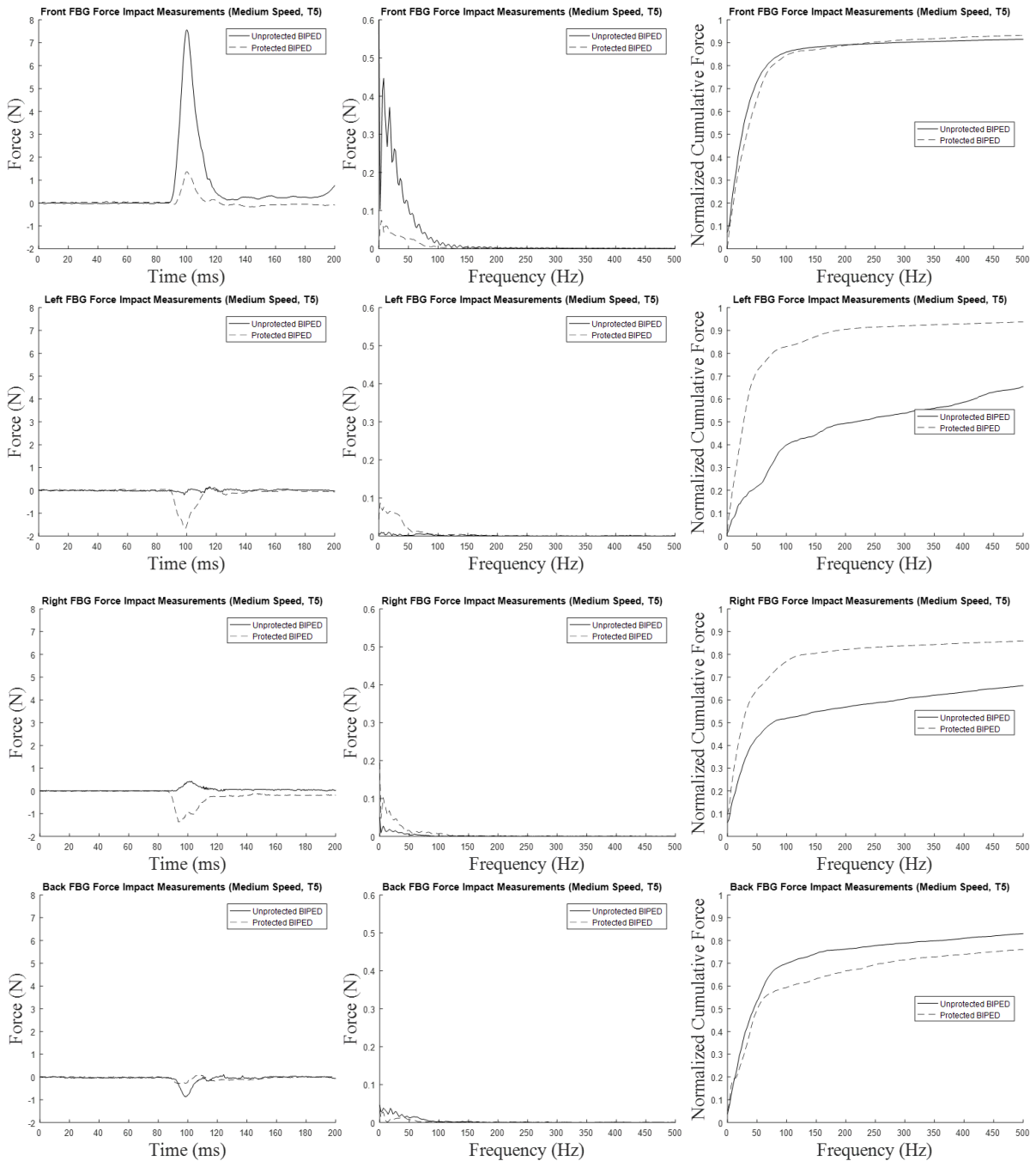
Figure 30: Unprotected and protected BIPED impact force data. Force versus time is shown in the first column, spectral content from an FFT transform in the second column, and normalized cumulative force in the third column. The first row shows front transducer measurements, the second/third rows show side transducer measurements, and the fourth row shows back transducer measurements.

During impact experiments, ICP and force peaks, measured nearest the impact site (front), are reduced by the addition of a helmet. In low speed scenarios (Table 10), peak front ICP reduced from a mean of 32.5 kPa to 15.5 kPa with the addition of a TBH helmet (53% reduction) and peak front force reduced from a mean of 6.83 N to 1.18 N (83% reduction). In medium speed impacts (Table 11), peak front ICP reduced from a mean of 50.3 kPa to 27.7 kPa (45% reduction) with the addition of a TBH, and peak front force reduced from a mean of 7.09 N to a mean of 1.16 N (84% reduction). In high speed impacts (Table 12), peak front ICP reduced from a mean of 82 kPa to a mean of 46.3 kPa with the addition of a TBH (44% reduction), and peak front force reduced from a mean of 8.23 N to a mean of 2.57 N (69% reduction). Data from the back ICP transducer indicates decreases in pressure magnitudes with the addition of helmet. However, the side ICP transducer measurements do not indicate any systematic trend that could be attributed to the presence of head protection. In contrast, specific to force data (Table 10, Table 11, Table 12), the back sensor did not exhibit trends of force reduction with the addition of a helmet. However, data from side located force transducers showed amplification of force with the addition of a TBH.

ICP data for impact experiments do not exhibit shifts in spectral content with the addition of a helmet. The normalized cumulative pressures shown in Figure 29 suggest that for pressure data, both protected and unprotected, over 70% of the accumulation resides between 0 Hz and 100 Hz. Force data did exhibit alteration in the accumulation of force amplitude between the cases of unprotected and protected BIPEDs (Figure 30). Relative to an unprotected BIPED, the protected BIPED, for left and right located force transducer data, accumulates more amplitude at lesser frequencies. Data for front located force transducers suggests that the accumulation of amplitude with frequency is unaffected by the presence (or absence) of head protection. Force data associated with the back of the head suggests the unprotected BIPED accumulates amplitude at lower frequencies than the protected BIPED. Figure 30 shows a shift in the force cumulative frequency distribution plots for the unprotected scenarios, in particular the left and right located transducers, and the tendency is that head protection shifts mechanics to lower frequencies than when the head is not protected. Front and back located transducer measurements convey shift to higher frequencies when the head is protected.

4.5   Discussion

Using a repeatable simulant-based surrogate headform, instrumented with transducers capable of measuring pressure within the brain parenchyma and forces on the inner table of the skull, the results of this work suggest that head protection can be associated with overall reductions in pressures and forces. The surrogate, with novel instrumentation, and the data presented are the first that document forces, along with pressure within the brain, and the effects that adding head protection has on these measures in blast and impact loading. In both blast and impact, the overall trend is that peak pressures and peak forces are lesser for a protected head relative to an unprotected head.

Free-field blast experiments using 5 kg C4 charges at a 5 m standoff produced repeatable blast loading overpressures measured on the outer surface of the BIPED. Between trials and within a given protection scenario, variation in measured overpressure on the head exterior was generally less than 10%. Relative to the alterations in peak pressures and peak forces in the cranial vault, associated with the addition of head protection, which in some cases were 50% (pressure) and 80% (force), 10% variation is relatively small. Further, as shown in Table 7, while there was typically 10% variation (or less) in external pressure data within a given group of data for a given protection scenario, the variations in external pressures between protection scenarios were as high as 50% (reduced, relative to an unprotected BIPED). Consequently, we speculate that the alterations in force and pressure that are noted in the presence of head protection can be associated with the head protection, as opposed to non-repeatability in loading between trials. Therefore, we argue that the blast loading conditions were repeatable and further that the BIPED is capable of detecting alteration in the loading of the head exterior due to the presence of head protection.

The overarching trend is that relative to an unprotected BIPED, head protection could be associated with attenuation of peak metrics. The majority of attenuation occurs for the transducer locations closest to the loading site, with peak forces at the front location attenuated by as much as 84% and peak pressures at the front location within the surrogate brain attenuated by as much as 53%. In contrast, back and side ICP transducer measurements were altered less, and the side force transducer measurements appeared to be amplified. We speculate the increased forces observed on the side of the skull when adding head protection

could explain why the side ICP measurements were not attenuated in the presence of head protection. This may indicate that adding head protection alters the mode of skull flexure [151] and increases the amount of lateral skull deformation under frontal blast loading, which results in increased lateral skull-brain interaction forces.

The measurements from the BIPED also suggest that the addition of headgear alters the frequency content of mechanics experienced in the brain. For blast, Figure 24 shows that higher frequencies are attenuated for the front ICP transducer, particularly in the 1500 Hz to 2000 Hz range. Figure 25 also indicates attenuation for the front force transducer data, particularly in the 1000 Hz to 1500 Hz range, but there is also attenuation from 800 Hz to 900 Hz. There appears to be a shift in spectral content with the addition of protective headgear, in which lower frequency peaks (observed below 600 Hz) are amplified while higher frequencies are attenuated (Figure 24 and Figure 25). The shift in spectral content is demonstrated in Figure 26 where the normalized cumulative plots for the front ICP and force transducers accrue more amplitude at lower frequencies for the protected scenarios relative to the unprotected scenarios (observed as a leftward shift in the top two plots). Findings were mixed for instrumentation located at the side and back of the head; in some cases the protected head accrued amplitude at lesser frequencies, and in some cases greater, relative to the unprotected head. Figure 29 and Figure 30 convey that relative to blast, alteration in frequency content due to head protection was relatively lesser for impact.

ICP signals are significantly lower in comparison to the external overpressures (Figure 24 shows data from various protection scenarios and transducer locations), indicating that energy attenuation occurs as the blast wave propagates through several materials (surrogate scalp, skull, membranes, CSF, and then brain). Figure 23 shows that the most significant ICP fluctuations occur shortly after the arrival of the incident wave, and again approximately 2 ms later after the arrival of the ground reflection wave. Front ICP measurements, shown in Table 8, are approximately 20-40% of the front external pressure transducer, with a mean of 72.5 kPa for the front ICP transducer in an unprotected case (Scenario #1), and means of 45.2 kPa, 37.0 kPa, and 50.0 kPa for protected cases (Scenarios #2,3, and 4, respectively).

In blast experiments, both ICP and force transducers measured negative pressures and forces following positive values occurring earlier in the pressure-time and force-time data,

despite a positive overpressure on the external head form. Arguably, this finding could be construed as counter-intuitive. In this study, ICP signals are observed to be as low as -40.5 kPa for blast and were not negative for impact. Inner table forces are observed to be as low as -6.2 N for blast and -2.2 N for impact. Negative pressures within the cranial vault have been measured in other work using cadavers, under blast loading, and computed in numerical simulations [65,75], in which it is suggested that skull flexure may be a mechanism through which negative pressures are created and cavitation in fluid occurs. While the thresholds of negative pressures that can lead to brain injury through cavitation in humans are not yet agreed upon, and indeed cavitation as a contributor to brain injury is arguably as yet unproven, the BIPED could be capable of quantifying negative valued pressure and force. While skull flexure and resonance have been studied in detail for the BIPED [151], further study is needed to ascertain whether or not the BIPED measurements are accurate in relation to cavitation mechanics.

For the impact loading conditions we subject the BIPED to, the ICP data exhibit similarities to what has been published for experimental cadaveric and numerical simulations. A study on blunt impact to human cadaver heads reports coup and counter-coup pressures at velocities of 3 to 4 m/s [17], using a football helmet for head protection. They found mean peak coup pressures of 58 ± 21.9 kPa (mean $\pm$ standard deviation) for a helmeted cadaver head, and 68.1 ± 47.6 kPa for mean peak coup pressures for an unhelmeted cadaver. Impact pressure pulse widths varied significantly but were typically between 5 to 35 ms duration. ICP and force versus time data from the BIPED exhibit similar pulse widths (approximately 10 to 20 ms for most trials) to the average cadaveric results. Peak frontal ICPs of 82.0 kPa without a helmet and 46.3 kPa with a combat helmet were observed within the BIPED for the high speed impact scenario (3.3 – 3.4 m/s), which are within the pressure ranges observed during the previous cadaveric study, for a similar impact velocity. Another study reconstructed NFL player impacts that resulted in cases of mTBI and simulated, using finite-elements, ICP responses to be 90 ± 24 kPa for injury cases, and 61 ± 17 kPa for non-injury cases [175]. Based on their findings, the high speed results from our study are comparable to the range of simulated ICP responses from reconstructed impact scenarios that have induced mTBI in professional athletes.

The BIPED surrogate model used in this study demonstrates repeatability in both impact and blast measurements in both unprotected and protected scenarios. The measured ICP and force signals report similar peak results and fluctuations, and capture similar spectral profiles for trials of the same protection scenario. For high speed impact experiments, peak front force signals and peak front ICP signals had coefficients of variation (COV) less than 7% in both protected (n = 5) and unprotected scenarios (n = 5), which is lesser than the variation of peak measurements observed within cadaveric tissue. Impact pulse widths (calculated based on the initial impact signal width at 20% of the peak value, reported in a cadaver study by Hardy et al. 2007 [17]) are also significantly more repeatable in the BIPED compared to experiments with post mortem human subjects [17], with COV for ICP and force pulse widths less than 12% for each impact scenario.

We noted important differences in the forces measured at the inner table when comparing impact results to blast results. During impact, force transducers at the side and back of the head measure negative values, while at the front of the head measure positive values. The time-duration of these forces (nominally 20 ms) are approximately the same when comparing front located sensors to all other locations. The negative valued forces could be interpreted to suggest that the separation between the inner table and simulant brain increases as the impact event occurs causing net reduction in the amount of force that the brain exerts on the skull. The separation could be due to either motion of the brain relative to the skull (while the skull geometry is unchanged), or flexure of the skull toward or away from the brain, or a combination of both. The positive increasing forces at the front could be due to the brain compressing the skull due to relative motion, or skull flexure leading the skull to press against the brain, or both. In blast, the force data exhibits high frequency sign reversal in force magnitude, at timescales lesser than 3 ms, and these sign reversals appear at all locations. It is arguably plausible that skull-brain motion and or skull flexure be responsible for the sign reversals measured. Detailed examinations in previous studies suggest that for blast, these sign reversals correspond to skull flexure mechanics [151]. In future work, we will attempt to ascertain whether the mechanics-based explanation offered above for the BIPED in impact is valid, and if it is, the relative contributions of skull flexure or relative motion between the skull-brain in the force versus time data to ascertain which mechanism dominates. Strain sensors, that are mounted to the

skull and co-located with force transducers, could transduct skull flexure and allow us to ascertain the proportional contribution that skull flexure has on energy transfer in impact and blast loading to the BIPED.

The findings in this study, as with any study that involves a surrogate model, are subject to limitations and may not be indicative of how a human head would respond under the same loading conditions. While the BIPED has been shown to measure similar ICP magnitudes and fluctuation durations to a cadaver headform under a specific set of blast loading conditions [66], this does not imply that the BIPED will respond equally to a human head in other loading scenarios such as the free-field blast conditions and the impact loading conditions we tested in this study. In addition, the Hybrid III neck arguably may not be an appropriate model of the human neck for blast. It is often criticized as possessing too great a mechanical stiffness and researchers have speculated the stiffness may lead to head kinematics that are unrealistic relative to the living human, specifically in blunt impact [168,169]. Because the Hybrid III neck has not been characterized or designed for applications in blast, we acknowledge that it could be a poor model for application in blast and further that the findings of our study could be different if neck mechanics are altered. In our study, we reduced flexion-extension neck stiffness for blast experiments (Scenario #4) and observed greater peak ICP and skull-brain forces relative to Scenario #3 (relative stiffer neck), suggesting that neck mechanics may have affect energy transferred into the BIPED. For both blast and impact experiments in this study, the loading into the head was always frontal. Further experiments would be needed to assess whether head protection leads to reductions in mechanics in other loading directions. Future work could also involve testing secondary blast injury due to ballistic/projectile threats from debris/shrapnel [150].

In this work, we quantify mechanical measures of forces on the inner table and pressure within the parenchyma of a simulant-based surrogate headform subjected to blast and impact loading. Our results suggest that adding head protection can attenuate the measured mechanics relative to the case when the surrogate model is unprotected. Head protection had the greatest effect on measurements nearest to the site of blast/impact loading, with front forces attenuated by as much as 80% under blast loading and 84% under impact loading, and front ICP signals attenuated by as much as 49% under blast loading and 53% under impact loading. Additionally,

results for forces and pressures (measured at the head front) for a helmeted head demonstrate propensity towards more spectral content at lower frequencies, relative to an unprotected head. It is premature to ascribe definitive statements regarding mitigation of brain injury risk based on our mechanical measures. However, it is possible that with further biomechanical research that elucidates how mechanics relates to injury likelihood in blast and impact, that measurements like those presented here could indicate whether or not protective headgear offers net protective effects to military personnel exposed to blasts and impacts.

Chapter 5: Conclusions

5.1   Contributions

The primary goals of this thesis were to develop a transducer for measuring forces on the inner skull table during high-rate loading scenarios and to apply this novel technology towards investigating the effect of head protection on the transmissions of blast and impact energy imparted to the head and brain. The main contributions of this thesis work are outlined below:

1. A novel force transducer was developed to make the first measurements of inner skull kinetics during both impact and blast loading scenarios. These transducers are repeatable tools that, when integrated into the BIPED, can be applied towards the evaluation of headgear by inferring the relative efficacy at mitigating energy transmission into the head and brain.

2. The BIPED and embedded instrumentation were applied to blast and impact loading scenarios to document the attenuation of peak internal mechanics, as well as the shift in spectral frequencies, for various protection conditions. There is limited biomechanical data in the literature on the effect of protective headgear on skull-brain kinetics during blast and impact, and therefore these results are an important contribution towards documenting how the skull and brain react under blast and impact loading for a protected head relative to an unprotected head.

3. The BIPED is demonstrated to be a repeatable model for impact loading conditions, in addition to blast. This is an important step towards having an all-encompassing bTBI evaluation device, in which the surrogate headform can be used for evaluating multiple bTBI mechanisms. Prior to this study, blast headforms were only applied towards the investigation of primary blast effects. This work presents the first demonstration of a biofidelic surrogate headform that has been applied towards both primary and tertiary blast loading scenarios.

Overall, the results in this work suggest that protective headgear alters the transmission of blast and impact energy into the head and brain. These results should not be construed to indicate any efficacy or deficiency of the protective headgear that was used.

5.2 Future Work and Recommendations

There are many opportunities for this work to be continued. The BIPED has been shown to measure similar ICP magnitudes and frequencies to a cadaver head under primary blast conditions [66], however validation experiments have not yet been performed for impact or ballistic loading scenarios. For both blast and impact experiments in this work, the loading orientation has always been frontal. Future work could assess the response of the BIPED and the effect of protective headgear on internal mechanics for other loading orientations. The Hybrid III neck was used during this study and is widely employed amongst blunt impact injury research; however, the Hybrid III neck is often criticized for having far greater mechanical stiffness than a human neck. It has been postulated that increased neck stiffness can lead towards unrealistic mechanics in the surrogate model relative to the human head, specifically during blunt impact [168,169]. We acknowledge that the Hybrid III may not be an appropriate model for blast, and future work could employ a more biofidelic neck model towards the assessment of the BIPED and protective headgear under blast. Forthcoming work could also investigate the effect of protective headgear on internal mechanics within the BIPED, along with the repeatability of the surrogate model, under secondary bTBI loading scenarios (e.g. ballistic exposure to shrapnel or other projectile threats).

In the current state of biomechanics research, it is premature to declare any definitive statements regarding injury risk based on the mechanical measures presented in this thesis. Further research on this topic can clarify how these mechanical measures relate to brain injury likelihood during blast and impact events, allowing measurements like what is presented here to indicate whether or not protective headgear can mitigate the risk of bTBI. All of the above-mentioned future work presented in this section provides an opportunity to further develop a complete head protection assessment paradigm against blast, which can ultimately be employed towards reducing the occurrence of bTBI.

References

[1] David W. Wright, 2013, "CDC Grand Rounds: Reducing Severe Traumatic Brain Injury in the United States," Cent. Dis. Control Prev., **62**(27), pp. 549–552.

[2] Seifert, J., 2007, "Incidence and Economic Burden of Injuries in the United States," J. Epidemiol. Community Health, **61**(10), p. 926.

[3] Ling, G. S. F., and Ecklund, J. M., 2011, "Traumatic Brain Injury in Modern War," Curr. Opin. Anaesthesiol., **24**(2), pp. 124–130.

[4] Wilk, J. E., Thomas, J. L., McGurk, D. M., Riviere, L. A., Castro, C. A., and Hoge, C. W., 2010, "Mild Traumatic Brain Injury (Concussion) during Combat: Lack of Association of Blast Mechanism with Persistent Postconcussive Symptoms," J. Head Trauma Rehabil., **25**(1), pp. 9–14.

[5] Morey, R. A., Haswell, C. C., Selgrade, E. S., Massoglia, D., Liu, C., Weiner, J., Marx, C. E., MIRECC Work Group, Cernak, I., and McCarthy, G., 2013, "Effects of Chronic Mild Traumatic Brain Injury on White Matter Integrity in Iraq and Afghanistan War Veterans," Hum. Brain Mapp., **34**(11), pp. 2986–2999.

[6] Cernak, I., and Noble-Haeusslein, L. J., 2010, "Traumatic Brain Injury: An Overview of Pathobiology with Emphasis on Military Populations," J. Cereb. Blood Flow Metab. Off. J. Int. Soc. Cereb. Blood Flow Metab., **30**(2), pp. 255–266.

[7] MacGregor, A. J., Dougherty, A. L., and Galarneau, M. R., 2011, "Injury-Specific Correlates of Combat-Related Traumatic Brain Injury in Operation Iraqi Freedom," J. Head Trauma Rehabil., **26**(4), pp. 312–318.

[8] Terrio, H., Brenner, L. A., Ivins, B. J., Cho, J. M., Helmick, K., Schwab, K., Scally, K., Bretthauer, R., and Warden, D., 2009, "Traumatic Brain Injury Screening: Preliminary Findings in a US Army Brigade Combat Team," J. Head Trauma Rehabil., **24**(1), pp. 14–23.

[9] Polusny, M. A., Kehle, S. M., Nelson, N. W., Erbes, C. R., Arbisi, P. A., and Thuras, P., 2011, "Longitudinal Effects of Mild Traumatic Brain Injury and Posttraumatic Stress Disorder Comorbidity on Postdeployment Outcomes in National Guard Soldiers Deployed to Iraq," Arch. Gen. Psychiatry, **68**(1), pp. 79–89.

[10] Nelson, N. W., Davenport, N. D., Sponheim, S. R., and Anderson, C. R., 2015, "Blast-Related Mild Traumatic Brain Injury: Neuropsychological Evaluation and Findings," *Brain Neurotrauma: Molecular, Neuropsychological, and Rehabilitation Aspects*, F.H. Kobeissy, ed., CRC Press/Taylor & Francis, Boca Raton (FL).

[11] Jones, E., 2007, "Shell Shock and Mild Traumatic Brain Injury: A Historical Review," The American Journal of Psychiatry, **164**(11), pp. 1641–1645.

[12] Belmont, P. J., Goodman, G. P., Zacchilli, M., Posner, M., Evans, C., and Owens, B. D., 2010, "Incidence and Epidemiology of Combat Injuries Sustained during 'the Surge' Portion of Operation Iraqi Freedom by a U.S. Army Brigade Combat Team," J. Trauma, **68**(1), pp. 204–210.

[13] Bass, C. R., Panzer, M. B., Rafaels, K. A., Wood, G., Shridharani, J., and Capehart, B., 2012, "Brain Injuries from Blast," Ann. Biomed. Eng., **40**(1), pp. 185–202.

[14] Fievisohn, E., Bailey, Z., Guettler, A., and VandeVord, P., 2018, "Primary Blast Brain Injury Mechanisms: Current Knowledge, Limitations, and Future Directions," J. Biomech. Eng., **140**(2).

[15] Committee on Review of Test Protocols Used by the DoD to Test Combat Helmets, Board on Army Science and Technology, Division on Engineering and Physical Sciences, and National Research Council, 2014, *Review of Department of Defense Test Protocols for Combat Helmets*, National Academies Press (US), Washington (DC).

[16] Fournier, E., David Sullivan, Bayne, T., and Nicholas Shewchenko, 2007, "Blast Headform Development."

[17] Hardy, W. N., Mason, M. J., Foster, C. D., Shah, C. S., Kopacz, J. M., Yang, K. H., King, A. I., Bishop, J., Bey, M., Anderst, W., and Tashman, S., 2007, "A Study of the Response of the Human Cadaver Head to Impact," Stapp Car Crash J., **51**, p. 17.

[18] Sone, J. Y., Kondziolka, D., Huang, J. H., and Samadani, U., 2016, "Helmet Efficacy against Concussion and Traumatic Brain Injury: A Review," J. Neurosurg., **126**(3), pp. 768–781.

[19] Breeze, J., Baxter, D., Carr, D., and Midwinter, M. J., 2015, "Defining Combat Helmet Coverage for Protection against Explosively Propelled Fragments," J. R. Army Med. Corps, **161**(1), pp. 9–13.

[20] Nakatsuka, A. S., and Yamamoto, L. G., 2014, "External Foam Layers to Football Helmets Reduce Head Impact Severity," Hawaii J. Med. Public Health, **73**(8), pp. 256–261.

[21] Delaney, J. S., Al-Kashmiri, A., Drummond, R., and Correa, J. A., 2008, "The Effect of Protective Headgear on Head Injuries and Concussions in Adolescent Football (Soccer) Players," Br. J. Sports Med., **42**(2), pp. 110–115; discussion 115.

[22] Haider, A. H., Saleem, T., Bilaniuk, J. W., and Barraco, R. D., 2012, "An Evidence Based Review: Efficacy of Safety Helmets in Reduction of Head Injuries in Recreational Skiers and Snowboarders," J. Trauma Acute Care Surg., **73**(5), pp. 1340–1347.

[23] Taber, K. H., Warden, D. L., and Hurley, R. A., 2006, "Blast-Related Traumatic Brain Injury: What Is Known?," J. Neuropsychiatry Clin. Neurosci., **18**(2), pp. 141–145.

[24] Mayorga, M. A., 1997, "The Pathology of Primary Blast Overpressure Injury," Toxicology, **121**(1), pp. 17–28.

[25] Rigby, S. E., Tyas, A., Bennett, T., Clarke, S. D., and Fay, S. D., 2014, "The Negative Phase of the Blast Load," Int. J. Prot. Struct., **5**(1), pp. 1–19.

[26] Westrol, M. S., Donovan, C. M., and Kapitanyan, R., 2017, "Blast Physics and Pathophysiology of Explosive Injuries," Ann. Emerg. Med., **69**(1S), pp. S4–S9.

[27] CombatHelmets, C. on R. of T. P. U. by the D. to T., Technology, B. on A. S. and, Sciences, D. on E. and P., and Council, N. R., 2014, *Threats, Head Injuries, and Test Methodologies*, National Academies Press (US).

[28] BlastExposures, C. on G. W. and H. L.-T. E. of, Populations, B. on the H. of S., and Medicine, I. of, 2014, *Pathophysiology of Blast Injury and Overview of Experimental Data*, National Academies Press (US).

[29] DePalma, R. G., Burris, D. G., Champion, H. R., and Hodgson, M. J., 2005, "Blast Injuries," N. Engl. J. Med., **352**(13), pp. 1335–1342.

[30] Ramasamy, A., Hill, A. M., Masouros, S., Gibb, I., Phillip, R., Bull, A. M. J., and Clasper, J. C., 2013, "Outcomes of IED Foot and Ankle Blast Injuries," J. Bone Joint Surg. Am., **95**(5), p. e25.

[31] Stocchetti, N., and Zanier, E. R., 2016, "Chronic Impact of Traumatic Brain Injury on Outcome and Quality of Life: A Narrative Review," Crit. Care, **20**(148).

[32] Feigin, V. L., Theadom, A., Barker-Collo, S., Starkey, N. J., McPherson, K., Kahan, M., Dowell, A., Brown, P., Parag, V., Kydd, R., Jones, K., Jones, A., Ameratunga, S., and BIONIC Study Group, 2013, "Incidence of Traumatic Brain Injury in New Zealand: A Population-Based Study," Lancet Neurol., **12**(1), pp. 53–64.

[33] Nolan, S., 2005, "Traumatic Brain Injury: A Review," Crit. Care Nurs. Q., **28**(2), pp. 188–194.

[34] Hicks, R. R., Fertig, S. J., Desrocher, R. E., Koroshetz, W. J., and Pancrazio, J. J., 2010, "Neurological Effects of Blast Injury," J. Trauma, **68**(5), pp. 1257–1263.

[35] Hurley, R. A., McGowan, J. C., Arfanakis, K., and Taber, K. H., 2004, "Traumatic Axonal Injury: Novel Insights into Evolution and Identification," J. Neuropsychiatry Clin. Neurosci., **16**(1), pp. 1–7.

[36] McAllister, T. W., Sparling, M. B., Flashman, L. A., and Saykin, A. J., 2001, "Neuroimaging Findings in Mild Traumatic Brain Injury," J. Clin. Exp. Neuropsychol., **23**(6), pp. 775–791.

[37] Monea, A. G., Baeck, K., Verbeken, E., Verpoest, I., Sloten, J. V., Goffin, J., and Depreitere, B., 2014, "The Biomechanical Behaviour of the Bridging Vein – Superior Sagittal Sinus Complex with Implications for the Mechanopathology of Acute Subdural Haematoma," J. Mech. Behav. Biomed. Mater., **32**, pp. 155–165.

[38] Pearce, C. W., and Young, P. G., 2014, "On the Pressure Response in the Brain Due to Short Duration Blunt Impacts," PLOS ONE, **9**(12), p. e114292.

[39] Ward, C., Chan, M., and Nahum, A., 1980, "Intracranial Pressure–A Brain Injury Criterion."

[40] Kenner, V. H., and Goldsmith, W., 1973, "Impact on a Simple Physical Model of the Head," J. Biomech., **6**(1), pp. 1–11.

[41] Freitas, C. J., Mathis, J. T., Scott, N., Bigger, R. P., and MacKiewicz, J., 2014, "Dynamic Response Due to Behind Helmet Blunt Trauma Measured with a Human Head Surrogate," Int. J. Med. Sci., **11**(5), pp. 409–425.

[42] Säljö, A., Svensson, B., Mayorga, M., Hamberger, A., and Bolouri, H., 2009, "Low-Level Blasts Raise Intracranial Pressure and Impair Cognitive Function in Rats," J. Neurotrauma, **26**(8), pp. 1345–1352.

[43] Owens, B. D., Kragh, J. F., Wenke, J. C., Macaitis, J., Wade, C. E., and Holcomb, J. B., 2008, "Combat Wounds in Operation Iraqi Freedom and Operation Enduring Freedom," J. Trauma, **64**(2), pp. 295–299.

[44] Warden, D., 2006, "Military TBI during the Iraq and Afghanistan Wars," J. Head Trauma Rehabil., **21**(5), pp. 398–402.

[45] Elder, G. A., Mitsis, E. M., Ahlers, S. T., and Cristian, A., 2010, "Blast-Induced Mild Traumatic Brain Injury," Psychiatr. Clin. North Am., **33**(4), pp. 757–781.

[46] Clemedson, C. J., and Pettersson, H., 1956, "Propagation of a High Explosive Air Shock Wave through Different Parts of an Animal Body," Am. J. Physiol., **184**(1), pp. 119–126.

[47] Bauman, R. A., Ling, G., Tong, L., Januszkiewicz, A., Agoston, D., Delanerolle, N., Kim, Y., Ritzel, D., Bell, R., Ecklund, J., Armonda, R., Bandak, F., and Parks, S., 2009, "An Introductory Characterization of a Combat-Casualty-Care Relevant Swine Model of Closed Head Injury Resulting from Exposure to Explosive Blast," J. Neurotrauma, **26**(6), pp. 841–860.

[48] Säljö, A., Arrhén, F., Bolouri, H., Mayorga, M., and Hamberger, A., 2008, "Neuropathology and Pressure in the Pig Brain Resulting from Low-Impulse Noise Exposure," J. Neurotrauma, **25**(12), pp. 1397–1406.

[49] Xydakis, M. S., Mulligan, L. P., Smith, A. B., Olsen, C. H., Lyon, D. M., and Belluscio, L., 2015, "Olfactory Impairment and Traumatic Brain Injury in Blast-Injured Combat Troops: A Cohort Study," Neurology, **84**(15), pp. 1559–1567.

[50] Choi, C.-H., 2012, "Mechanisms and Treatment of Blast Induced Hearing Loss," Korean J. Audiol., **16**(3), pp. 103–107.

[51] Shupak, A., Doweck, I., Nachtigal, D., Spitzer, O., and Gordon, C. R., 1993, "Vestibular and Audiometric Consequences of Blast Injury to the Ear," Arch. Otolaryngol. Neck Surg., **119**(12), pp. 1362–1367.

[52] Williams, S. T., Harding, T. H., Statz, J. K., and Martin, J. S., 2017, "Blast Wave Dynamics at the Cornea as a Function of Eye Protection Form and Fit," Mil. Med., **182**(S1), pp. 226–229.

[53] Weichel, E. D., Colyer, M. H., Bautista, C., Bower, K. S., and French, L. M., 2009, "Traumatic Brain Injury Associated with Combat Ocular Trauma," J. Head Trauma Rehabil., **24**(1), pp. 41–50.

[54] Choi, J. H., Greene, W. A., Johnson, A. J., Chavko, M., Cleland, J. M., McCarron, R. M., and Wang, H.-C., 2015, "Pathophysiology of Blast-Induced Ocular Trauma in Rats after Repeated Exposure to Low-Level Blast Overpressure," Clin. Experiment. Ophthalmol., **43**(3), pp. 239–246.

[55] Wang, H.-C. H., Choi, J.-H., Greene, W. A., Plamper, M. L., Cortez, H. E., Chavko, M., Li, Y., Dalle Lucca, J. J., and Johnson, A. J., 2014, "Pathophysiology of Blast-Induced Ocular Trauma with Apoptosis in the Retina and Optic Nerve," Mil. Med., **179**(8 Suppl), pp. 34–40.

[56] Dal Cengio Leonardi, A., Keane, N. J., Hay, K., Ryan, A. G., Bir, C. A., and VandeVord, P. J., 2013, "Methodology and Evaluation of Intracranial Pressure Response in Rats Exposed to Complex Shock Waves," Ann. Biomed. Eng., **41**(12), pp. 2488–2500.

[57] Bolander, R., Mathie, B., Bir, C., Ritzel, D., and VandeVord, P., 2011, "Skull Flexure as a Contributing Factor in the Mechanism of Injury in the Rat When Exposed to a Shock Wave," Ann. Biomed. Eng., **39**(10), pp. 2550–2559.

[58] Moss, W., King, M., and Blackman, E., 2009, "Skull Flexure from Blast Waves: A Mechanism for Brain Injury with Implications for Helmet Design," Phys. Rev. Lett., **103**(10).

[59] Libertiaux, V., Pascon, F., and Cescotto, S., 2011, "Experimental Verification of Brain Tissue Incompressibility Using Digital Image Correlation," J. Mech. Behav. Biomed. Mater., **4**(7), pp. 1177–1185.

[60] Garimella, H. T., Kraft, R. H., and Przekwas, A. J., 2018, "Do Blast Induced Skull Flexures Result in Axonal Deformation?," PLOS ONE, **13**(3), p. e0190881.

[61] Vandevord, P. J., Bolander, R., Sajja, V. S. S. S., Hay, K., and Bir, C. A., 2012, "Mild Neurotrauma Indicates a Range-Specific Pressure Response to Low Level Shock Wave Exposure," Ann. Biomed. Eng., **40**(1), pp. 227–236.

[62] Sajja, V. S. S. S., Galloway, M., Ghoddoussi, F., Kepsel, A., and VandeVord, P., 2013, "Effects of Blast-Induced Neurotrauma on the Nucleus Accumbens," J. Neurosci. Res., **91**(4), pp. 593–601.

[63] Sajja, V. S. S. S., Ereifej, E. S., and VandeVord, P. J., 2014, "Hippocampal Vulnerability and Subacute Response Following Varied Blast Magnitudes," Neurosci. Lett., **570**, pp. 33–37.

[64] Kamnaksh, A., Kovesdi, E., Kwon, S.-K., Wingo, D., Ahmed, F., Grunberg, N. E., Long, J., and Agoston, D. V., 2011, "Factors Affecting Blast Traumatic Brain Injury," J. Neurotrauma, **28**(10), pp. 2145–2153.

[65] Salzar, R. S., Treichler, D., Wardlaw, A., Weiss, G., and Goeller, J., 2017, "Experimental Investigation of Cavitation as a Possible Damage Mechanism in Blast-Induced Traumatic Brain Injury in Post-Mortem Human Subject Heads," J. Neurotrauma, **34**(8), pp. 1589–1602.

[66] Ouellet, S., Bir, C., and Bouamoul, A., 2014, "Direct Comparison of the Primary Blast Response of a Physical Head Model with Post-Mortem Human Subjects," Cambridge, UK.

[67] Wang, C., Pahk, J. B., Balaban, C. D., Miller, M. C., Wood, A. R., and Vipperman, J. S., 2014, "Computational Study of Human Head Response to Primary Blast Waves of Five Levels from Three Directions," PLoS ONE, **9**(11).

[68] Cernak, I., Wang, Z., Jiang, J., Bian, X., and Savic, J., 2001, "Ultrastructural and Functional Characteristics of Blast Injury-Induced Neurotrauma," J. Trauma, **50**(4), pp. 695–706.

[69] Long, J. B., Bentley, T. L., Wessner, K. A., Cerone, C., Sweeney, S., and Bauman, R. A., 2009, "Blast Overpressure in Rats: Recreating a Battlefield Injury in the Laboratory," J. Neurotrauma, **26**(6), pp. 827–840.

[70] Simard, J. M., Pampori, A., Keledjian, K., Tosun, C., Schwartzbauer, G., Ivanova, S., and Gerzanich, V., 2014, "Exposure of the Thorax to a Sublethal Blast Wave Causes a Hydrodynamic Pulse That Leads to Perivenular Inflammation in the Brain," J. Neurotrauma, **31**(14), pp. 1292–1304.

[71] Assari, S., Laksari, K., Barbe, M., and Darvish, K., 2013, "Cerebral Blood Pressure Rise During Blast Exposure in a Rat Model of Blast-Induced Traumatic Brain Injury," San Diego, California, USA, p. V03AT03A016.

[72] Goldberg, M. S., 2010, "Death and Injury Rates of U.S. Military Personnel in Iraq," Mil. Med., **175**(4), pp. 220–226.

[73] A Breeze, 2011, "The Face of War: The Initial Management of Modern Battlefield Ballistic Facial Injuries," Journal of Military and Veterans' Health, **19**(2).

[74] Wood, G. W., Panzer, M. B., Shridharani, J. K., Matthews, K. A., Capehart, B. P., Myers, B. S., and Bass, C. R., 2013, "Attenuation of Blast Pressure behind Ballistic Protective Vests," Inj. Prev. J. Int. Soc. Child Adolesc. Inj. Prev., **19**(1), pp. 19–25.

[75] Goeller, J., Wardlaw, A., Treichler, D., O'Bruba, J., and Weiss, G., 2012, "Investigation of Cavitation as a Possible Damage Mechanism in Blast-Induced Traumatic Brain Injury," J. Neurotrauma, **29**(10), pp. 1970–1981.

[76] Ouellet, S., and Philippens, M., 2018, "The Multi-Modal Responses of a Physical Head Model Subjected to Various Blast Exposure Conditions," Shock Waves, **28**(1), pp. 19–36.

[77] S.G.M. Hossain, 2010, "Material Modeling and Analysis for the Development of a Realistic Blast Headform," University of Nebraska at Lincoln.

[78] Roberts, J., Harrigan, T., Ward, E., Taylor, T., Annett, M., and Merkle, A., 2012, "Human Head-Neck Computational Model for Assessing Blast Injury," J. Biomech., **45**, pp. 2899–2906.

[79] U.S. Army, 2018, "WIAMan Blast Manikin" [Online]. Available: https://www.dtsweb.com/wiaman-blast-manikin/. [Accessed: 15-Oct-2018].

[80] Eyitejumade A. Sogbesan, 2011, "Design and Analysis of Blast Induced Traumatic Brain Injury Mechanism Using a Surrogate Headform: Instrumentation and Outcomes," University of Nebraska-Lincoln.

[81] S Ouellet, Bouamoul, A., R. Gauvin, Binette, J. S., K.V. Williams, and L. Martineau, 2012, "Development of a Biofidelic Head Surrogate for Blast-Induced Traumatic Brain Injury Assessment."

[82] Standards Council of Canada, 2008, "Specifications for Facially Featured Headforms CAN/CSA-Z262.6-02."

[83] 21st Century Solutions Ltd., 1997, "Anatomium: Digital Human 3D Body Anatomy" [Online]. Available: http://www.anatomium.com/.

[84] Sone, J. Y., Kondziolka, D., Huang, J. H., and Samadani, U., 2017, "Helmet Efficacy against Concussion and Traumatic Brain Injury: A Review," J. Neurosurg., **126**(3), pp. 768–781.

[85] Duncan Wallace, and Stephen Rayner, 2012, "Combat Helmets and Blast Traumatic Brain Injury," Journal of Military and Veterans' Health, **20**(1), pp. 10–17.

[86] Breeze, J., Baxter, D., Carr, D., and Midwinter, M. J., 2015, "Defining Combat Helmet Coverage for Protection against Explosively Propelled Fragments," J. R. Army Med. Corps, **161**(1), pp. 9–13.

[87] Nakatsuka, A. S., and Yamamoto, L. G., 2014, "External Foam Layers to Football Helmets Reduce Head Impact Severity," Hawaii J. Med. Public Health, **73**(8), pp. 256–261.

[88] Delaney, J. S., Al-Kashmiri, A., Drummond, R., and Correa, J. A., 2008, "The Effect of Protective Headgear on Head Injuries and Concussions in Adolescent Football (Soccer) Players," Br. J. Sports Med., **42**(2), pp. 110–115; discussion 115.

[89] Haider, A. H., Saleem, T., Bilaniuk, J. W., and Barraco, R. D., 2012, "An Evidence Based Review: Efficacy of Safety Helmets in Reduction of Head Injuries in Recreational Skiers and Snowboarders," J. Trauma Acute Care Surg., **73**(5), pp. 1340–1347.

[90] Walsh, S. M., Scott, B. R., and Spagnuolo, D. M., 2005, *The Development of a Hybrid Thermoplastic Ballistic Material With Application to Helmets*, ARL-TR-3700, ARMY RESEARCH LAB ABERDEEN PROVING GROUND MD.

[91] 1998, "CPSC - Safety Standard for Bicycle Helmets; Final Rule."

[92] 2012, "CSA Z262.1-09: Standard for Ice Hockey Helmets."

[93] 2015, "Standard Performance Specification for Newly Manufactured Football Helmets, NOCSAE DOC (ND) 002-13m15."

[94] Al-Fakih, E., Osman, N. A. A., and Adikan, F. R. M., 2012, "The Use of Fiber Bragg Grating Sensors in Biomechanics and Rehabilitation Applications: The State-of-the-Art and Ongoing Research Topics," Sensors, **12**(10), pp. 12890–12926.

[95] A. D. Kersey, 1997, "Fiber Grating Sensors," IEEE J. Light. Technol., **15**(8), pp. 1442–1463.

[96] Dennison, C. R., Wild, P. M., Wilson, D. R., and Cripton, P. A., 2008, "A Minimally Invasive In-Fibre Bragg Grating Sensor for Intervertebral Disc Pressure Measurements," Meas. Sci. Technol., **085201**, p. 12.

[97] Lee, B., 2003, "Review of the Present Status of Optical Fiber Sensors," Opt. Fiber Technol., **9**(2), pp. 57–79.

[98] Hill, K. O., Fujii, Y., Johnson, D. C., and Kawasaki, B. S., 1978, "Photosensitivity in Optical Fiber Waveguides: Application to Reflection Filter Fabrication," Appl. Phys. Lett., **32**(10), pp. 647–649.

[99] Meltz, G., Morey, W. W., and Glenn, W. H., 1989, "Formation of Bragg Gratings in Optical Fibers by a Transverse Holographic Method," Opt. Lett., **14**, pp. 823–825.

[100] Betz, D. C., Thursby, G., Culshaw, B., and Staszewski, W. J., 2006, "Advanced Layout of a Fiber Bragg Grating Strain Gauge Rosette," J. Light. Technol., **24**(2), pp. 1019–1026.

[101] M.S. Muller, Buck, T. C., El-Khozondar, H. J., and Koch, A. W., 2009, "Shear Strain Influence on Fiber Bragg Grating Measurement Systems," J. Light. Technol., **27**(23), pp. 5223–5229.

[102] Qiu, W., Cheng, X., Luo, Y., Zhang, Q., and Zhu, B., 2013, "Simultaneous Measurement of Temperature and Strain Using a Single Bragg Grating in a Few-Mode Polymer Optical Fiber," J. Light. Technol., **31**(14), pp. 2419–2425.

[103] Chen, G., Liu, L., Jia, H., Yu, J., Xu, L., and Wang, W., 2004, "Simultaneous Strain and Temperature Measurements with Fiber Bragg Grating Written in Novel Hi-Bi Optical Fibre," IEEE Photonics Technol. Lett., **16**, pp. 221–223.

[104] Singlehurst, D. A., Dennison, C. R., and Wild, P. M., 2012, "A Distributed Pressure Measurement System Comprising Multiplexed In-Fibre Bragg Gratings Within a Flexible Superstructure," IEEE J. Light. Technol., **30**, pp. 123–129.

[105] Butz, R., and Dennison, C., 2015, "In-Fibre Bragg Grating Impact Force Transducer for Studying Head-Helmet Mechanical Interaction in Head Impact.," J. Light. Technol., **33**(13), p. 8.

[106] Dennison, C. R., Wild, P. M., Wilson, D. R., and Gilbart, M. K., 2010, "An In-Fiber Bragg Grating Sensor for Contact Force and Stress Measurements in Articular Joints," Meas. Sci. Technol., **21**, p. 115803.

[107] Lee, S.-M., Jeong, M.-Y., and Saini, S. S., 2012, "Etched-Core Fiber Bragg Grating Sensors Integrated With Microfluidic Channels," J. Light. Technol., **30**(8), pp. 1025–1031.

[108] Cameron, K. L., Marshall, S. W., Sturdivant, R. X., and Lincoln, A. E., 2012, "Trends in the Incidence of Physician-Diagnosed Mild Traumatic Brain Injury among Active Duty U.S. Military Personnel between 1997 and 2007," J. Neurotrauma, **29**(7), pp. 1313–1321.

[109] Hoge, C. W., and Castro, C. A., 2011, "Blast-Related Traumatic Brain Injury in U.S. Military Personnel," N. Engl. J. Med., **365**(9), pp. 860; author reply 860-861.

[110] James M. Thompson, 2008, "Persistent Symptoms Following Mild Traumatic Brain Injury (MTBI) - A Resource for Clinicians and Staff."

[111] Wolf, S. J., Bebarta, V. S., Bonnett, C. J., Pons, P. T., and Cantrill, S. V., 2009, "Blast Injuries," The Lancet, **374**(9687), pp. 405–415.

[112] Bandak, F. A., Ling, G., Bandak, A., and De Lanerolle, N. C., 2015, "Injury Biomechanics, Neuropathology, and Simplified Physics of Explosive Blast and Impact Mild Traumatic Brain Injury," Handb. Clin. Neurol., **127**, pp. 89–104.

[113] Chavko, M., Koller, W. A., Prusaczyk, W. K., and McCarron, R. M., 2007, "Measurement of Blast Wave by a Miniature Fiber Optic Pressure Transducer in the Rat Brain," J. Neurosci. Methods, **159**(2), pp. 277–281.

[114] Leonardi, A. D. C., Bir, C. A., Ritzel, D. V., and VandeVord, P. J., 2010, "Intracranial Pressure Increases during Exposure to a Shock Wave," J. Neurotrauma, **28**(1), pp. 85–94.

[115] Svetlov, S. I., Prima, V., Kirk, D. R., Gutierrez, H., Curley, K. C., Hayes, R. L., and Wang, K. K. W., 2010, "Morphologic and Biochemical Characterization of Brain Injury in a Model of Controlled Blast Overpressure Exposure," J. Trauma, **69**(4), pp. 795–804.

[116] Rubovitch, V., Ten-Bosch, M., Zohar, O., Harrison, C. R., Tempel-Brami, C., Stein, E., Hoffer, B. J., Balaban, C. D., Schreiber, S., Chiu, W.-T., and Pick, C. G., 2011, "A Mouse Model of Blast-Induced Mild Traumatic Brain Injury," Exp. Neurol., **232**(2), pp. 280–289.

[117] Sosin, D. M., 1990, "Head Injury—Associated Deaths From Motorcycle Crashes: Relationship to Helmet-Use Laws," JAMA, **264**(18), p. 2395.

[118] Robinson, D. L., 2001, "Changes in Head Injury with the New Zealand Bicycle Helmet Law," Accid. Anal. Prev., **33**(5), pp. 687–691.

[119] Olivier, J., Walter, S. R., and Grzebieta, R. H., 2013, "Long Term Bicycle Related Head Injury Trends for New South Wales, Australia Following Mandatory Helmet Legislation," Accid. Anal. Prev., **50**, pp. 1128–1134.

[120] Nahum, A., Smith, R., and Ward, C., "Intracranial Pressure Dynamics During Head Impact," SAE Int. Tech. Pap. 770922, p. 1977.

[121] Hardy, W. N., Khalil, T. B., and King, A. I., 1994, "Literature Review of Head Injury Biomechanics," Int. J. Impact Eng., **15**(4), pp. 561–586.

[122] Turner, R. C., Naser, Z. J., Bailes, J. E., Smith, D. W., Fisher, J. A., and Rosen, C. L., 2012, "Effect of Slosh Mitigation on Histologic Markers of Traumatic Brain Injury," J. Neurosurg., **117**(6), pp. 1110–1118.

[123] Foster, J. K., Kortge, J. O., and Wolanin, M. J., 1977, "Hybrid III-A Biomechanically-Based Crash Test Dummy," pp. 975–1014.

[124] D Hynd, 2007, "The Use of the Hybrid III Dummy in Low-Speed Rear Impact Testing."

[125] Beckwith, J. G., Greenwald, R. M., and Chu, J. J., 2012, "Measuring Head Kinematics in Football: Correlation Between the Head Impact Telemetry System and Hybrid III Headform," Ann. Biomed. Eng., **40**(1), pp. 237–248.

[126] Ivarsson, J., Viano, D. C., and Lövsund, P., 2002, "Influence of the Lateral Ventricles and Irregular Skull Base on Brain Kinematics Due to Sagittal Plane Head Rotation," J. Biomech. Eng., **124**(4), pp. 422–431.

[127] A. Othonos, 2000, "Bragg Gratings in Optical Fibers: Fundamentals and Applications," Opt. Fiber Sens. Technol., pp. 79–187.

[128] Xu, M. G., Reekie, L., Chow, Y. T., and Dakin, J. P., 1993, "Optical In-Fibre Grating High Pressure Sensor," Electron. Lett., **29**, pp. 398–399.

[129] Measures, R. M., 2001, *Structural Health Monitoring with Fiber Optic Technology*, Academic Press.

[130] Xu, M. G., Geiger, H., and Dakin, J. P., 1996, "Fibre Grating Pressure Sensor with Enhanced Sensitivity Using a Glass-Bubble Housing," Electron. Lett., **32**, pp. 128–129.

[131] Wilk, J. E., Thomas, J. L., McGurk, D. M., Riviere, L. A., Castro, C. A., and Hoge, C. W., 2010, "Mild Traumatic Brain Injury (Concussion) during Combat: Lack of Association of Blast Mechanism with Persistent Postconcussive Symptoms," J. Head Trauma Rehabil., **25**(1), pp. 9–14.

[132] Morey, R. A., Haswell, C. C., Selgrade, E. S., Massoglia, D., Liu, C., Weiner, J., Marx, C. E., MIRECC Work Group, Cernak, I., and McCarthy, G., 2013, "Effects of Chronic Mild Traumatic Brain Injury on White Matter Integrity in Iraq and Afghanistan War Veterans," Hum. Brain Mapp., **34**(11), pp. 2986–2999.

[133] Cernak, I., and Noble-Haeusslein, L. J., 2010, "Traumatic Brain Injury: An Overview of Pathobiology with Emphasis on Military Populations," J. Cereb. Blood Flow Metab. Off. J. Int. Soc. Cereb. Blood Flow Metab., **30**(2), pp. 255–266.

[134] Belanger, H. G., Kretzmer, T., Yoash-Gantz, R., Pickett, T., and Tupler, L. A., 2009, "Cognitive Sequelae of Blast-Related versus Other Mechanisms of Brain Trauma," J. Int. Neuropsychol. Soc. JINS, **15**(1), pp. 1–8.

[135] MacGregor, A. J., Dougherty, A. L., and Galarneau, M. R., 2011, "Injury-Specific Correlates of Combat-Related Traumatic Brain Injury in Operation Iraqi Freedom," J. Head Trauma Rehabil., **26**(4), pp. 312–318.

[136] Terrio, H., Brenner, L. A., Ivins, B. J., Cho, J. M., Helmick, K., Schwab, K., Scally, K., Bretthauer, R., and Warden, D., 2009, "Traumatic Brain Injury Screening: Preliminary Findings in a US Army Brigade Combat Team," J. Head Trauma Rehabil., **24**(1), pp. 14–23.

[137] Polusny, M. A., Kehle, S. M., Nelson, N. W., Erbes, C. R., Arbisi, P. A., and Thuras, P., 2011, "Longitudinal Effects of Mild Traumatic Brain Injury and Posttraumatic Stress Disorder Comorbidity on Postdeployment Outcomes in National Guard Soldiers Deployed to Iraq," Arch. Gen. Psychiatry, **68**(1), pp. 79–89.

[138] Nelson, N. W., Davenport, N. D., Sponheim, S. R., and Anderson, C. R., 2015, "Blast-Related Mild Traumatic Brain Injury: Neuropsychological Evaluation and Findings," *Brain Neurotrauma: Molecular, Neuropsychological, and Rehabilitation Aspects*, F.H. Kobeissy, ed., CRC Press/Taylor & Francis, Boca Raton (FL).

[139] Jones, E., 2007, "Shell Shock and Mild Traumatic Brain Injury: A Historical Review," American Journal of Psychiatry, **164**(11), pp. 1641–1645.

[140] Belmont, P. J., Goodman, G. P., Zacchilli, M., Posner, M., Evans, C., and Owens, B. D., 2010, "Incidence and Epidemiology of Combat Injuries Sustained during 'the Surge' Portion of Operation Iraqi Freedom by a U.S. Army Brigade Combat Team," J. Trauma, **68**(1), pp. 204–210.

[141] Bass, C. R., Panzer, M. B., Rafaels, K. A., Wood, G., Shridharani, J., and Capehart, B., 2012, "Brain Injuries from Blast," Ann. Biomed. Eng., **40**(1), pp. 185–202.

[142] Tanielian, T., and Jaycox, L. H., 2008, *Invisible Wounds of War: Psychological and Cognitive Injuries, Their Consequences, and Services to Assist Recovery.*, RAND Coporation, Santa Monica, CA.

[143] Nelson, T. J., Wall, D. B., Stedje-Larsen, E. T., Clark, R. T., Chambers, L. W., and Bohman, H. R., 2006, "Predictors of Mortality in Close Proximity Blast Injuries during Operation Iraqi Freedom," J. Am. Coll. Surg., **202**(3), pp. 418–422.

[144] Jones, N., Thandi, G., Fear, N. T., Wessely, S., and Greenberg, N., 2014, "The Psychological Effects of Improvised Explosive Devices (IEDs) on UK Military Personnel in Afghanistan," Occup. Environ. Med., **71**(7), pp. 466–471.

[145] Galarneau, M. R., Woodruff, S. I., Dye, J. L., Mohrle, C. R., and Wade, A. L., 2008, "Traumatic Brain Injury during Operation Iraqi Freedom: Findings from the United States Navy-Marine Corps Combat Trauma Registry," J. Neurosurg., **108**(5), pp. 950–957.

[146] BlastExposures, C. on G. W. and H. L.-T. E. of, Populations, B. on the H. of S., and Medicine, I. of, 2014, *Pathophysiology of Blast Injury and Overview of Experimental Data*, National Academies Press (US).

[147] Chatelin, S., Constantinesco, A., and Willinger, R., 2010, "Fifty Years of Brain Tissue Mechanical Testing: From in Vitro to in Vivo Investigations," Biorheology, **47**(5–6), pp. 255–276.

[148] Skotak, M., Alay, E., Zheng, J. Q., Halls, V., and Chandra, N., 2018, "Effective Testing of Personal Protective Equipment in Blast Loading Conditions in Shock Tube: Comparison of Three Different Testing Locations," PLoS ONE, **13**(6).

[149] Nyein, M. K., Jason, A. M., Yu, L., Pita, C. M., Joannopoulos, J. D., Moore, D. F., and Radovitzky, R. A., 2010, "In Silico Investigation of Intracranial Blast Mitigation with Relevance to Military Traumatic Brain Injury," Proc. Natl. Acad. Sci., **107**(48), pp. 20703–20708.

[150] Nguyen, T.-T., Pearce, A. P., Carpanen, D., Sory, D., Grigoriadis, G., Newell, N., Clasper, J., Bull, A., Proud, W. G., and Masouros, S. D., 2018, "Experimental Platforms to Study Blast Injury," J. R. Army Med. Corps, p. jramc-2018-000966.

[151] Ouellet, S., and Philippens, M., 2018, "The Multi-Modal Responses of a Physical Head Model Subjected to Various Blast Exposure Conditions," Shock Waves, **28**(1), pp. 19–36.

[152] Kleiven, S., 2003, "Influence of Impact Direction on the Human Head in Prediction of Subdural Hematoma," J. Neurotrauma, **20**(4), pp. 365–379.

[153] Knowles, B. M., MacGillivray, S. R., Newman, J. A., and Dennison, C. R., 2017, "Influence of Rapidly Successive Head Impacts on Brain Strain in the Vicinity of Bridging Veins.," J. Biomech., **59**, pp. 59–70.

[154] Goggio, A. F., 1941, "The Mechanism of Contre-Coup Injury," J. Neurol. Psychiatry, **4**(1), pp. 11–22.

[155] Meaney, D. F., and Smith, D. H., 2011, "Biomechanics of Concussion," Clin. Sports Med., **30**(1), pp. 19–31, vii.

[156] Raymond, D., Van Ee, C., Crawford, G., and Bir, C., 2009, "Tolerance of the Skull to Blunt Ballistic Temporo-Parietal Impact," J. Biomech., **42**(15), pp. 2479–2485.

[157] McElhaney, J. H., Hopper, R. H., Nightingale, R. W., and Myers, B. S., 1995, "Mechanisms of Basilar Skull Fracture," J. Neurotrauma, **12**(4), pp. 669–678.

[158] Kleiven, S., 2013, "Why Most Traumatic Brain Injuries Are Not Caused by Linear Acceleration but Skull Fractures Are," Front. Bioeng. Biotechnol., **1**.

[159] Mckee, A. C., and Daneshvar, D. H., 2015, "The Neuropathology of Traumatic Brain Injury," Handb. Clin. Neurol., **127**, pp. 45–66.

[160] Inglese, M., Makani, S., Johnson, G., Cohen, B. A., Silver, J. A., Gonen, O., and Grossman, R. I., 2005, "Diffuse Axonal Injury in Mild Traumatic Brain Injury: A Diffusion Tensor Imaging Study," J. Neurosurg., **103**(2), pp. 298–303.

[161] Stemper, B. D., and Pintar, F. A., 2014, "Biomechanics of Concussion," Prog. Neurol. Surg., **24**, pp. 14–27.

[162] Backman, M. E., and Goldsmith, W., 1978, "The Mechanics of Penetration of Projectiles into Targets," Int. J. Eng. Sci., **16**(1), pp. 1–99.

[163] McIntosh, A. S., and Janda, D., 2003, "Evaluation of Cricket Helmet Performance and Comparison with Baseball and Ice Hockey Helmets," Br. J. Sports Med., **37**(4), pp. 325–330.

[164] Cameron, K. L., Marshall, S. W., Sturdivant, R. X., and Lincoln, A. E., 2012, "Trends in the Incidence of Physician-Diagnosed Mild Traumatic Brain Injury among Active Duty U.S. Military Personnel between 1997 and 2007," J. Neurotrauma, **29**(7), pp. 1313–1321.

[165] Azar, A., Bhagavathula, K. B., Hogan, J., Josey, T., Ouellet, S., Satapathy, S., and Dennison, C. R., 2018, "An Optical Fibre Transducer for Measuring Kinetics of Skull-Brain Interaction in a Surrogate Model of the Human Head Subjected to Blast Overpressure," IEEE Sens. J., pp. 1–1.

[166] James L. Underwood, 1981, "Technology Assessment Program: NIJ Standard for Ballistic Helmets," U.S. Department of Justice - National Institute of Justice.

[167] Office of Justice Programs, 2017, "Active NIJ Standards and Comparative Test Methods," Natl. Inst. Justice [Online]. Available: https://www.nij.gov:443/topics/technology/standards-testing/Pages/active.aspx. [Accessed: 13-Nov-2018].

[168] Sances, A., and Kumaresan, S., 2001, "Comparison of Biomechanical Head-Neck Responses of Hybrid III Dummy and Whole Body Cadaver during Inverted Drops," Biomed. Sci. Instrum., **37**, pp. 423–427.

[169] Brian Herbst, Stephen Forrest, David Chng, and Anthony Sances Jr, 1998, "Fidelity of Anthropometric Test Dummy Necks in Rollover Accidents," *Proceedings of the 16th International Technical Conference on the Enhanced Safety of Vehicles (ESV)*.

[170] Knowles, B. M., and Dennison, C. R., 2017, "Predicting Cumulative and Maximum Brain Strain Measures From HybridIII Head Kinematics: A Combined Laboratory Study and Post-Hoc Regression Analysis," Ann. Biomed. Eng., **45**(9), pp. 2146–2158.

[171] Butz, R., Knowles, B., Newman, J., and Dennison, C., "Effects of External Helmet Accessories on Biomechanical Measures of Head Injury Risk: An ATD Study Using the HybridIII Headform," J. Biomech., **48**(14), pp. 3816–3824.

[172] Alphonse, V. D., Kemper, A. R., and Duma, S. M., 2015, "Effects of Filtering on Experimental Blast Overpressure Measurements," Biomed. Sci. Instrum., **51**, pp. 143–150.

[173] Society of Automotive Engineers, 2014, "SAE J211 Instrumentation for Impact Test - Part 1: Electronic Instrumentation."

[174] M. Philippens, B. de Jong, S. Ouellet, A. Bouamoul, and A. Zwanenburg, 2018, "Response of the BIPED Head Physical Model to Low Level Shockwaves."

[175] Zhang, L., Yang, K. H., and King, A. I., 2001, "Comparison of Brain Responses between Frontal and Lateral Impacts by Finite Element Modeling," J. Neurotrauma, **18**(1), pp. 21–30.